UNIVERSITA' DEGLI STUDI DI PADOVA

DIPARTIMENTO DI INGEGNERIA INDUSTRIALE

CORSO DI LAUREA MAGISTRALE IN INGEGNERIA CHIMICA E DEI PROCESSI INDUSTRIALI

Tesi di Laurea Magistrale in
Ingegneria Chimica e dei Processi Industriali

MECHANISTIC ANALYSIS AND MODELLING OF MILLING OF PHARMACEUTICAL RIBBONS

Relatore: Prof. Andrea Claudio Santomaso
Correlatore: Prof. Chuan–Yu Wu

Laureando: FILIPPO POZZA

ANNO ACCADEMICO 2017–2018

Alla mia famiglia,
per il vostro continuo sostegno e supporto,
sempre,
Grazie.

Abstract

Dry granulation through roll compaction followed by milling is a widespread pharmaceutical process. It consists of two main processes: the powder compression and the ribbon milling. One part of the project deeply deals with the mechanistic analysis of powder compression, applying well–established mathematical models like Heckel and Kawakita to analyse the material behaviour along the compression. Indeed the material properties of the powder and the conditions in the compactor affect the strength of the tablets, and subsequently affect the size distribution of milled ribbons. A good prediction of granule size distribution is essential for ensuring table quality. Therefore the other major part of the project involves the population balance model (PBM) approach, which is widely adopted to model breakage, crystallization and settling processes in various industries, such as mining, food, chemical and pharmaceutical. Modelling breakage with PBM requires the formulation of a breakage kernel that represents the breakage phenomenon. Therefore, a mass-based population balance model coupled with a new mass–based breakage kernel based on the Weibull function is developed in this study to simulate the batch milling process. Both model parameter estimation and sensitivity are performed. The model shows good agreement with the experimental data and it is particularly suitable for modelling bi–modal distribution. A sensitivity analysis leads to a simplified model with only one variable as a function of porosity and the accuracy is experimentally validated.

Riassunto

La granulazione a secco tramite compattazione e successiva macinatura é un processo altamente impiegato nell'industria farmaceutica. Consta principalmente di due processi: la compressione di polveri e la macinatura dei nastri. Una parte del progetto tratta la compattazione delle polveri attraverso un'analisi meccanicistica. Affermati modelli matematici come Heckel e Kawakita sono stati implementati per analizzare il comportamento del materiale durante la compressione. Infatti le proprietà delle polveri e le condizioni adottate nel compattatore influenzano la tenacità delle pastiglie, e conseguentemente anche la distribuzione granulometrica dei nastri macinati. Una rigorosa predizione della distribuzione granulometrica dei granuli è essenziale per garantire ottime proprietà delle pastiglie. Quindi la seconda parte del progetto prevede l'utilizzo del bilancio di popolazione (PBM). Tale approccio è largamente impiegato per modellare i processi di rottura, cristallizzazione e sedimentazione in varie industrie, come quella mineraria, alimentare, chimica o farmaceutica. Per modellare la rottura con PBM è necessario impostare un kernel che sia rappresentativo del fenomeno di rottura in esame. In particolare in questo progetto è stato proposto un nuovo kernel di rottura basato sulla funzione di Weibull, implementando un bilancio di popolazione in termini massivi. L'obiettivo è quello di riuscire a modellare fedelmente un processo discontinuo di macinatura. Sia la stima dei parametri che una successiva analisi di sensitivitá sono state effettuate. Il modello si dimostra adatto a rappresentare i dati sperimentali e risulta particolarmente efficace per descrivere distribuzioni bimodali. Tale modello è stato successivamente migliorato; alla fine del refinement il modello consta solamente di un parametro in funzione della porositá dei nastri. L'accuratezza delle predizioni é stata sperimentalmente verificata.

Contents

Chapter 1

Introduction

1.1 Background

One of the preferred dosage way for any type of drug is the tablet. In pharmaceutical industries, three different processes can be adopted for tablet production: direct compression, wet granulation or dry granulation.

- Direct compression consists of the filling of the material into a die followed by the compression and the ejection of the tablet. This process is suitable for mixtures that have good flowability and can be well mixed, thus no granulation step is needed (Zhang et al., [42]).
- Wet granulation involves the production of granules with the addition of a liquid binder to the mixture of excipients and API in a granulator. After the granulation step the mixture is subjected to drying, followed by milling and compaction. Wet granulation is not used for materials sensitive to moisture and heat, because degradation can occur during drying (Miller, [22]).
- Dry granulation is the most common process used for materials sensitive to moisture and heat. In the dry granulation process the dry mixture is compacted into ribbons or flakes using a roll compactor, which are then milled (size reduction step) using a granulation machine and the granules obtained are introduced into the tableting machine for compaction.

Nowadays, dry granulation (DG) attracts notable interest of engineers and researchers, especially in the pharmaceutical industry, due to its distinct feature that no liquid binder is needed. It is normally expected that, as a size enlarge process, dry granulation would improve properties of feed powders (such as flowability), but it was

also reported that DG could cause a reduction in powder compactibility. In pharmaceutical industry, dry granulation involves two consecutive stages:

1. **Roll compaction**, in which the powder material is compacted through two counter–rotating rolls to form ribbons or flakes;
2. **Milling**, in which ribbons are milled into granules.

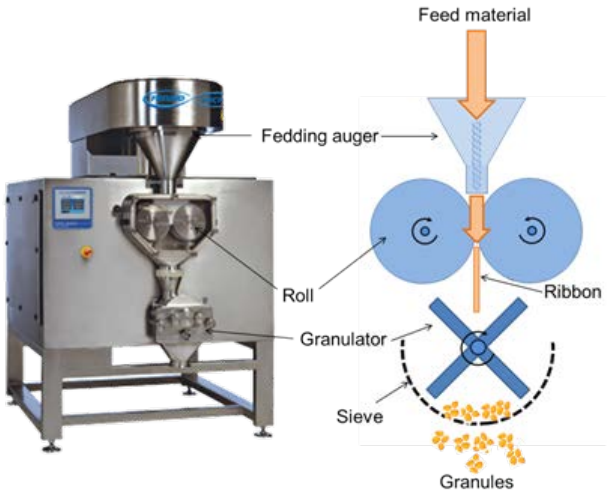

Fig. 1.1. A typical dry granulation process set up

The raising increase of interest in this process is owing to several advantages it offers compared to wet granulation, like the absence of solvents or water in the process, which is noteworthy to those substances sensitive to moisture. Another advantage of RCDG (roll compacted dry granulation) is that no liquid binder is needed so that no drying operation is necessary. Hence this technique is the preferred agglomeration process for formulations involving substances sensitive to moisture or heat [15].

In dry granulation processes of pharmaceutical materials the milling is a commonly used method to produce granules from roll compacted ribbons [15]. Dry granulation is particularly beneficial when dealing with active ingredients that are heat or moisture sensitive and therefore cannot be wet granulated [3], [10], [12]. Unfortunately, from roll compaction the produced ribbons and flakes generally have non–uniform porosity distribution and this will result in a wider granule size distribution. The wider the granule size distribution, the more difficult the control during the downstreams pharmaceutical operations. Gamble et al. [11] observed that an increase in ribbon porosity results in broader particle size distribution and reduces granule flow properties due to a greater volume of fine particles. It was proved that weaker ribbons tend to form finer granules under a given milling condition [35]. For this reason the size distribution of the granules is also affected

by the strenght of ribbons [2], [19], [20]. In this study, it was decided to produce from die compaction a *circular shape* ribbon, (large tablets as thin as possible) trying to mimic the traditional rectangular figure. The production of several ribbon batches with different and better controlled porosities was the basis of this work. Another outstanding problem in the dry granulation is the uncontrolled generation of fines, which Bacher [5] defined as particles smaller than 125 μm. An excessive amount of fines leads to manufacturing problems, such as poor flow, which may result in high tablet weight variation due to inconsistent die filling during tableting and unacceptable content uniformity due to segregation of fines from coarse granules [17], [26], [36]. To overcome this issue, on industrial scale, fines are often regranulated to improve the yield. However, a negative impact of recycling on API-conformity was evidenced [33]. One attempt to reduce the number of fines was made by Bultman [8] who studied the effects of multiple roll compactions on microcrystalline cellulose granules (Avicel PH 101). A Gerteis® roll compactor was used to re–compacted the granules for 10 times at fix process conditions (*i.e.* roll gap, roll speed and compaction pressure). The results showed a reduction of fines producing granules with an additionally increase of flowability and increased granule size. However, the final tablet tensile strength was reduced (*i.e.* lost in compactibility) and they attributed that to the loss of plastic deformability that the granules have after each recompaction step. Therefore there is a research gap regarding the control in the generation of fines. They should be minimized during the dry granulation, and one of the objective of this study is to identify what is the optimum process condition that satisfies the minimization. A mathematical method was adopted to accomplish the previous purpose. The population balance model (PBM) approach is widely used to model breakage, crystallization and settling processes in various industries, such as mining, food, chemical, metal and pharmaceutical. Modelling breakage processes with PBMs requires the formulation of a breakage kernel that represents the breakage phenomenon. The strength of the population balance model is its capability to predict the particle size distribution of the milled product as a function of the material properties and the design and operational variables of the mill. Reynolds [28] developed a mechanistic model of a conical screen mill. This allowed the mode of granule breakage to be investigated, and also was a useful tool to predict the size distribution of granules as a function of mill process parameters. Earlier also Motzi and Anderson [23] investigated the influence of screen size, impeller speed and impeller shape on aspirin granules. Through an analysis of variance they concluded that these three variables are all significant in the determination of the milled granule size distribution. Re-

garding the breakage mechanism, more recently Schenck and Plank [30] studied the milling of wet and dry agglomerates and concluded that the primary mechanism governing dry granule breakage was impact attrition. Based on this literature background, in this study a population balance modelling of the ribbon milling was developed, aiming to improve the predictive capability thanks to mathematical correlations between the input conditions and the model parameters.

1.2 Objectives

The overall aim of this study is the optimization of the milling process, improving the predictive capability of the population balance model to prevent the large production of fines. However, in sight of the previous background review, to improve the consistency of the study ensuring a high control in the density distribution of the ribbons, the milling was performed on different batches of cylindrical ribbons produced through die compaction instead of using the classical roll compaction. A summary of the objectives is here presented:

- ✓ To prepare five batches of model ribbons at different porosities developing a quantitative and reproducible procedure;
- ✓ To characterise the granules obtained after the milling process keeping fixed conditions both from the size and shape point of view;
- ✓ To exploit the experimental data in order to estimate the model parameters;
- ✓ To explore the relationship between the feeding ribbon porosity and the model parameters;
- ✓ To refine the model proving the parameters identification through sensitivity;
- ✓ To validate the model turning out experimentally the numerical results.

1.3 Layout of the thesis

Chapter 1 provides a brief introduction to the literature background, objectives and thesis structure.

Chapter 2 presents the material and the experimental instrumentations used along the project. For each machine, a detailed description of the working principle is

reported. In the second part, the Chapter focuses on the MCC PH–102 characterisation, presenting the particle size distribution and the shape analysis.

Chapter 3 illustrates the process of die compaction to produce the simulated ribbons. A preliminary sensitivity analysis varying the operating variables allowed to identify the target ribbon batches for five different porosities. The quality of the die compaction process is assessed plotting the porosity distributions for all the batches. Finally, the compressibility analysis is introduced, presenting the well–established models that quantify the progress of the force along the deformation and the energy requirement.

Chapter 4 describes the milling process reporting the experimental results and characterises the granules in terms of size and shape distribution, as done in Chapter 2 for the powder.

Chapter 5 is totally dedicated to the numerical part of the study. In the first of the Chapter, the population balance model is introduced, putting forward the several functions and parameters involved. Afterthat, the parameter identification was performed using experimental data collected by a previous MSc student referred to the traditional rectangular ribbon shape. This first application of the model led to interesting results and helped to get familiar with the numerical simulation. The second part of the Chapter addresses the population balance model applied to the experimental data collected from the milling of the simulated circular ribbons. Through a sensitivity analysis the model has been refined up to a unique parameter dependent of the ribbon porosity. In the end, the model was validated both within and outside the experimental domain. Finally, through the final predictions, it was possible to tackle the problem of fines generation, identifying the optimum process condition capable to minimise this issue.

Chapter 6 discusses the mechanistic analysis of powder and granules compression. The application of the Heckel and Kawakita models allowed to quantify the progress of the pressure along the deformation, proved to be porosity–dependent. Furthermore, the compression process was characterised also from the energy point of view, focusing on the different behaviour between powder and granules.

Chapter 7 recaps and summarises the key results of study, suggesting possible future developments.

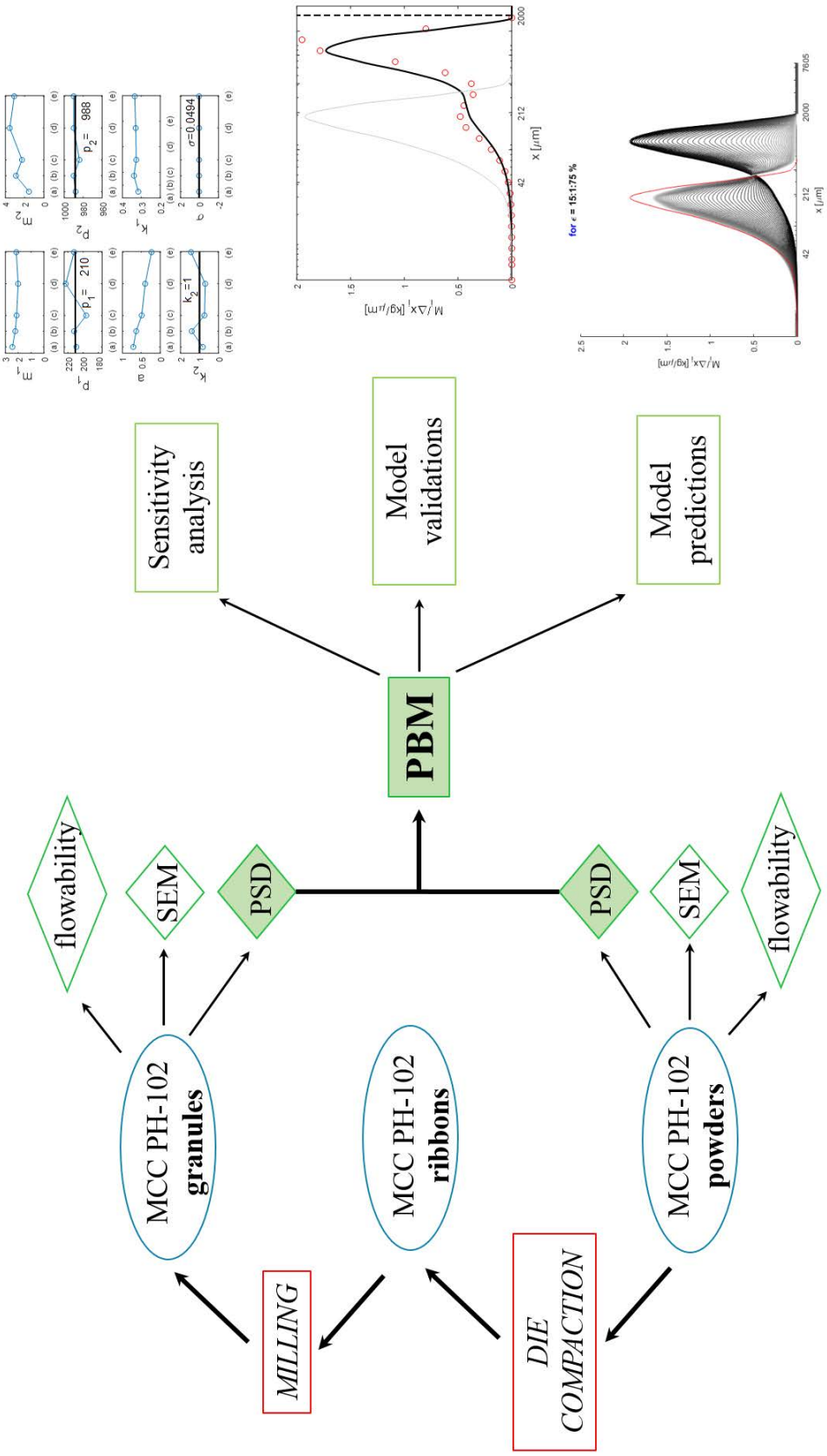

Fig. 1.2. Whole view of the study, from the experimental part up to the numerical modelling

Chapter 2

Materials & Experiments

This Chapter is divided into two main parts:

- description of the experimental equipments used during the project;
- powder characterisation according to size and shape analysis.

2.1 Die compaction

An Instron® universal testing machine with a 100 kN load cell (Figure 2.1) was used to produce circular ribbons as thin as possible using a die of 32 mm of diameter. For each experiment, a constant mass of 1000 ± 4 mg was compacted at different maximum pressures. The compaction was performed at room temperature (23°C) at a speed of 5 mm/min. The output experimental data plotting the force against the displacement were saved for the latter compressibility analysis.

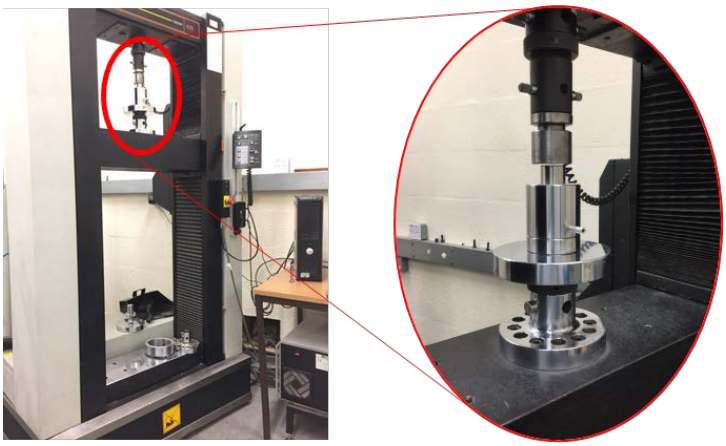

Fig. 2.1. Instron® press, with detail on the die

2.2 Particle size distribution

Adi et al. [1] defines a particle as 'a single entity comprising part of solid or liquid'. Usually, a set of particles is named monodisperse or uniform when they have the same size, while a sample of particles that have different size, shape and mass distribution is called polydisperse or non–uniform. A polydisperse system is characterised by a distribution of particle size. To describe this system, it is necessary to introduce a parameter, called equivalent diameter of a spherical particle, defined as the diameter of the sphere having the same value of a particular physical property as the particle of interest, such as volume, surface area or projected area. Several different equivalent diameters are available in literature (Seville and Wu, [32]) and their definitions depend of the type of method used to determine the particle size. Usually, various diameters can be measured from a single instrument for particle size characterization and this brings to different size results on the measurement of the same sample.
A dynamic analysis technique for size determination is the QicPic® (Yu and Hancock, [41]). QicPic is an image analysis technique including a light source for quasi-static imaging of fast moving particles with a double optical modules and a high speed camera. The QicPic can also be combined with a variety of dispersers, such as the RODOS disperser. It is used for all dry powder samples of size up to 1 mm. The particle size limits are 0.55 μm – 3 mm. The characterisation of the granule size distribution after the milling operation is essential to assess the quality of granules polidispersion.

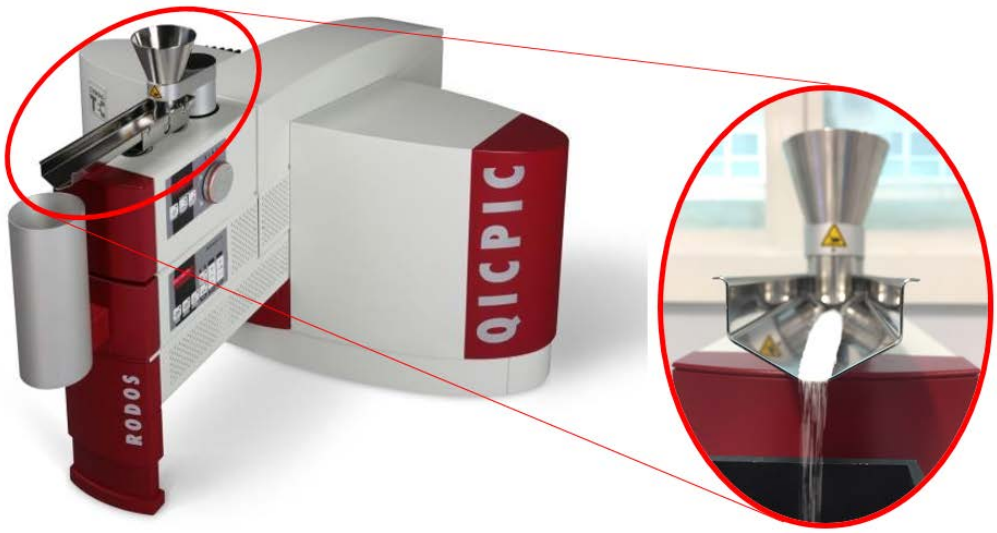

Fig. 2.2. QicPic SYMPATEC®, with detail on the feeding hopper

2.3 Particle shape analysis

Image analysis using SEM microscope (TM-1000, Hitachi®) was carried out for different granule batches at four different magnifications (x100, x150, x200, x700). The wide range of magnification allowed a more comprehensive shape characterisation in which both single and overall granules shape can be observed.

2.4 Mill

The milling process was carried out using a batch Retsch® cutting mill (Figure 2.3). Cutting mill is an highly intesitive mill, whose blades rotate at fixed 1500 rpm. In the upper part of the machine there is an hopper through which the inlet material is fed. Conversely, at the bottom there is a bin that collects the granules escaped from the mill thanks to the gravity force, once their size was small enough. The final fineness which can be achieved with the cutting mill depends on the aperture size of the exchangeable bottom sieve and the breaking properties of the sample material. During the experimental campaign, it was used a constant screen size of 2 mm. Unfortunately, there is a lack of operating variables using this type of mill, since the blades speed is fixed. For this reason, it was decided to investigate the effect of the ribbon porosity towards the milled granule size distribution, keeping constant both the milling time and the screen size.

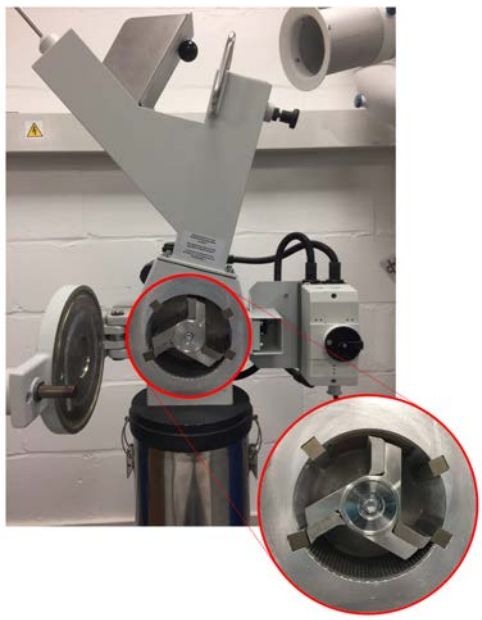

Fig. 2.3. Retsch® mill, with detail on the cutting region

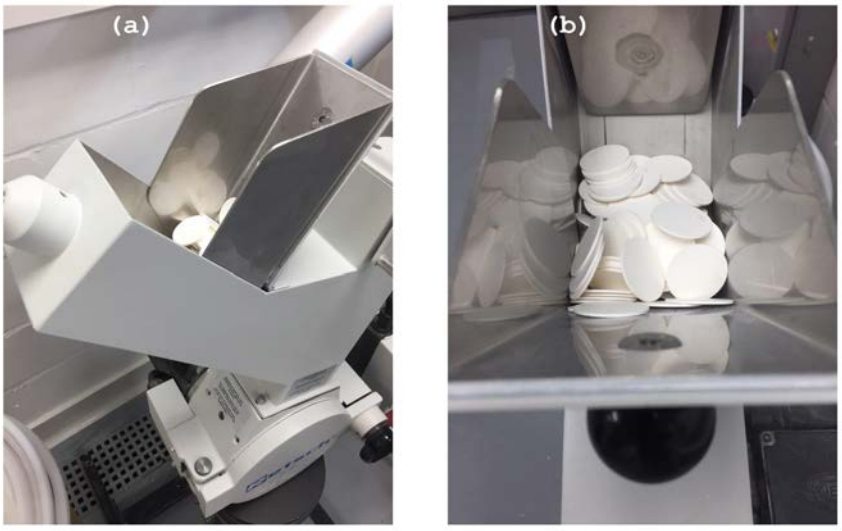

Fig. 2.4. (a) points out the mill hopper, (b) focuses on the feeding ribbons

Figure 2.4 illustrates the detail of the hopper. Each batch of circular ribbons consists of 20 elements. They were fed from the top and entered the cutting region once the machine was switched on. Each experimental run lasted 60 seconds.

2.5 Die filling

Among the mechanistic analysis performed during the study, one important characteristic that must be assessed is the flowability. In particular the study wants to prove that dry granulation can effectively enhance the flowability moving from powder to granules. To do that, die filling experiments were performed using a rotary device that better emulated the industrial application. It was used a squared die and the progress of the fill ratio for different shoe velocites was investigated.

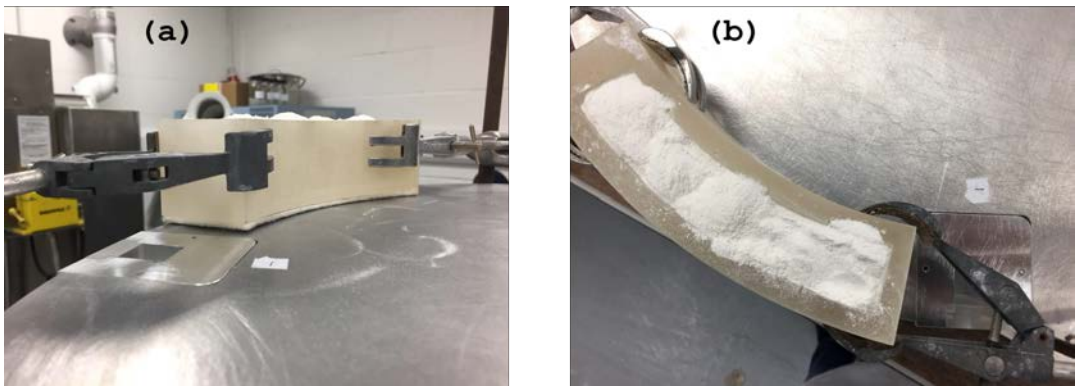

Fig. 2.5. Shoe details, (a) points out the front view while (b) illustrates the top view

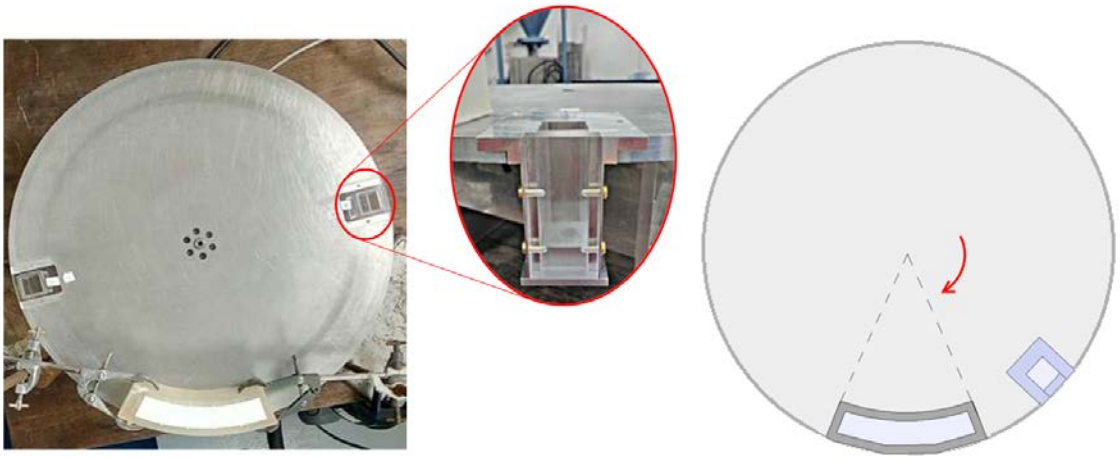

Fig. 2.6. Rotary die filling device, with fixed shoe and rotating plate

The velocity range explored during the experiments is [10, 220 mm/s]. The higher the plate velocity, the lower the fill ratio. This trend has been described by Wu et al. [38] according to an exponential law, wherein two parameters are involved:

$$\delta = \left(\frac{V_c}{V_s}\right)^n \tag{2.1}$$

where V_s is the shoe velocity and the critical fill speed V_c was defined as the highest filling speed at which the die can be completely filled. The die will not be completely full if the velocity is higher than the critical velocity. In this way it was possible to determine the fill ratio δ as the ratio between the mass deposited in the die at a given speed and the mass of a full die. n is another model parameter whose usual value is between 1–1.6.

2.6 Powder characterisation

This thesis project was totally dedicated to the excipient MCC PH–102 (Figure 2.7). Microcrystalline cellulose (MCC) is carbohydrate, white free-flowing, odourless and tasteless powders. It is a depolymerized cellulose prepared by treating alpha cellulose with mineral acids. The main source of MCC for pharmaceutical application derived from fibrous materials as wood pulp. The most common manufacturing process for MCC powders is the so called spray drying, in which controlling the process

Fig. 2.7. MCC PH–102 powder

conditions is possible to manipulate the particle size distribution and the moisture content. Microcrystalline cellulose is widely used in pharmaceutical formulations, primarily used as a binder/diluent in oral tablets and capsule formulations, furthermore, it is also used as lubricants and disintegrants that make it useful in tableting. It is used in either wet-granulation or direct-compression.
In this Section the results obtained from powder characterisation described in the previous sections are presented. More specifically, in Subsection 3.6.1 particle size analysis achieved by QicPic will be given, whereas particle shape using SEM analysis will be presented in Subsection 3.6.2.

2.6.1 Particle size analysis

Results obtained from QicPic analysis are presented in Figure 2.8, both as probability (black solid curve) and cumulative distribution functions (red solid curve). The yleft–axis reports the probability distribution in terms of volume p_3. Practically, the image analysis technique yields its results based on the equivalent diameter of a spherical particle, defined as the diameter of the sphere having the same value of the particle projected area. The probability distribution provides a great optical representation and makes it easy to visually determine the main body of particles. For instance, it is possible to detect modes of the distribution more easily from this type of distribution diagram. On the other hand, the cumulative distribution shows the percentage values, making it easy to identify the d_{50} *i.e.*.

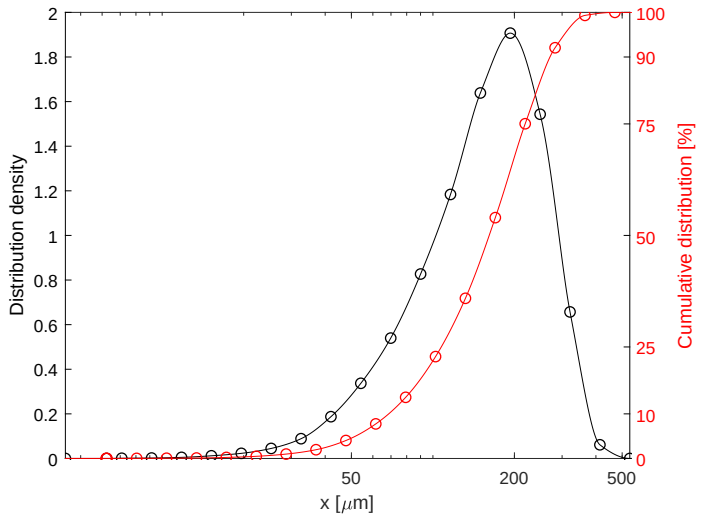

Fig. 2.8. MCC PH–102 particle size distribution

Figure 2.8 shows that the MCC–PH102 has a single mode. To quantitatively characterise the distribution, Table 2.1 summarises the main percentiles and the span.

Tab. 2.1. Particle size distribution parameters obtained from QicPic

$\mathbf{d}_{10}$ $[\mu m]$	$\mathbf{d}_{50}$ $[\mu m]$	$\mathbf{d}_{90}$ $[\mu m]$	Span ψ $[-]$
68.64	161.40	270.60	1.25

Table 2.1 sums up the major distribution parameters. For instance, d_{50} corresponds to the particle diameter at which the 50 % of a sample's mass is smaller than and 50 % of a sample's mass is larger than. Statistically, the d_{50} is exactly the median of the distribution. Furthermore, the span of distribution, named as ψ, gives an indication of how far the 10 % and 90 % points are apart, normalized with the midpoint. In practice, the span is a statistical descriptor of the width of the distribution. The smaller the value, the narrower the distribution. It is formally calculated as:

$$span\ \psi = \frac{d_{90} - d_{10}}{d_{50}} \tag{2.2}$$

2.6.2 Particle shape analysis

Furthermore, from the QicPic analysis it was possible to plot also the progress of the sphericity (*i.e.* circularity) with respect to the particle size.

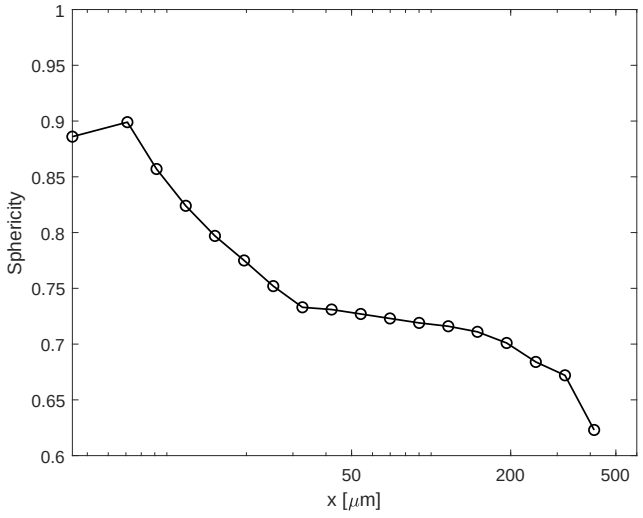

Fig. 2.9. Powder sphericity plotted against particle size

The sphericity is the ratio of the perimeter of the circle with the same projected area as the particle to the measured perimeter of the projected particle. The closer to 1, the smoother the surface. Mathematically, the sphericity Ψ is defined as:

$$\Psi = \frac{2\sqrt{\pi A_p}}{P} \tag{2.3}$$

where A_p is respectively the projected area of particles and P is the perimeter. From Figure 2.9 it is clear that the sphericity for the MCC PH–102 powder is around 0.71, since most of the distribution is located within the range [50, 250 μm]. Therefore, through image analysis it was possible to perform also a shape characterisation which is consistent with the images taken by the SEM. Indeed Figure 2.10 illustrates the morphology of MCC PH–102. Images at different magnification were taken to better capture the profile of the particles. The reported sizes (detail in the following figure) are consistent with the results achieved from the particle size analysis. From Figure 2.10 one can appreciate how the larger particles tend to assume an acicular shape, by far different from any spherical geometry. Finally, the SEM shape analysis agrees with the QicPic results since Ψ=0.71 is quite far from 1. SEM images reveal that MCC PH–102 has a prism morphology, consistent with the results obtained from Hughes et al. [16].

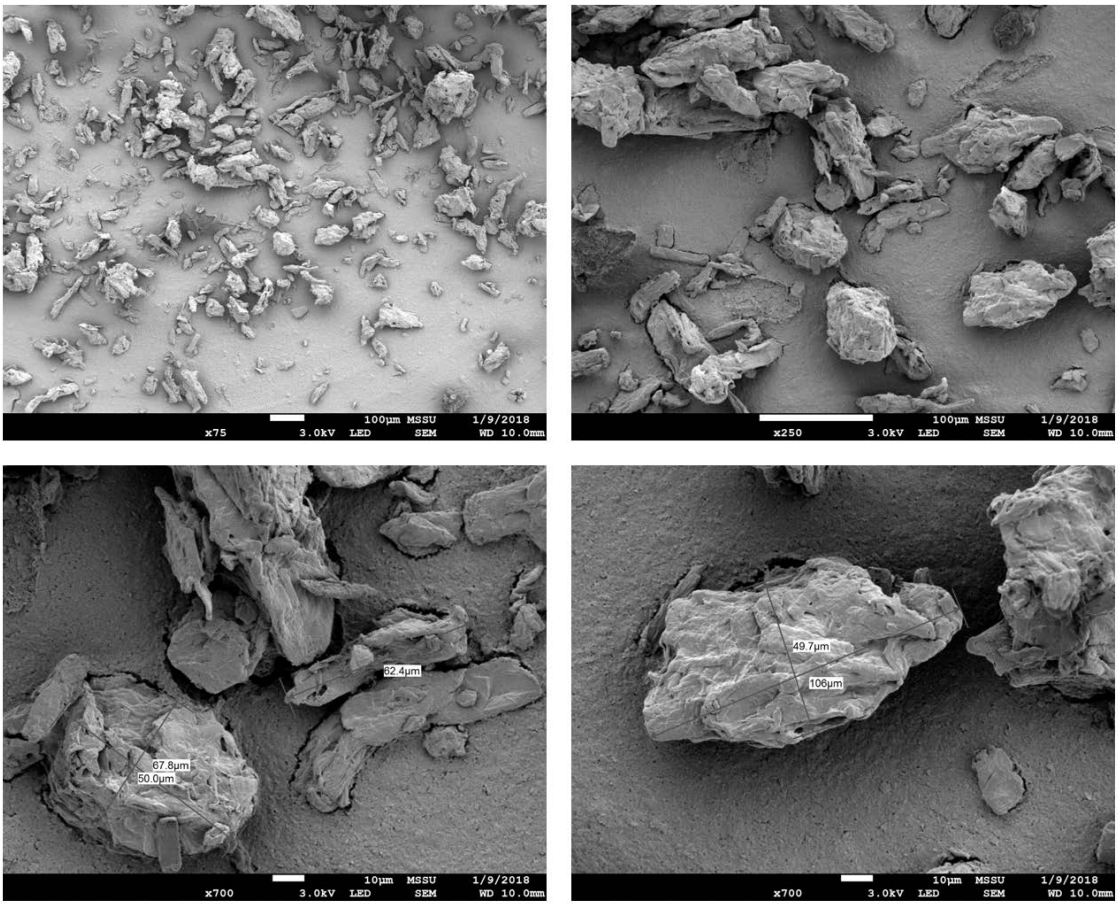

Fig. 2.10. SEM images at different magnification (x75, x250 and x700)

Chapter 3

Die compaction

3.1 Model ribbons production

In this Chapter, the first step of the dry granulation process is described: the production of ribbons. The aim of this process is to move from the powder state to the new form of ribbon, basically through uniaxial compression. The traditional approach for producing ribbons involves the usage of a roller compactor, but the produced ribbons and flakes generally have non–uniform density distribution, which leads to a much wider granule size distribution after milling [2], [19], [20], [21]. Indeed, since the stress distribution during the roller compaction is not uniform, density variations in ribbons are inevitable. For example, the ribbon density is usually lower at the edges than in the middle [14], [37]. Therefore the research question that triggers the first part of project was:

Can we produce ribbons with better controlled density distribution in order to ensure a better quality of the final granules after the milling?

Instead of the roller compactor, to tackle the previous research question, simulated ribbons were produced, *i.e.* circular tablets with large diameter (32 mm) prepared by die compression of accurately weighed powder under controlled conditions. The thickness of the circular tablets was reduced as much as possible to mimic the typical ribbons shape (Figure 3.1). Although tedious to prepare sufficient samples for milling, ribbons prepared by this approach had minimal uncontrolled ribbon density variations. This kind of procedure was discontinuous and

therefore suffered from dead times, but on the other hand offered a better process controllability. In particular, in sight of the further analysis, the control on the ribbons porosity must be ensured.

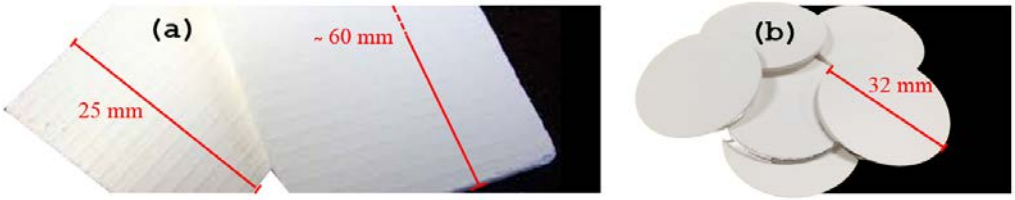

Fig. 3.1. (a) traditional rectangular shape, (b) proposed circular shape (*tablet*)

As described in Chapter 2, the machine used for the powder compression is the Instron® universal testing machine, equipped with a 100 kN load cell.
For each experiment, a constant mass of 1000± 4 mg was compacted at different maximum pressures leading to different tablet porosities.
Figure 3.2 illustrates the experimental set up for producing the ribbons. It was reported also the total time per run, given as the sum of dead and process times.

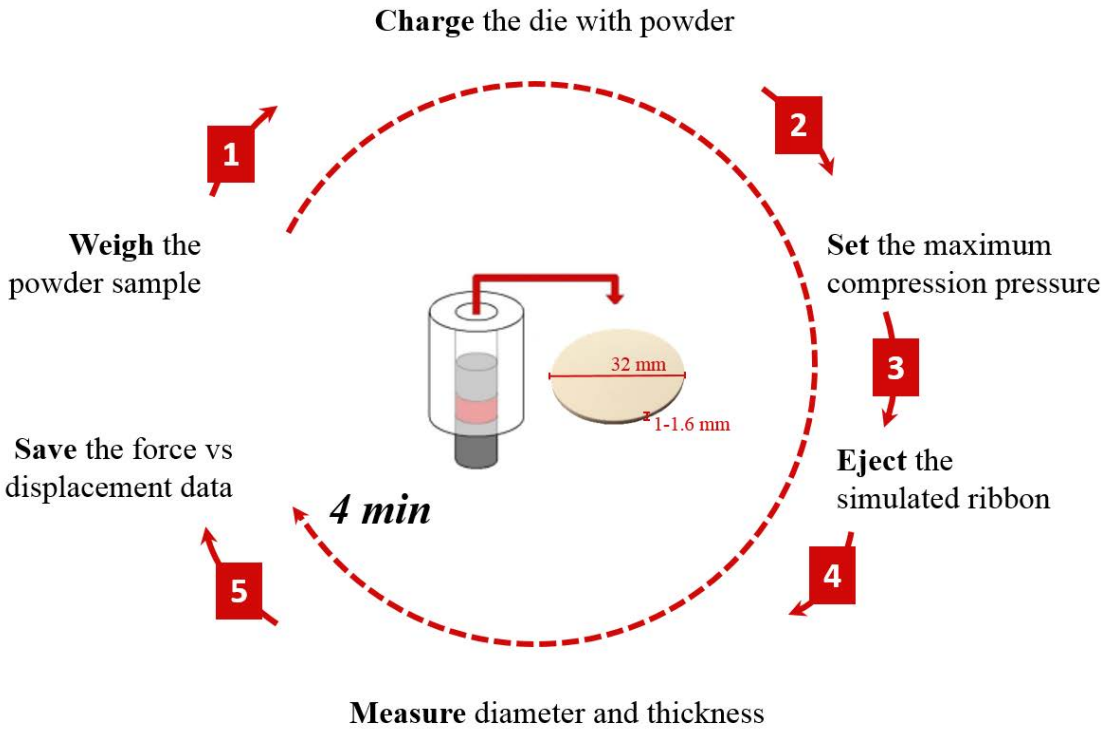

Fig. 3.2. Die compaction batch process

As a preliminary investigation, a sensitivity analysis was performed in order to assess what is the porosity distribution as a function of the uniaxial compression. First of all, it is important to define how the porosity has been computed. In order to do that, let us recall the definitions of bulk and true density as follows:

$$\rho_{bulk} = \frac{M_{tablet}}{V_{tablet}} \tag{3.1}$$

The bulk density is defined as the ratio between the mass of the tablet and the volume of the tablet, whose major dimensions (thickness and diameter) were measured with a calliper.

$$\rho_{true} = \frac{M_{solid}}{V_{solid}} \tag{3.2}$$

The true density is defined as the ratio between the mass of the solid and the volume of the solid; its value was measured with an Helium Pycnometer (*AccuPyc II 1340, Micromeritics, UK*). The model ribbons porosity ε is hence defined as:

$$\varepsilon = 1 - \frac{\rho_{bulk}}{\rho_{true}} \tag{3.3}$$

In the following `subplot` visualization, the results of the sensitivity were displayed.

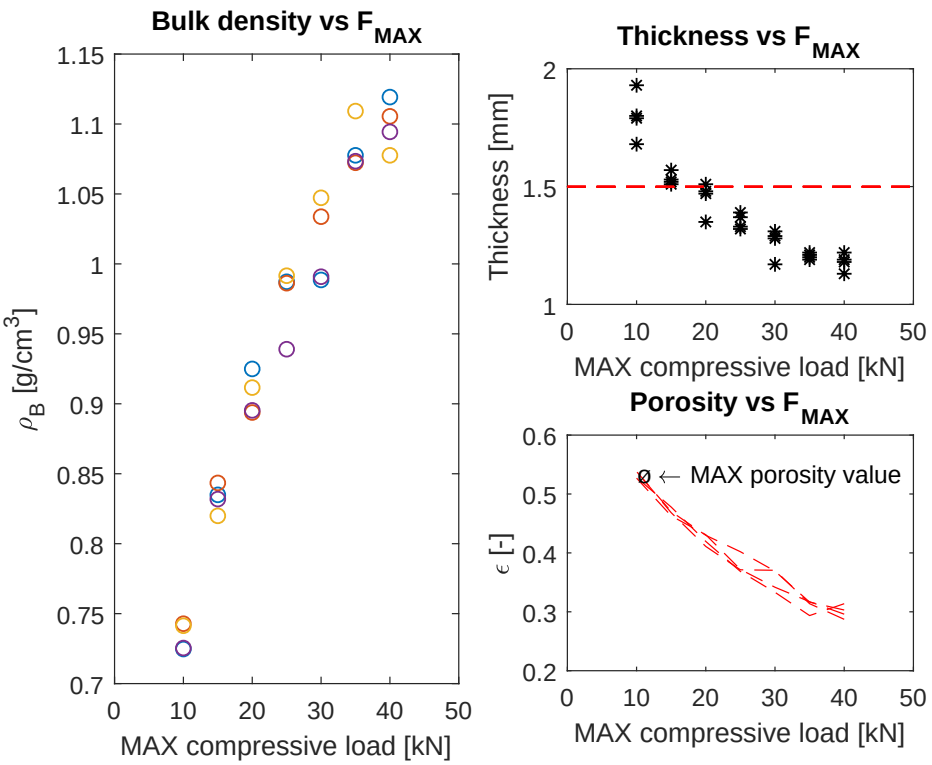

Fig. 3.3. The dependence of ρ_{bulk}, thickness and porosity on the maximum compression load

As expected, the higher the maximum compression load, the higher the bulk density. This result of course is straightforward related to the porosity reduction, since the void spaces between particles are going to decrease when the compression load is increased. Since one of the goal of this controlled compression was to keep, as small as possible, the thickness of the tablet, a maximum value of 1.5 mm has been set (horizontal red dashed line). Through the experiments, it was observed that a maximum compressive load of 10 kN was not capable to produce handleable tablets. Analysing the previous results, it was decided to produce five batches of ribbons with different porosities:

- ◇ maximum compression load of 15 kN $\Rightarrow$ Porosity $\varepsilon = [45\% - 48\%]$;
- ◇ maximum compression load of 22.5 kN $\Rightarrow$ Porosity $\varepsilon = [38\% - 41\%]$;
- ◇ maximum compression load of 30 kN $\Rightarrow$ Porosity $\varepsilon = [33\% - 37\%]$;
- ◇ maximum compression load of 45 kN $\Rightarrow$ Porosity $\varepsilon = [25\% - 29\%]$;
- ◇ maximum compression load of 60 kN $\Rightarrow$ Porosity $\varepsilon = [22\% - 25\%]$;.

Figure 3.4 illustrates the probability distributions of ribbon porosity for each batch:

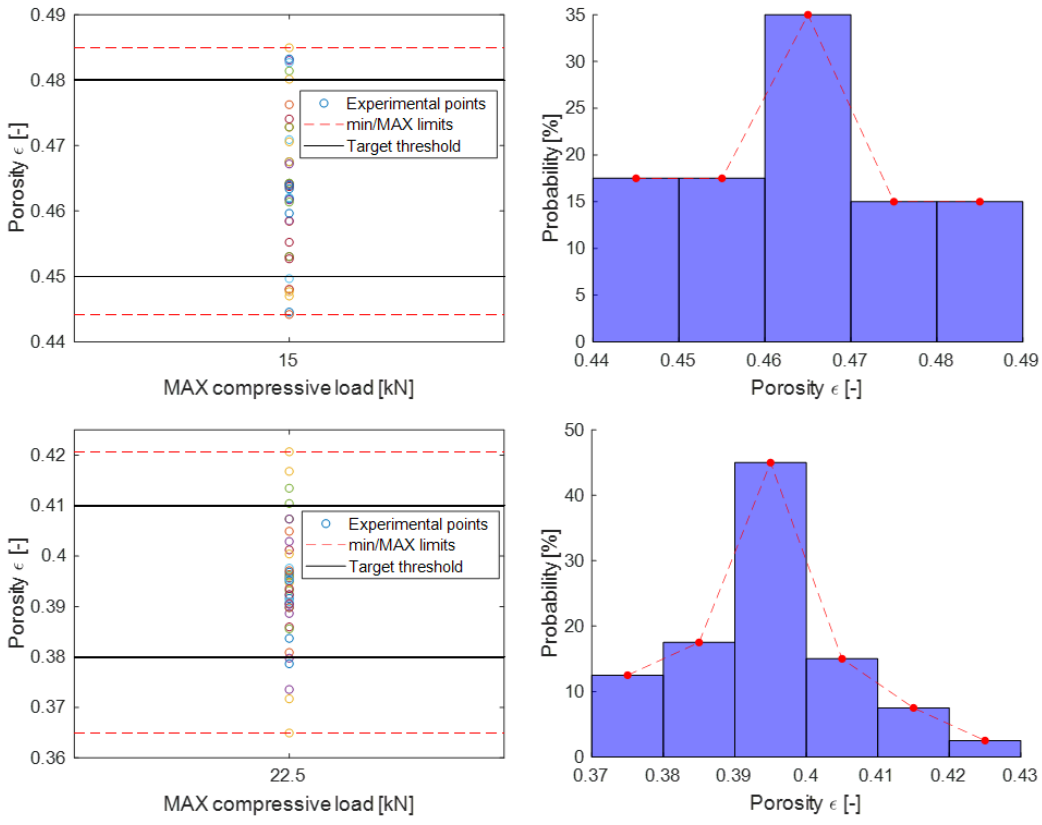

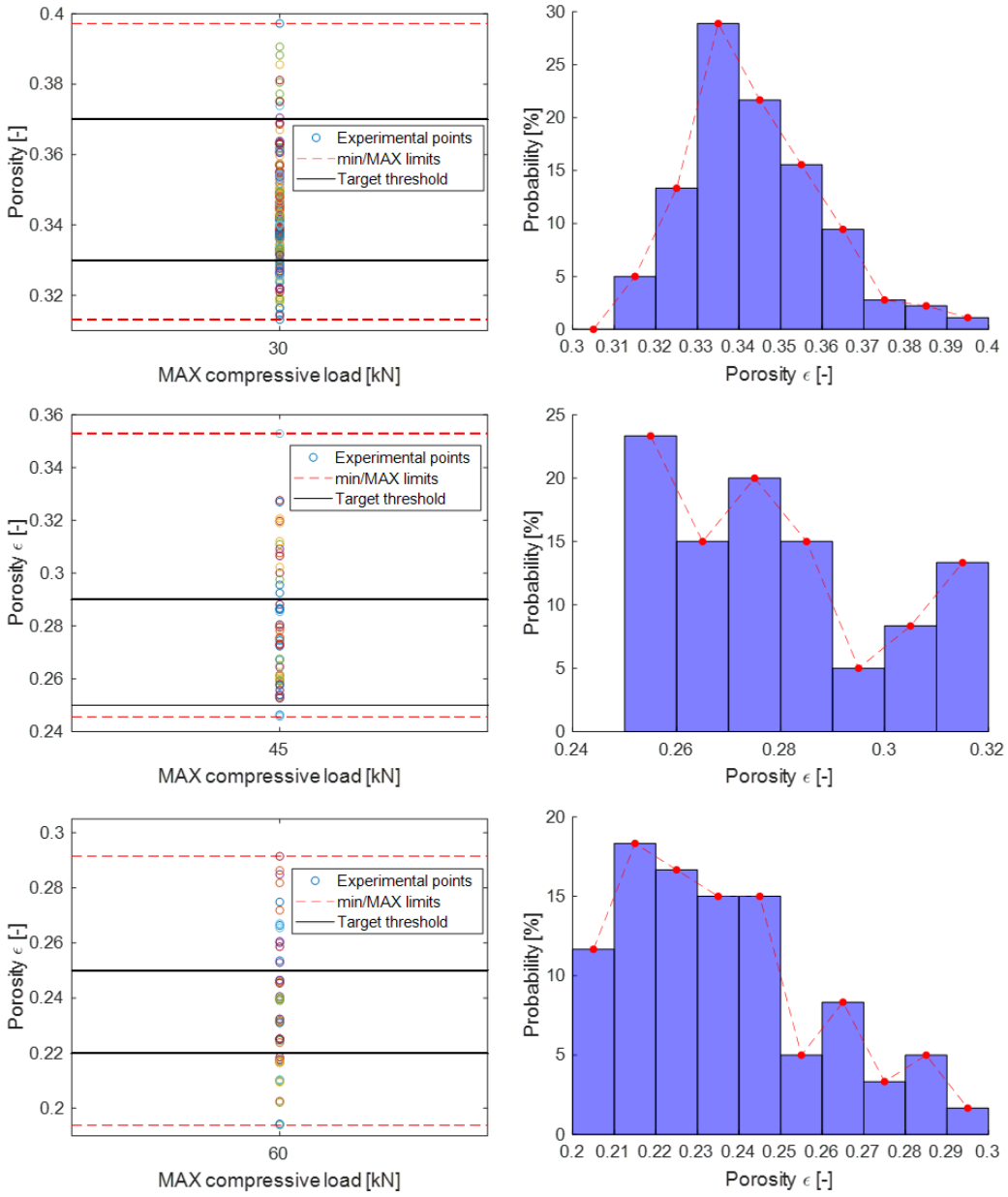

Fig. 3.4. On the left–hand side of the plot there are the porosity ε scatter plots, while on the right–hand side there are the % probability distributions of ribbon porosity

Tab. 3.1. Porosity and number of samples for the five ribbon batches

	#1	#2	**#3**	#4	#5
up to	15 kN	22.5 kN	30 kN	45 kN	60 kN
n° samples	40	40	180	60	60
ε [%]	46.7 ±2.3	39.4 ±2.3	34.3 ±3.2	27.3 ±3.3	23.8 ±4.5

Since for the die filling experiments a huge amount of material was required, just for the third tablet batch 180 tablets have been produced. For the other families,

a lower number of tablets was performed. As it can be noticed from the previous probability distributions (Figure 3.4), just the one plotted for a maximum compressive load of 30 kN looks like a gaussian curve. That's because for the other tablet families a lower number of samples was drawn and therefore the *central limit theorem* has been just partially fulfilled.
Generally, the density distribution in real ribbons prepared through roller compaction is not homogeneous. On the contrary, the implemented experimental technique of producing model ribbons through die compaction perfectly succeeded and it ensured a proper density distribution control. Indeed, the largest % of ribbons is located within the target region for each batch. The variability in the ribbon porosity goes up increasing the maximum compression load, meaning that assuring a tight control in the density distribution becomes more difficult.

3.2 Compressibility analysis

Exploiting the raw data achieved by the compression experiments, a compressibility analysis of the process was developed. When a bulk solid is compressed, it will deform, which may be accompanied by rearrangement of constituent particles, resulting in collapse of voids if the compression pressure is low, and deformation of individual particles if the pressure is high [32].
The extent of deformation under a certain compression pressure depends on the material properties. To characterise the ability of bulk solids to deform or consolidate during compression, the concept of compressibility is introduced. Indeed the knowledge of compressibility is very useful in understanding densification and compaction processes. In particular it describes how the bulk density, solid fraction or porosity change with the applied pressure. Various mathematical models and empirical fits to data have been developed and among these, the Heckel and Kawakita equations are widely used.

3.2.1 Heckel equation

Basically the Heckel model assumes that the densification process under pressure can be approximated as a first–order rate process. Mathematically, this gives:

$$-\frac{d\varepsilon}{dP} = k\varepsilon \tag{3.4}$$

The integration of Eq.(3.4) will provide the following law:

$$ln\left(\frac{1}{1-\rho_R}\right) = kP + A \tag{3.5}$$

where ρ_R is the relative density, given as the ratio between the bulk and the true density, whereas k and A are two model parameters. In particular, k is a material-related parameter and is inversely related to the mean yield pressure of the bulk solid, while A is a parameter related to the densification due to die filling and rearrangement of particles.

From the force vs displacement data from the press machine, it was possible to fit the experimental data to identify the values of the parameters involved in the model. In Figure 6.3 both the loading and unloading curves are reported. The loading part is highlighted with respect to the unloading contribution which has been made transparent. According to the Heckel analysis, plotting $ln(1/1-\rho_R)$ against the compression pressure P, a linear relationship can be obtained.

The parameters k and A can be easily estimated through linear regression and are reported in the following table:

Tab. 3.2. Parameters k and A estimated after linear fitting

Material	**k [MPa^{-1}]**	**P$_y$ [MPa]**	**A [-]**
MCC PH-102	0.0192	52.08	0.347

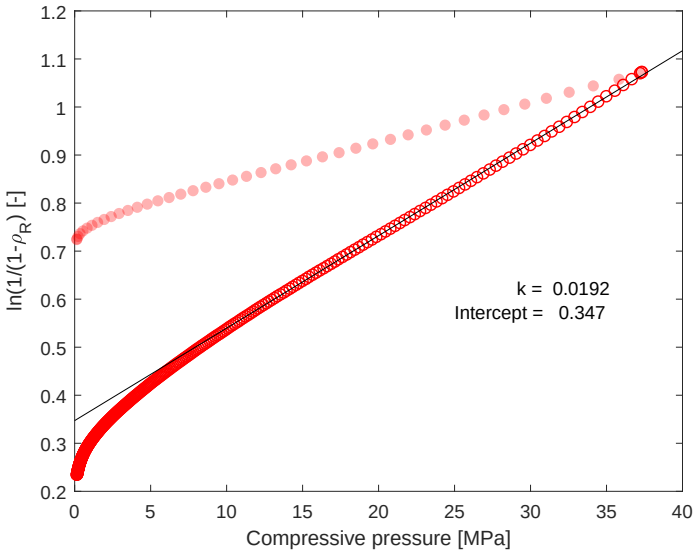

Fig. 3.5. A typical Heckel plot, based on a run up to 30 kN

The P_y value is called the Heckel yield stress, defined as:

$$P_y = \frac{1}{k} \tag{3.6}$$

Robert and Rowe (1987) proposed a criterion to classify powder materials based on the Heckel yield stress, which is presented in Table 3.3. In view of the above calculation reported in Table 3.2 and according to the Robert & Rowe criterion, the MCC PH–102 is classified as soft powder.

Tab. 3.3. Robert & Rowe (1987) powder classification criterion

$\mathbf{P}_y$	**Compression Characteristics**
< 40 MPa	Very soft
40~80 MPa	Soft
80~200 MPa	Intermediate
> 200 MPa	Hard

3.2.2 Kawakita equation

Kawakita and Ludde also analyzed the volume reduction of bulk solids with applied pressure during compression. The Kawakita model is given as:

$$C = \frac{V_0 - V}{V_0} = \frac{abP}{1 + bP} \tag{3.7}$$

where C is the degree of volume reduction, V_0 is the initial volume of the bulk solid, V is the volume of the bulk solid at pressure P, a and b are two constants. Let us re–arrange Eq.(3.7) as:

$$\frac{P}{C} = \frac{P}{a} + \frac{1}{ab} \tag{3.8}$$

For given compression data, one can plot P/C as a function of the compression pressure, which is often referred to as the Kawakita plot (Figure 3.6).
In particular, the parameters a and b are two material constants with a indicating the initial powder porosity before compression and b being a constant related to the yield stress of particles.
As before, the loading contribution is highlighted with respect to the unloading one. Looking at the linear relationship obtained, through linear regression is again possible to determine the constants a and b. The slope from the the linear part of the plot gives the reciprocal of constant a, while the intercept of the fitted straight line at the P/C axis gives the value of $1/ab$.

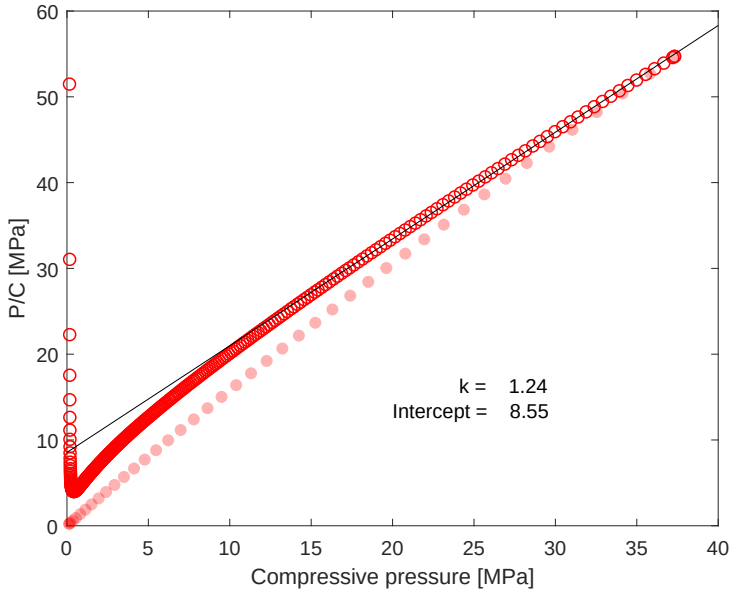

Fig. 3.6. A typical Kawakita plot, based on a run up to 30 kN

Tab. 3.4. Parameters a and b estimated after linear fitting

Material	**a** [-]	**b** [-]
MCC PH-102	0.806	0.145

The whole mechanistic analysis involving all the ribbon batches and the comparison between the compressibility of powder against granules will be developed in the Chapter 7.

Compressibility energy

In order to proper characterise the compression process, it is necessary to analyze the compressibility also concerning the energy point of view. As discussed above, the progress of the applied force against the deformation shows first a loading and then, when the applied pressure is removed, an unloading contribution. By definition, the area below the loading curve is exactly the energy required for the powder compression. Actually, it is also required to account for the energy release in case of elastic recovery.

$$\mathbb{E} = \int_0^{\gamma MAX} \mathcal{F}(\gamma) d\gamma - \int_{\gamma end}^{\gamma MAX} \mathcal{F}(\gamma) d\gamma \tag{3.9}$$

where $\mathbb{E}$ is the compressibility energy expressed in [J], $\mathcal{F}(\gamma)$ stands for the load-

ing part of the curve and $\digamma(\gamma)$ describes the unloading contribution. Therefore, starting from the experimental data provided by the machine, through a numerical integration approach implemented in MATLAB®, it was possible to assess the compressibility energy as the difference between the area below the **loading** curve and the area below the **unloading** curve.

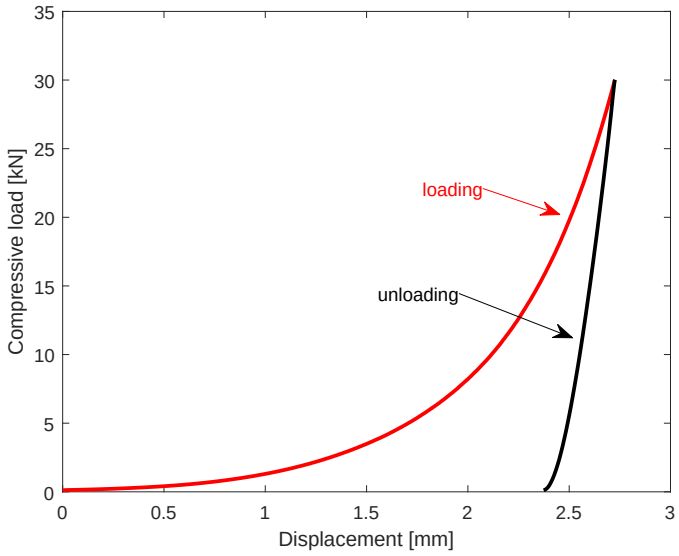

Fig. 3.7. Typical loading & unloading curves for powder compression up to 30 kN

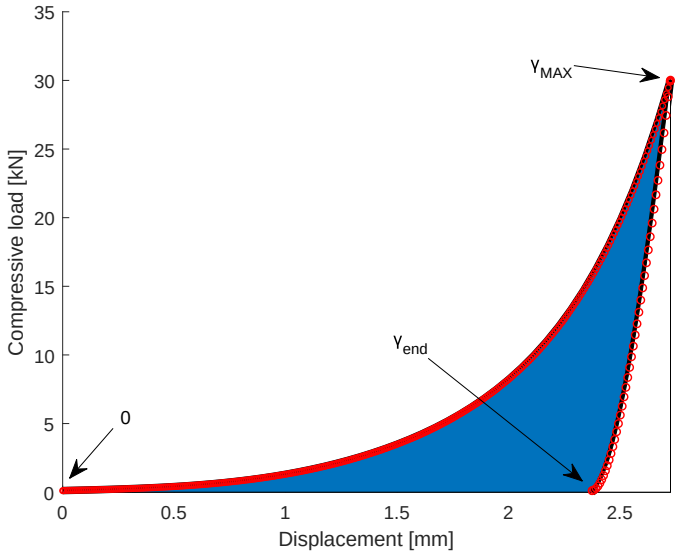

Fig. 3.8. Compressibility energy (blue area) for powder compression up to 30 kN

In the following Figure 3.9, the assessment of both the loading and unloading areas is reported. As defined above, the compressibility energy is given as the difference between these two areas.

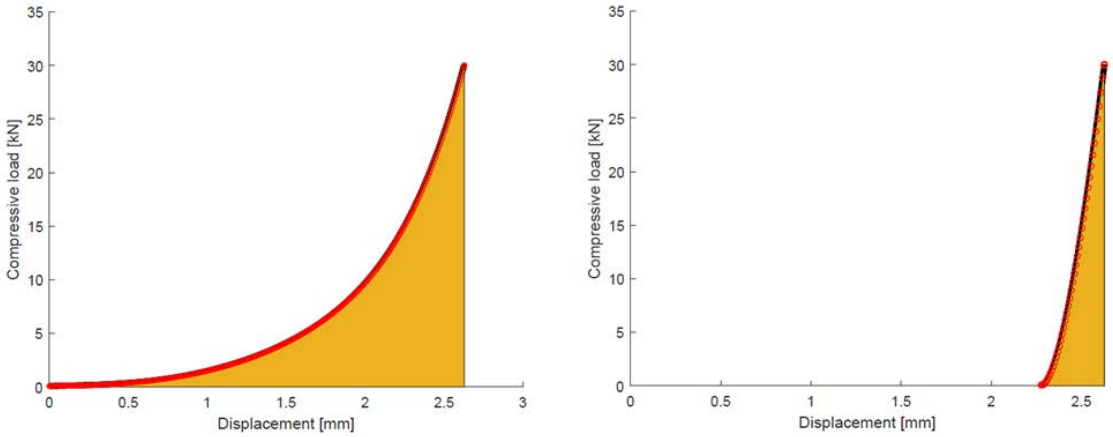

Fig. 3.9. Loading & unloading areas for powder compression up to 30 kN

Moreover, it is possible to define another important characterisation factor, called elastic recovery, as follows:

$$ER\,[\%] = \frac{unloading\ area}{loading\ area}\% \tag{3.10}$$

where ER is the elastic recovery, expressed as %.

Tab. 3.5. Compressibility energy and elastic recovery for powder compression up to 30 kN

Material	Energy [J]	ER [%]
MCC PH-102	12.42	24.36

The batch of tablets produced with the maximum compression load of 30 kN was taken as example to introduce the theoretical background behind the compressibility analysis. As mentioned above, the complete investigation of the compressibility phenomena will be fully analysed in the final Chapter. Anyway, for this first batch, Table 3.5 summarises the calculations of compressibility energy (assessed as reported in Eq. 3.9) and the elastic recovery (Eq. 3.10). In concluding, the aim of this third Chapter was to describe the passage from the powder state to the simulated ribbons. First of all, the five batches of tablets with controlled porosity have been presented. After that, the compressibility analysis background was introduced, presenting the first result referred to the illustrative case of the 30 kN batch. Both Heckel and Kawakita mathematical models like will be used to characterise the solids behaviour. Finally, the compressibility has been brought in also from the energy point of view, defining both the compression energy and the elastic recovery.

Chapter 4

Milling process & Granules characterisation

The beginning of this Chapter deals with the milling process, presenting objectives (§4.1) and results (§4.2). Then, following the same order of Chapter 2, Section 4.3 specifically addresses the granules characterisation aimed at comparing the main features. More specifically, in this current section granule size distributions for every tablet batch achieved by QicPic will be given. The morphological analysis using SEM analysis will be presented in Section 4.4. Finally, flowability characterisation through die filling experiments will be described in Section 4.5.

4.1 Objective

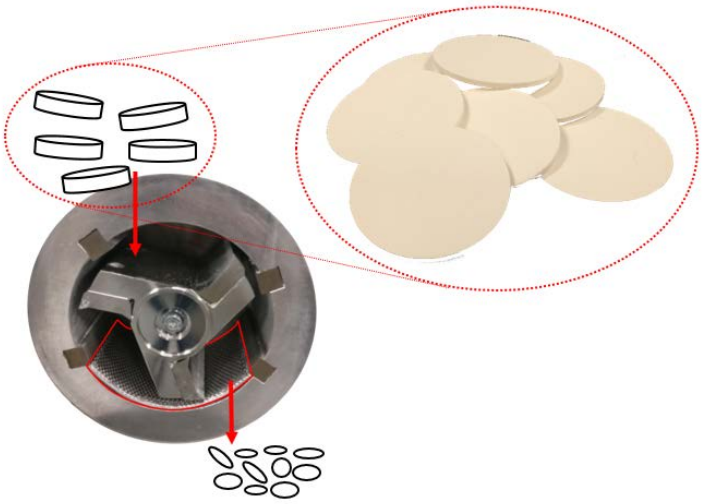

Fig. 4.1. Retsch® Cutting mill with detail in feeding tablets

Mills screen–equipped are widespread in the manufacture of solid oral dosage forms in the pharmaceutical industry. Mills are used for several purposes, ranging form coarse delumping of wet granules to fine control of granule size. The granule size distribution is an essential intermediate product attribute. For example, the granule size distribution can have a significant effect on uniformity of powder flow, and ultimately tablet weight uniformity. Additionally, control of the granule size distribution is important to minimise segregation potential during compression. Milling is therefore necessary to produce granules and is a crucial step for the dry granulation. Although milling is beneficial for the pharmaceutical industry, favouring bioavailability of drugs and granule homogeneity, it is a complex, inefficient, and not fully understood process. Complexity of milling arises from the variety of grinding mechanisms which occur during the comminution and from the material and process parameters involved. To improve the milling process, much research was conducted to enhance understanding of the basic mechanisms of breakage and attrition, in granulation [27]. Different milling techniques can be used based on the grinding mechanisms, such as cutting (or shearing), compression (or crushing), impact and attrition. Specifically in this project a cutting mill was used and the experimental procedure followed during the milling has been already explained in Section §2.4. The research question that set off the study was:

Can we improve the knowledge on the milling by implementing any predictive tool?

The objective of this introductive Chapter is to present the experimental results, quantitatively describing the milling process and characterising the granules produced. In Chapter 5, a numerical modelling approach based on the population balance will tackle the above research question.

4.2 Results

To quantify the performance of the milling operation, the efficiency η was introduced, defined as:

$$\eta\,[\%] = \frac{M_{OUT}}{M_{IN}} \tag{4.1}$$

where M_{IN} is the mass of material into the tablets feeding the mill, whereas M_{OUT} is the mass of material leaving the mill. Ideally, because of the mass conservation principle, the mill efficieny should be 100 %. Unfortunately, there were unavoidable losses of materials due to trapping phenomena into the machine. The following table summarises the process efficiency for the five ribbon batches:

Tab. 4.1. Milling efficiency η [%]

#1 15 kN	**#2** 22.5 kN	**#3** 30 kN	**#4** 45 kN	**#5** 60 kN
76.05	80.77	81.32	88.49	89.14

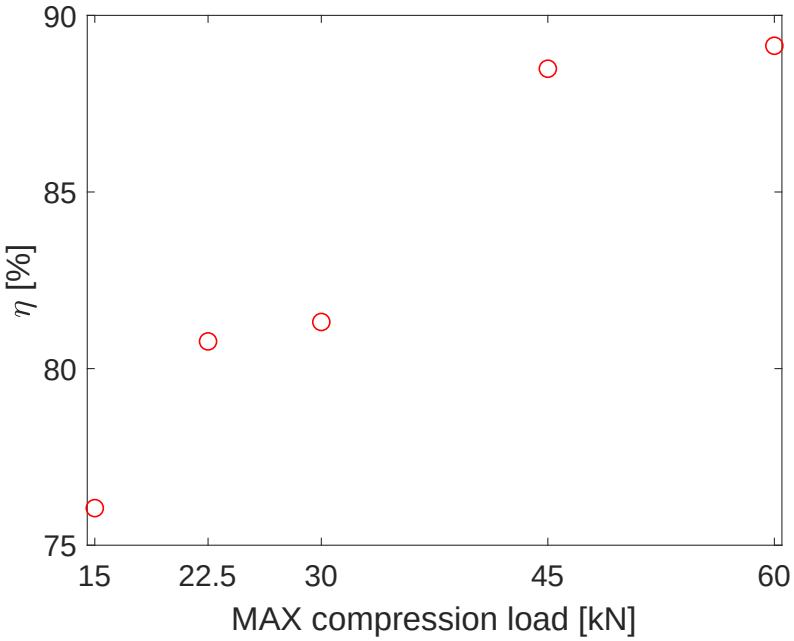

Fig. 4.2. Milling efficiency η plotted against the tablets batches

The higher the maximum compression load, the lower the amount of fines produced. Indeed, it is well–known that weaker ribbons tend to form finer granules under a given milling condition [35]. The major part of the losses are due to the fines, therefore the lower the fines produced, the higher the milling efficiency. The minimisation of fines would lead to an increase of milling efficiency and, more generally, to a better performance of the downstream operations.
After the milling characterisation, several analysis were performed on the granules produced. First of all, through the image analysis (QicPic®), the granule size distributions of all the granules batches were computed.

4.3 Granule size distribution analysis

Table 4.2 shows both the mean values and the standard deviations of the porosities for each tablet batch. Please notice that from now on, the highest porosity batch will be named with (a), whereas the lowest one will be indicated with (e).

Tab. 4.2. Porosity values for the five tablet batches

#1 (a)	#2 (b)	#3 (c)	#4 (d)	#5 (e)
46.7 ±2.3 %	39.4 ±2.3 %	34.3 ±3.2 %	27.3 ±3.3 %	23.8 ±4.5 %

The granule size distributions obtained from QicPic are presented in Figure 4.3. To avoid segregation phenomena and to guarantee a meaningful specimen, a careful sampling was performed before each measurement. Moreover, repeatability was ensured by repeating every measurement three times and the average values were considered.

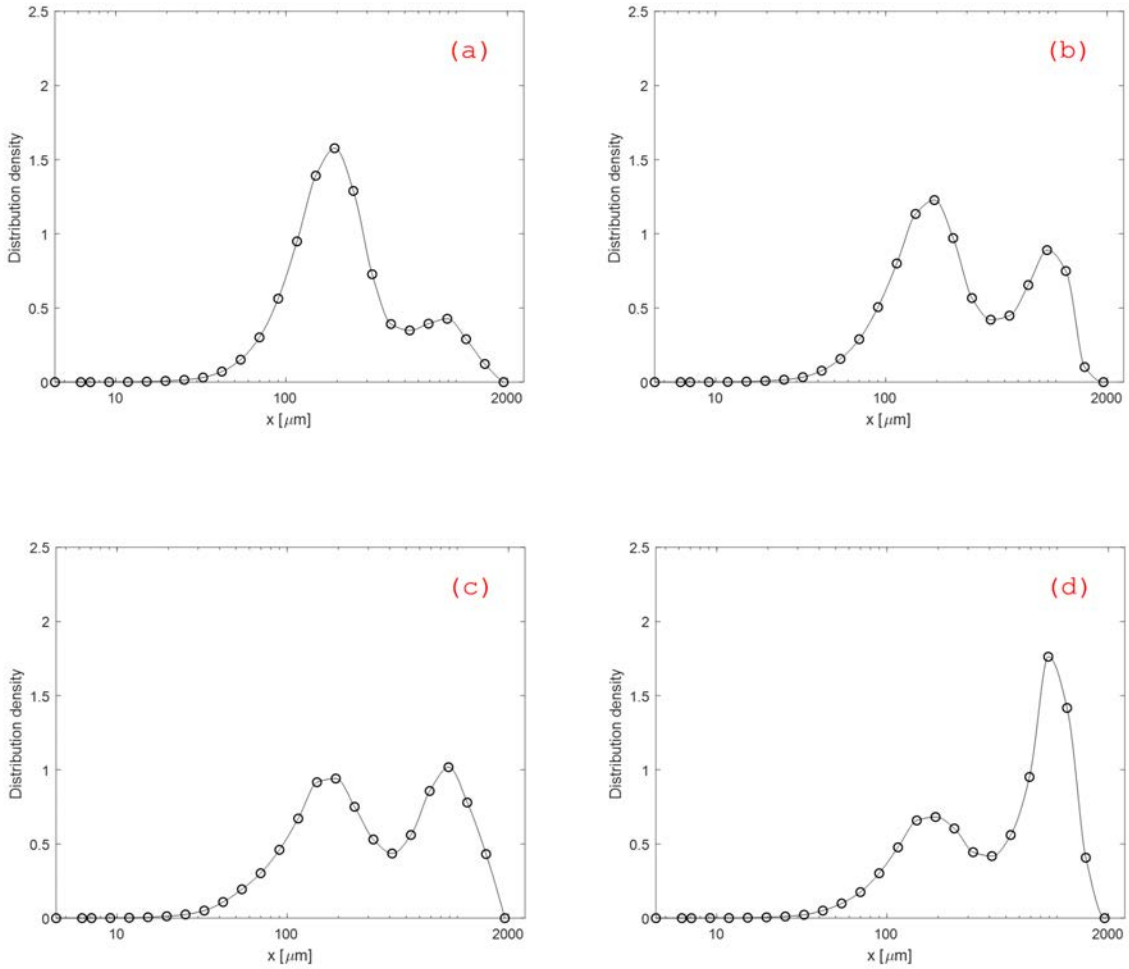

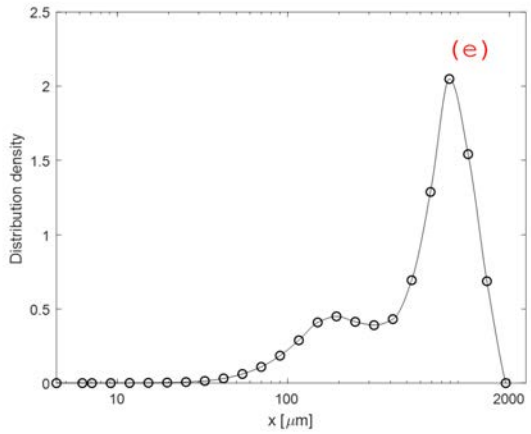

Fig. 4.3. MCC PH–102 granule size distributions for the five tablet batches

From Figure 4.3, it is clear that the porosity has a strong effect on the granule size distribution. All the distributions appear to be bimodal, meaning that two peaks are detected. The first mode corresponds to the fines; therefore that portion of the distribution is simply powder. The second mode corresponding to the granules family is brought out by the milling itself. Increasing the compression pressure and consequently decreasing the porosity of the ribbons, harder ribbons are produced. From the milling of these harder tablets, more granules are generated. This is the reason why moving from (a) to (e) the first mode decreases while the second one starts to prevail. From a process point of view, in order to optimize the dry granulation which aimed at producing as much granules as possible, it is clear that feeding harder ribbons in the mill is a better option, since more granules will be produced and the percentage of fines left after the milling will be reduced. The case (c) can be considered as a critical porosity value, since a further reduction in the ribbon porosity will end up to the domain of the second mode. Finally in (e) one can notice that the first peak flattens and all the material is roughly detected within the granules mode.

To quantitatively describe the distributions, some main parameters like the percentiles and span were calculated and the result is reported in the following table. Table 4.3 highlights the increase in the percentiles decreasing the ribbon porosity. Of course in sight of the comments referred to Figure 4.3, this is an expected result, since the largest amount of granules is obtained milling the hardest ribbons with low porosity. Moreover, it is also clear that the distribution span is much lower within the last two batches, since the width of the distribution is smaller. From a process control point of view, for sure it is preferred a more uniform granule size distribution and therefore a low distribution span value is a point of strength.

Tab. 4.3. Granule size distribution parameters obtained from QicPic

ε [%]	$\mathbf{d}_{10}$ [μm]	$\mathbf{d}_{50}$ [μm]	$\mathbf{d}_{90}$ [μm]	Span ψ [−]
(a)	92.38	202.40	751.66	3.25
(b)	93.98	237.44	1000.66	3.82
(c)	89.53	307.14	1116.10	3.34
(d)	116.67	606.10	1191.89	1.77
(e)	151.07	748.73	1254.90	1.47

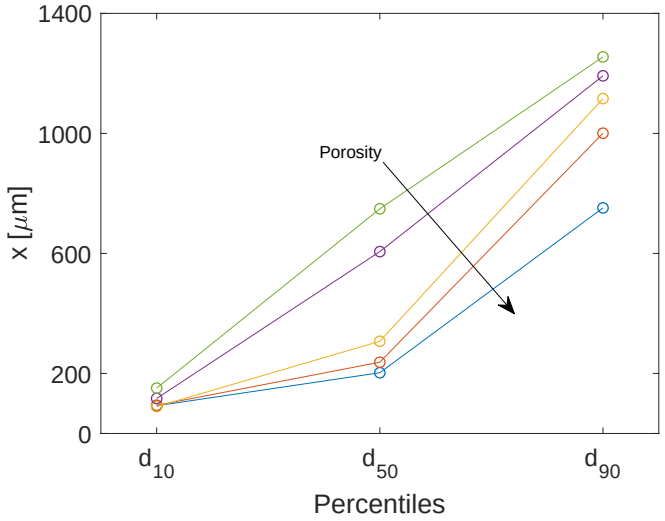

Fig. 4.4. Percentiles trend for the five ribbon batches

4.4 Granule shape analysis

To characterise the morphology of the granules, once again several SEM images were taken, considering just samples of the first (a), third (c) and fifth (e) batch. The availability of several images at different magnification allows to better understand the morphology of the granules, moving from an ensemble perspective up to the tiniest detail of a single granule. Figure 4.7 shows that the sample presents both powder and granules, consistently with the granule size distribution achieved by QicPic. Moreover, looking at x700 magnification image, the granules look to be made by an aggregation of acicular shape particles. Looking at SEM images referred to batch (c), it is clear that the proportion between granules and powder is increased compared to the previous situation. Furthermore, the granules shape seems to be more spherical compared to the needle shaped particles. This result will be quantitatively proved later through the QicPic analysis. Finally, batch (e) basically is made by just granules, since the fines are dramatically reduced.

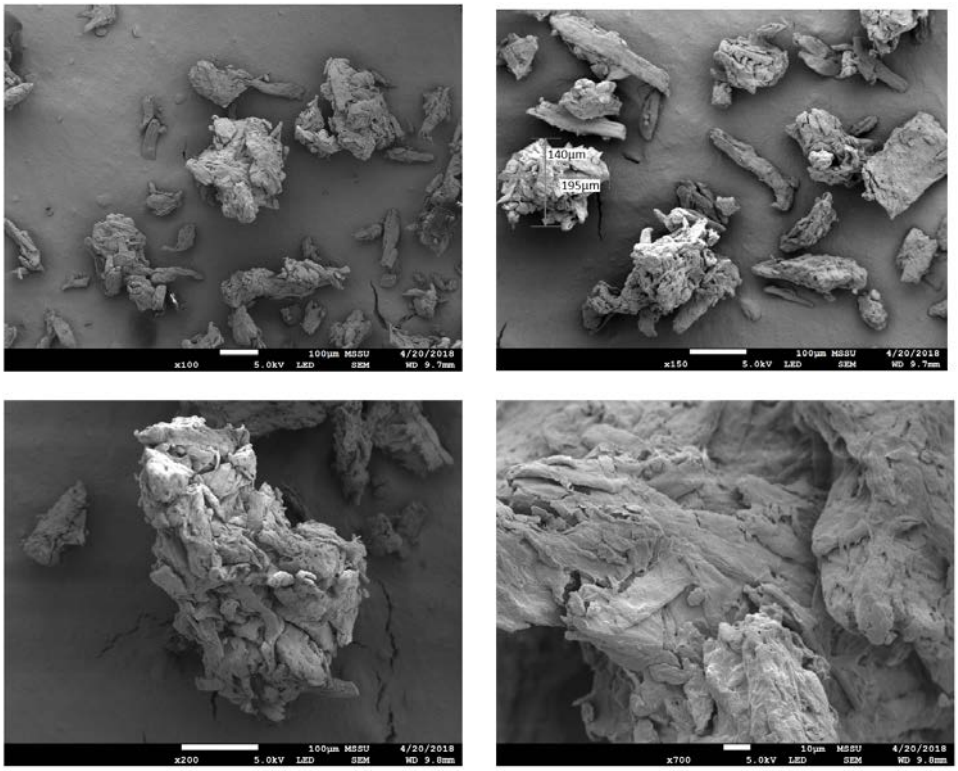

Fig. 4.5. SEM images of batch (a) at different magnification (x100, x150, x200 and x700)

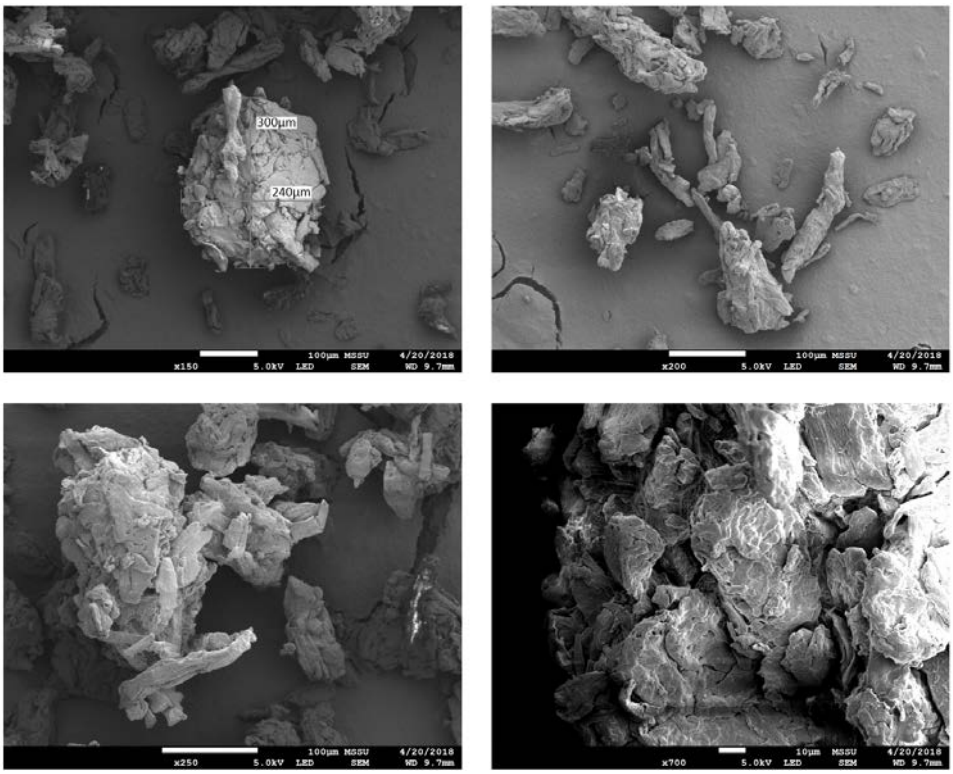

Fig. 4.6. SEM images of batch (c) at different magnification (x100, x150, x200 and x700)

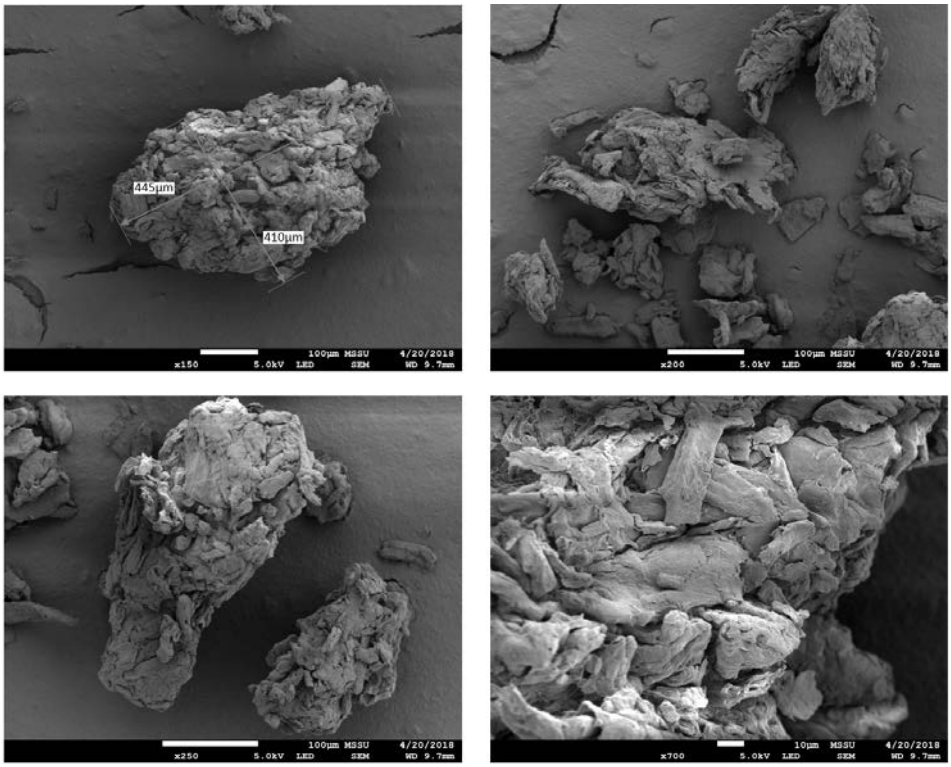

Fig. 4.7. SEM images of batch (e) at different magnification (x100, x150, x200 and x700)

From these SEM images, it is clear that the lower the porosity, the larger the granules produced at the end of the milling operation. From this morphological analysis, as before it seems that the sphericity after dry granulation increases. Therefore, summarising into a unique plot the progress of the sphericity along the particle size (as defined in Chapter 4), the sphericity analysis ends up in Figure 4.8. The speculation on the sphericity risen up looking at SEM images is confirmed by the quantitative result achieved by QicPic. The lower the porosity, the more spherical the granules produced. This effect can be due to the screen aperture, or can be a direct consequence of the powder compressibility during the compaction that led to re–arrangement phenomena. Certainly, the needle shaped particles of the MCC PH–102 helps the packing process, therefore spherical geometries are likely to be achieved through the milling.

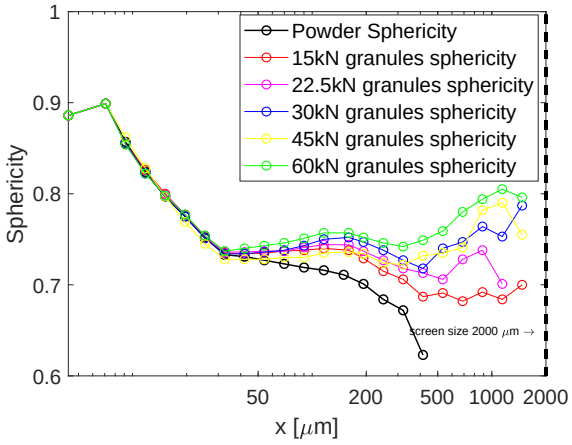

Fig. 4.8. Granules and powder sphericity plotted against particle size

Chapter 5

Milling modelling

Contents

With four parameters I can fit an elephant, with five I can make him wiggle his trunk.

John von Neumann

5.1 Introduction

The population balance model (PBM) approach is widely used to model breakage, crystallization and settling processes in various industries, such as mining, food, chemical, metal and pharmaceutical. Modelling breakage processes with PBMs requires the formulation of a breakage kernel that represents the breakage phenomenon. The strength of the population balance model is its capability to predict the particle size distribution of the milled product as a function of the material properties and the design and operational variables of the mill. It will contribute the understanding of the underlying mechanism that governs the milling in order to obtain a high quality product with the lowest energy cost. Therefore, PBMs can be used not only as a tool for simulation and design, but also to elucidate the breakage mechanism(s) such as massive fracture, cleavage, and/or attrition.

5.1.1 Objectives

The first part of the research was mainly focused on the parameter estimation in order to develop a well-established model, useful for future milling predictions. Firstly, the study was focused on the mass re-distribution of 81 g of MCC PH-102 ribbons into ten size classes, due to the milling process occuring within the Cutting mill system (SM,100,Retsch,Germany). The availability of experimental data allowed to estimate the parameters involved in the model. Thereafter, in order to critically evaluate the results obtained, a sensitivity analysis was carried out. Through this technique, an example of model re–parametrization will also be shown. A first model validation will be presented, changing the milling time. Secondly, after this brief first part that ensured a proper understanding of the model, a more detailed study was developed, using the raw data obtained from the milling of the five different ribbon batches. In this case the aim was to find analytical correlations between the model parameters and the ribbon porosity. In conclusion of the work, model validations were performed and through reliable predictions it was possible to identify the optimum operating condition to minimise the fines produced by the process.

5.2 Development of the model structure

The population balance model is a mass balance accounting for the mass distribution within the size classes, starting from a given initial distribution. In milling process the variation of mass inside each size class is assumed to be just due to the breakage. For perfect mixed batch mills, the mathematical form of the balance solved is [9]:

$$\frac{dM_i}{dt} = -S_i M_i + \sum_{j=1}^{i-1} b_{ij} S_j M_j \tag{5.1}$$

In particular, for a mill equipped with a screen, Eq. 5.1 is re–written as:

$$\frac{dM_i}{dt} = -S_i c_i M_i + \sum_{j=1}^{i-1} b_{ij} S_j M_j c_j \tag{5.2}$$

where the index i represents the number of size classes ($i \geq 1$), whereas j represents the number of size classes before breakage up to i-1. M_i is the mass included within the i class, whereas the elements S_i, c_i and b_{ij} stand for the components of the selection, classification and breakage functions, respectively.
Indeed, the theoretical basis of the model is ruled by the probabilistic view of fragmentation of particles of a given size. It is basically characterized by two functions:

- **Selection function** – $\underline{S}$ is an array including a number of elements equal to i and stays for the specific breakage rate of particles in the class size i. In other words, it represents the fraction of particles that are going to break in the milling operation;
- **Breakage function** – $\underline{\underline{b}}$ is a matrix including the elements b_{ij}, which denotes the distribution of particle sizes obtained after breakage in size class j. That means any given b_{ij} is the mass fraction of material j that transforms into the size class i after the breakage.

In order to build a mechanistic model of the mill, it is assumed that the material passing through the device is relatively free flowing, so that granules smaller than the screen size have an extremely low residence time. This means that once a granule is small enough to pass through the screen, it will leave the mill without any further breakage. To take it in account, a third function has been introduced:

- **Classification function** – $\underline{c}$ is an array including a number of elements equal to i defining whether the particles are small enough to exit the mill.

5.2.1 Selection function S

Selection function or breakage probability indicates the fraction of the particles which were broken during milling process. An empirical model proposed by Austin et al. [4], [13] was used to develop the selection function into the population balance model. The selection function in array form $\underline{S}$ is given as:

$$S_i = k_1 \left(\frac{x_i}{x_{MAX}} \right)^{k_2} \tag{5.3}$$

where k_1 and k_2 represent two model parameters, while $\underline{x}$ is the vector for the size class dimensions.

5.2.2 Breakage function b

$\underline{\underline{b}}$ is a probability function describing the size distribution of the daughter particles. It hence indicates the part of the particles reaching some size interval from a larger size interval as a consequence of breakage. In order to describe the cumulative breakage function $\underline{B}$, based on the P80-m Weibull distribution (Rosin-Rammler distribution, Yu et al. [40]), it was proposed a mass-based cumulative breakage function for bimodal distribution:

$$B(x) = a \left(1 - e^{ln(0.2)\left(\frac{x}{p_1}\right)^{m_1}} \right) + (1-a) \left(1 - e^{ln(0.2)\left(\frac{x}{p_2}\right)^{m_2}} \right) \tag{5.4}$$

where p_1, m_1, p_2, m_2 are model parameters that reflect the bi-modal distribution whereas the parameter a reflects the proportions of the two modes. With the above cumulative breakage function B in continuous form, one can calculate the discrete breakage function $\underline{\underline{b}}$ as:

$$b_{ij} = B(x_j) - B(x_i) \tag{5.5}$$

where x_j and x_i are the upper sizes for interval j and i respectively.

5.2.3 Classification function c

For batch mills fitted with a screen, any particle with a size smaller than the screen size will flow out of the mill. Introducing the so–called classification function (Barrasso et al. [6]), only the size fractions larger than the screen size will be broken down, *i.e.*

$$c_i = \begin{cases} 0 & x_i \leq (1-\sigma)d_s \\ 1 & x_i > d_s \\ \dfrac{d_s - x_i}{\sigma d_s} & (1-\sigma)d_s < x_i < d_s \end{cases} \tag{5.6}$$

where d_s is the screen diameter, while the model parameter σ is the difference between the screen size and the critical size and will be obtained by fitting the experimental data. The classification function implies that if the particle size is smaller than the aperture of the screen, the particles can easily escape from the mill and they will not further be broken.

5.2.4 Numerical approach

Before proceeding with the analysis, it is extremely important to verify that the mass balance is satisfied. During the development of both the breakage and selection functions, according to Bilgili et al. [7], some necessary conditions were fulfilled:

- S_N must be equal to zero;
- $b_{ii} = 0$, meaning that the diagonal terms of the breakage function are null;
- $\sum_{i=j+1}^{N} b_{ij} = 1$, with N equal to the number of size classes.

In order to solve mass balances reported in Eq. 5.2, a MATLAB® code is developed, adopting the solver `ode45` to carry out the calculations. As reported in the introduction, the first aim of the study is the evaluation of the parameters involved within the functions. For this reason, the code embeds also the optimization process through the command `fminsearch`. The objective function to be minimized is defined as follows:

$$\mathbf{S} = min|_{\underline{\theta}} \left\{ \sum_{i=1}^{n^\circ exp} \left(\frac{M_i|^M}{\Delta x_i} - \frac{M_i|^E}{\Delta x_i} \right)^2 \right\} \tag{5.7}$$

In practice, the optimizer looks for a set of parameters included in the array $\underline{\theta}$ capable of minimizing the sum square errors between the normalized mass provided by the model and the normalized mass obtained from the experiment. As discussed in Section §5.1.1, the first part of the chapter will deal with the experimental data already available. They were obtained by sieving analysis, after the milling of traditional ribbon shape for 120 seconds. The upper size class has been estimated to range between 6675 μm and 9440 μm. At the beginning, the 81 g of MCC compacts were located into the upper size class.

5.3 Parameter identification

Knowing the experimental result of the final granule size distribution in terms of mass, it is possible to perform the optimization ending up with a first parameter identification. In the following sequence of plots, the re–distribution of the mass along the milling time is illustrated:

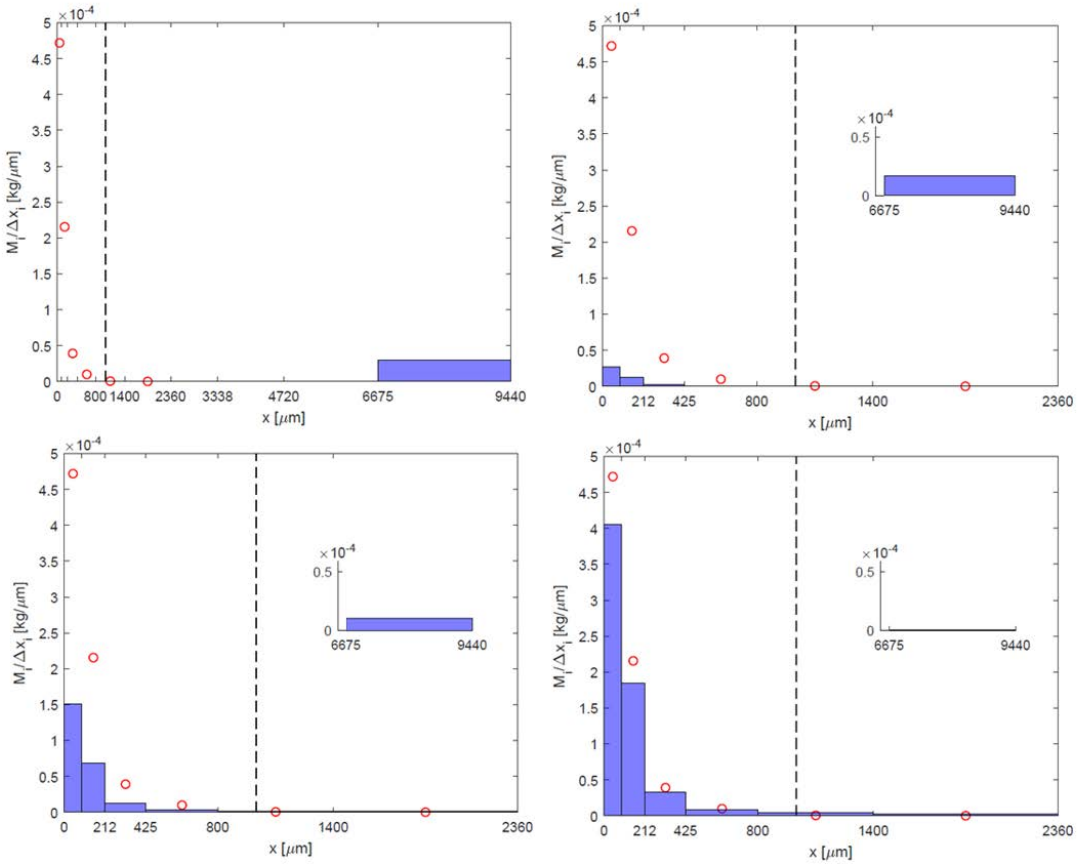

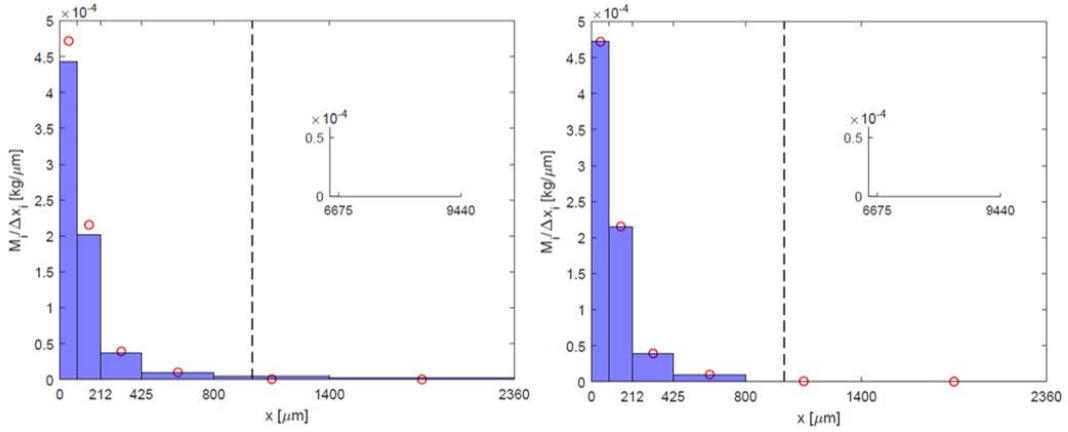

Fig. 5.1. Progress of the mass during the time t = *0-0.05-0.4-2.5-8.8-120 s*

In Figure 5.1, the red dots represent the experimental data, while the dashed black line indicates the screen size equal to 1 mm. The model results are reported in terms of bar plot. First of all, it is clear that the fitting has been able to provide a good set of parameters $\underline{\theta}$, because at t = 120 seconds the model perfectly matches the experimental data. As expected, there are no particles greater than 1000 μm, meaning that the classification function introduced into the model is effectively working. In the following table the set of parameters is reported:

Tab. 5.1. Set of parameters $\underline{\theta}$ obtained

$\mathbf{m}_1$	$\mathbf{m}_2$	$\mathbf{p}_1$	$\mathbf{p}_2$	$\mathbf{a}$	$\mathbf{k}_1$	$\mathbf{k}_2$	σ
1.710	0.252	172	$1.27\text{x}10^4$	0.410	1.260	2.150	0.105

$\underline{\theta}$ includes the parameters values used during the simulation, whose result was reported in Figure 5.1 for the six different screenshots, taken at different time instants. The corrective factor σ introduced in the classification function assumes a reasonable value, since it is roughly equal to 10%. Concerning the five parameters involved in the evaluation of the matrix $\underline{\underline{b}}$, since the final granules size distribution described by the data is monomodal, the second peak must not be present and therefore the value of p_2 should be quite small. However, looking at the Table 5.2, it is possible to notice that p_2 is quite high, even if we should also account for its power coefficient m_2 that is quite small. Unfortunately, these comments are just based on qualitative information, and we have to find out a quantitative strategy capable of characterising the quality of the fitting. The *sensitivity analysis* is that proper tool used to accomplish this goal.

5.4 Sensitivity analysis, 1 mm screen

The sensitivity analysis on the parameters ensures the model identifiability. It is the most important test to perform after any estimation. It is indeed possible to understand whether the parameters can be singularly estimated. The rationale is that changing the model parameters value (usually by 1 percentage point), the model response is expected to change as well. The parameters are then modified one by one to assess the model dependency on each of them. Usually, the first simulation is classified as the nominal one, a kind of base case. So, from the graphics obtained, one can understand the model sensitivity to each parameter and also the experimental conditions which maximize the information obtained.
It is not easy to realize the consequence of an undesired model behaviour, for the following reasons:

- ◇ the model is simply not much sensitive to some parameters (which could be set to zero without affecting the response);
- ◇ some parameters cannot be singularly determined, i.e. *structural unidentifiability*;
- ◇ the experimental conditions required to have enough information for the parameter estimation are not suitable for a physical or an economic point of view, i.e. *practical unidentifiability*.

In our case, $\underline{\theta}$ is the array including the eight parameters values achieved after the previous fitting. Let us re–name that array as $\underline{\theta}_0$, in order to specify that it has been obtained in nominal conditions. The order of the parameters is reported as follows:

$$\underline{\theta}_0 = \begin{bmatrix} m_1 & m_2 & p_1 & p_2 & a & k_1 & k_2 & \sigma \end{bmatrix}$$

Afterthat, using the command `repmat`($\underline{\theta}_0$,1,8), it was possible to create a 8x8 matrix, $\underline{\underline{\theta}}_0$. Then it has been defined the perturbation matrix $\underline{\underline{P}}$ (*8x8*), defined as:

$$\underline{\underline{P}} = \begin{bmatrix} 1.01 & \dots & 1 \\ \dots & 1.01 & \dots \\ 1 & \dots & 1.01 \end{bmatrix}$$

where $\underline{\underline{P}}$ is the perturbation matrix, used to step–increase by 1% the eight parameters, once a time. The resulting perturbated matrix $\underline{\underline{\theta}}_{\varepsilon}$ is simply given by the product:

$$\underline{\underline{\theta}}_{\varepsilon} = \underline{\underline{P}}\,\underline{\underline{\theta}}_{0} = \begin{bmatrix} \theta_{\varepsilon,1} & m_2 & p_1 & p_2 & a & k_1 & k_2 & \sigma \\ m_1 & \theta_{\varepsilon,2} & p_1 & p_2 & a & k_1 & k_2 & \sigma \\ m_1 & m_2 & \theta_{\varepsilon,3} & p_2 & a & k_1 & k_2 & \sigma \\ m_1 & m_2 & p_1 & \theta_{\varepsilon,4} & a & k_1 & k_2 & \sigma \\ m_1 & m_2 & p_1 & p_2 & \theta_{\varepsilon,5} & k_1 & k_2 & \sigma \\ m_1 & m_2 & p_1 & p_2 & a & \theta_{\varepsilon,6} & k_2 & \sigma \\ m_1 & m_2 & p_1 & p_2 & a & k_1 & \theta_{\varepsilon,7} & \sigma \\ m_1 & m_2 & p_1 & p_2 & a & k_1 & k_2 & \theta_{\varepsilon,8} \end{bmatrix}$$

Then, performing the cycle `for w = 1:8`, it is possible to build a 3D–matrix $\underline{\underline{\mathbf{X}}}$, which stores the data necessary for the further analysis (Figure 5.2).

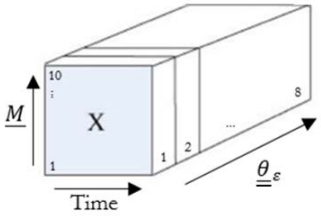

Fig. 5.2. 3D–matrix $\underline{\underline{\mathbf{X}}}$ storing the data required for the sensitivity analysis

Indeed, through a folding procedure, we will create, layer by layer, the matrix of sensitivity $\underline{\underline{\mathbf{Q}}}_S$, collecting after every iteration the progress of the mass moving among the ten size classes as a function of the milling time.

$$\underline{\underline{\mathbf{Q}}}_S = \frac{\left(M_i|_{\underline{\underline{\theta}}_{\varepsilon}} - M_i|_{\underline{\underline{\theta}}_{0}}\right)/\Delta x_i}{\theta^{\varepsilon}_{jj} - \theta^{0}_{jj}} \tag{5.8}$$

Once the matrix is built up, it is possible to assess whether all the parameters involved in the model can be identified from the experimental data. In such a way, we are now going to assess the quality of the experiment itself, understanding whether that experiment can lead us towards identifiable parameters. The result of the sensitivity analysis is reported through a `subplot` visualization in Figure 5.3.
The eight graphs included in the previous plot show the trend of $Q_{S,i}$ along the time for each parameter. This matrix can be seen as the model response with respect to a perturbation in the model parameter set. Of course in order to identify these parameters, the model response must be pretty evident, to allow an easier identification.

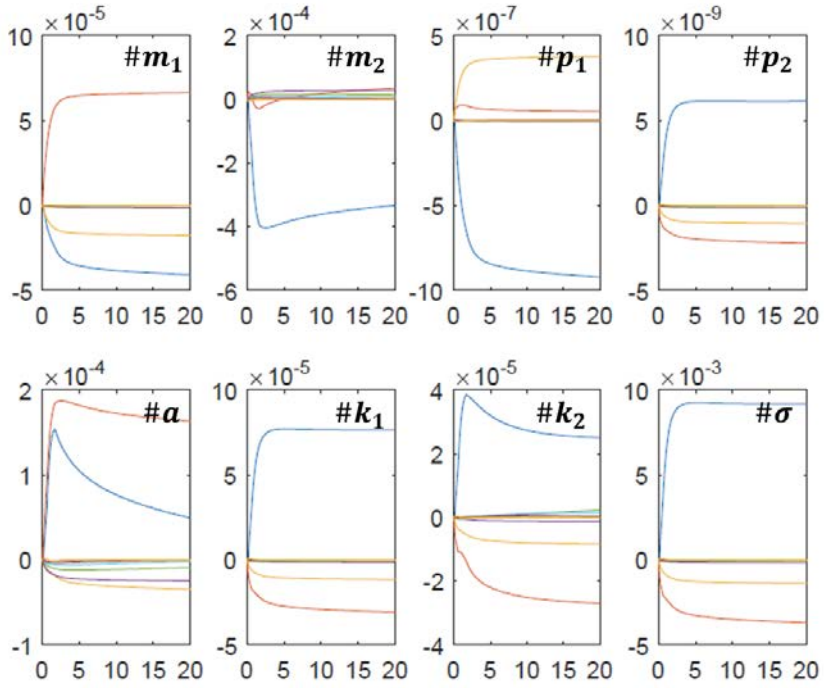

Fig. 5.3. Model response with respect to 1% parameters change one by one. Progress of Q_s for each size class along time [s]

For instance, looking at the subplot $[1,3]$ of Figure 5.3, we will observe what is the progress of $\mathbf{Q}_S$ for each size class along the time after a +1% change of the parameter p_1 compared to its initial value. The evaluation of $\mathbf{Q}_S$, reported in the Eq.(5.8), is done making the subtraction between the normalized mass predicted by the model using the perturbated set of parameters and the normalized mass obtained with the nominal set of parameters; this difference is then divided by the step change in the parameter, which in this case was assumed equal to 0.01. As it can be noticed from Figure 5.3, the third and fourth parameters, p_1 and p_2, look to be extremely difficult to identify through the available data. Indeed the order of magnitude in the y-axis is very low. Therefore, this result is also telling us that a re–parametrization of the model may be helpful. This quantitative result agrees with the early qualitative speculation during the comments on Table 5.2. Therefore, it is an expected conclusion since the final granules size distribution is monomodal and we are trying to fit those data with a bi–modal model for the breakage function, see Eq. (5.4). Moreover, assessing the result of the sensitivity analysis, it is possible to conclude that within the initial 10 seconds of experiment we would have enough information to fit all the other parameters. The same conclusion can be drawn looking at the simulation result in Figure 5.1, since almost the total change in term of mass–redistribution is achieved within 9 seconds.

5.5 Model re–parametrization

Thereafter, an attempt to modify the previous model was performed, trying to account for final shape of granule size distribution. In other words, instead of using Eq. (5.4) to describe the breakage function, it is possible to simplify the model, moving from the initial situation with 8 parameters to a new scenario where the number of parameters within $\underline{\theta}$ is reduced up to 5, considering just a one–mode distribution.
The new shape of the breakage function will be the following:

$$B_i = \left(1 - e^{ln(0.2)\left(\frac{x_i}{p_1}\right)^{m_1}} \right) \tag{5.9}$$

where just the two parameters m_1 and p_1 are involved.
The new array including the parameters used for the optimization is simplified:

$$\underline{\theta}_{new} = \begin{bmatrix} m_1 & p_1 & k_1 & k_2 & \sigma \end{bmatrix}$$

After the optimization procedure, the new set of parameters that better minimizes the objective function **S**, Eq.(5.7), is reported:

Tab. 5.2. Set of parameters $\underline{\theta}_{new}$ obtained

$\mathbf{m}_1$	$\mathbf{p}_1$	$\mathbf{k}_1$	$\mathbf{k}_2$	σ
1.11	180	1.67	1.5	0.133

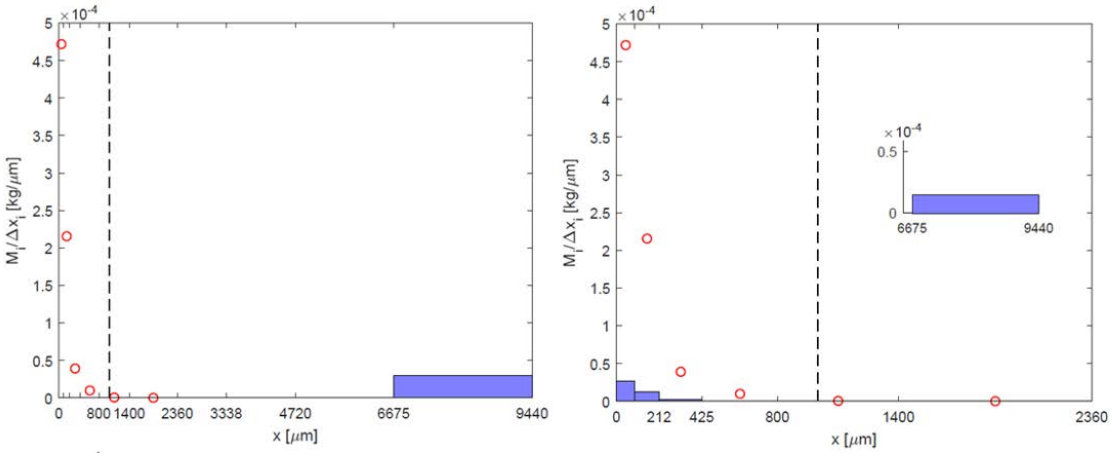

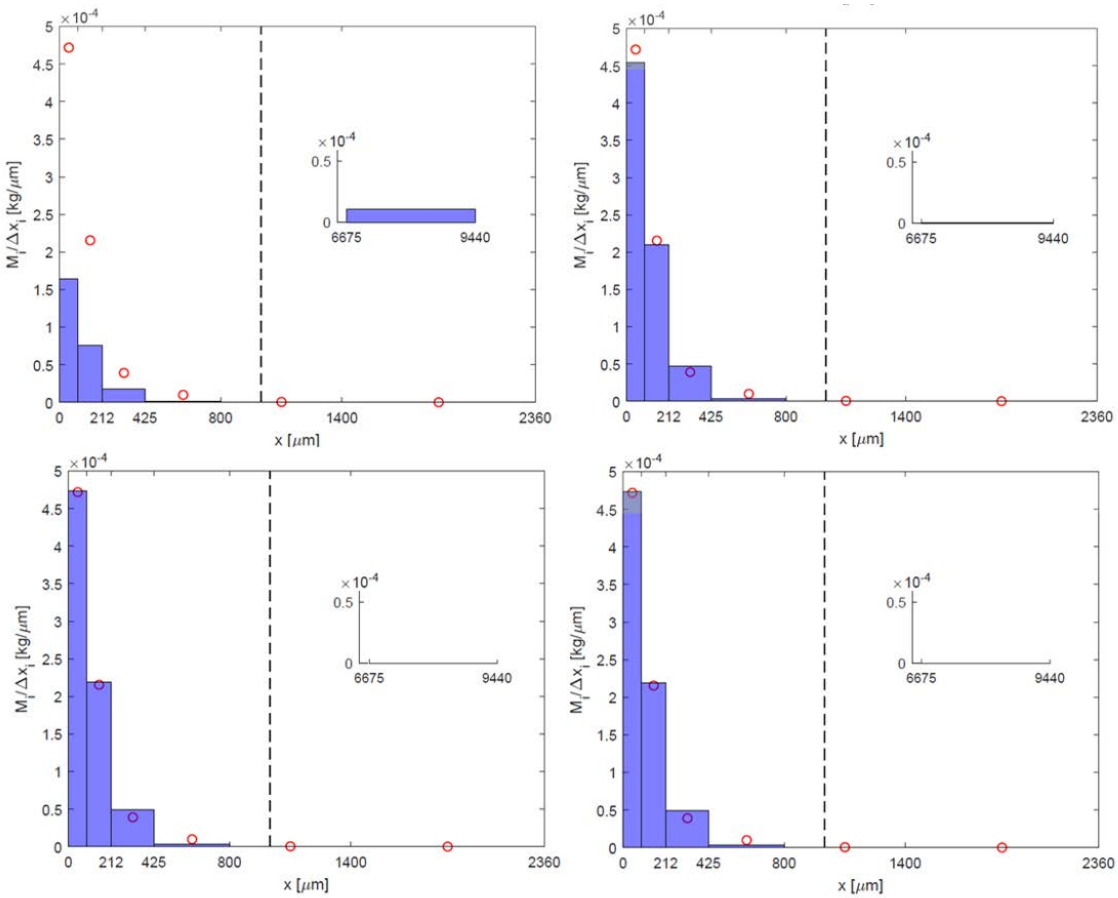

Fig. 5.4. Progress of the mass during the time t = *0-0.03-0.25-2-6.5-120 s*

The result of the minimization procedure is still good, even if the reduction in the parameters number led to a poorer fitting with respect to the initial one. In particular the new model tends to overestimate the mass included within the second and also the third class. Finally, to quantify the parameters identificability, also in this case a sensitivity analysis was performed, hoping to get better results with respect to the previous one. The procedure followed is clearly the same explained before, the only difference is that now we just need to handle five parameters. In Figure 5.5 the results have been plotted. After the model re–parametrization, it is possible to observe that still the parameter p_1 is rather difficult to estimate because of the low order of magnitude (10^{-6}) in the y–axis. Of course, with respect to the previous situation (Figure 5.3), the identificability of p_1 is slightly improved, whereas all the other parameters still remain identificable. Also in this case we recognize that the maximum information can be achieved within the initial 5 seconds, and mostly if we analyze the blue curve and the red curve which stand for the two initial size classes where the highest amount of material will be located.

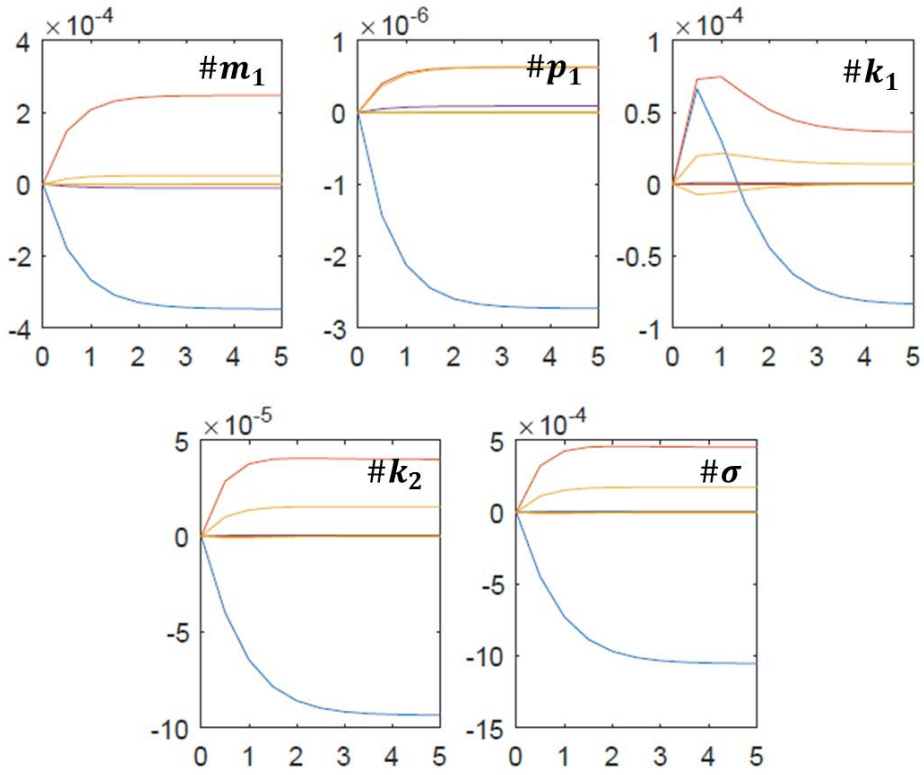

Fig. 5.5. Model response with respect to 1% parameters change one by one

Anyway, aiming to improve the parameter estimation, the origin point $(0,0)$ has been added. In this way, the code can more easily recognize the initial peak.

Tab. 5.3. Set of parameters $\underline{\theta}$ obtained

$\mathbf{m}_1$	$\mathbf{m}_2$	$\mathbf{p}_1$	$\mathbf{p}_2$	$\mathbf{a}$	$\mathbf{k}_1$	$\mathbf{k}_2$	σ
1.110	0.199	180	0.005	1.000	0.950	0.995	0.133

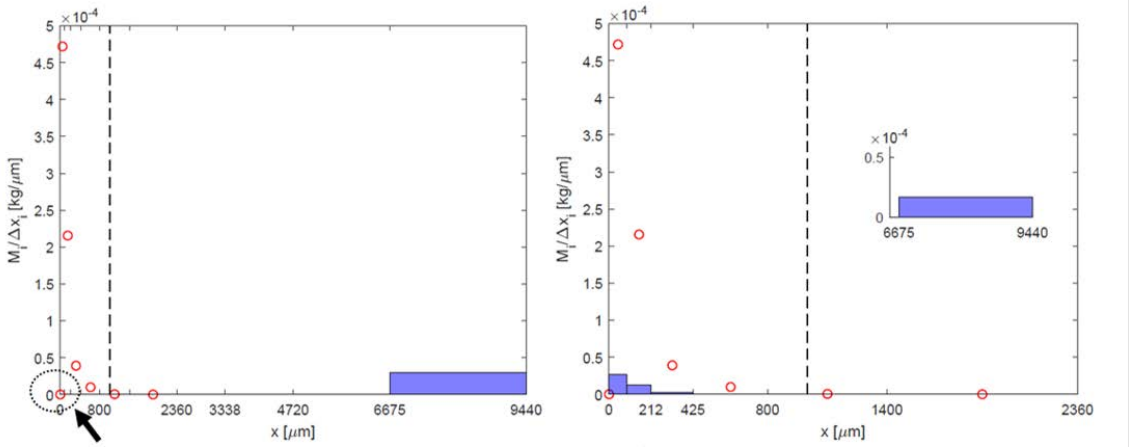

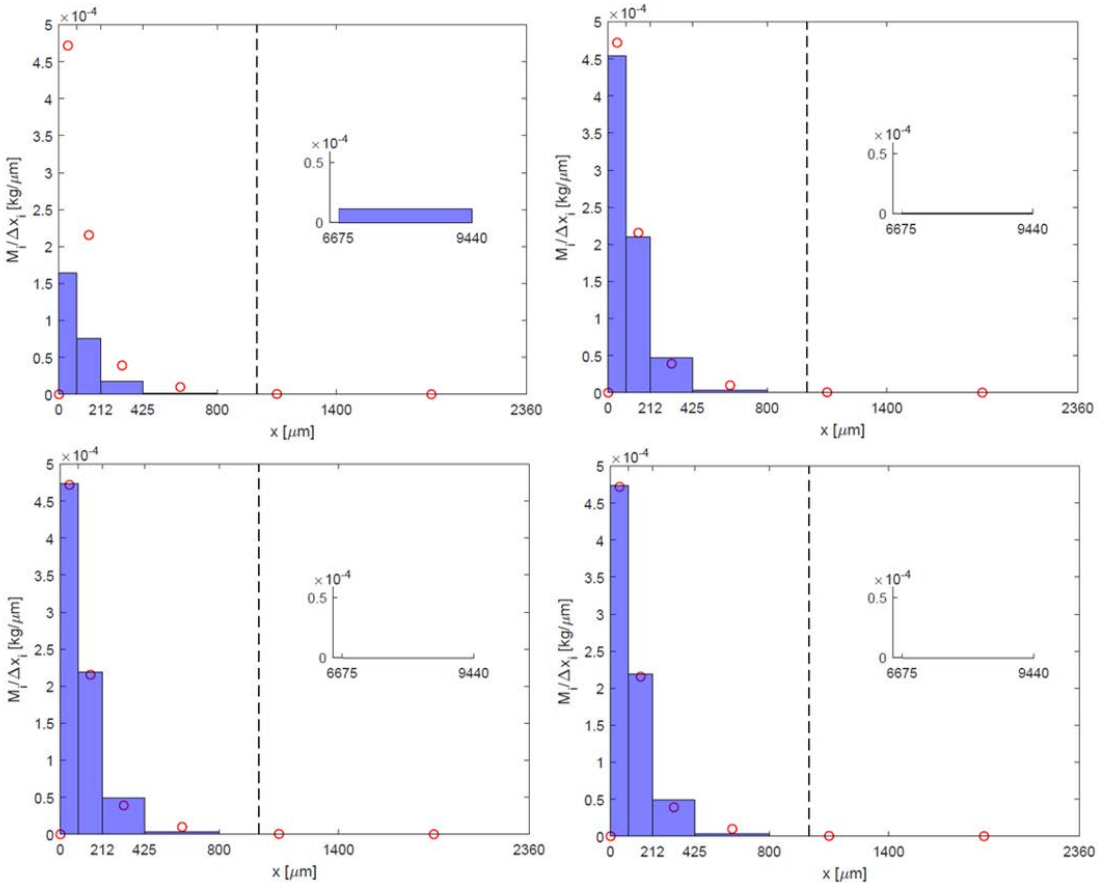

Fig. 5.6. Progress of the mass during the time t = *0-0.06-0.5-3.4-11.35-120 s*

Looking at Table 5.3, it is possible to notice how the new set of parameters is more consistent with the theoretical background. Simpy introducing the origin point, the model is capable to estimate properly its parameter values. In particular, the value of p_2 is roughly zero, as expected since we are dealing with a monomodal distribution case. Also the proportional coefficient a is equal to 1, meaning that there is just one mode in the distribution. Finally the monomodal distribution has been fully characterized; in the end of the analysis, it is recommended to model it adopting the 8 parameters model because it is numerically more stable. However, it is totally suggested to assign as initial guesses for p_2 and a the expected final values (reported in Table 5.3) in order to lead the code towards the more physical solution. In the following Section the bimodal granules size distribution will be modelled.

5.6 Bimodal Granule Size Distribution

In the previous section, it was proved the power of model re–parametrization, whenever issues concerning the parameters identification arise. In this part of the Chapter, the bimodal granule size distribution has been fitted. For sure, in this particular case the definition of the breakage function according to Eq.(5.4) must hold true. Therefore the eight parameters model will be considered, and the values of p_1 and p_2 should correspond to the x $[\mu m]$ location of the two distribution peaks. For this parameter estimation a different set of experimental data was used. Indeed the batch mill had been equipped with the 2 mm screen size. From the experiments it seems that the second peak in the distribution arises owing to the screen choice. The mass entering the mill in this case is 103 g and no losses within the machine are assumed. In Table 5.4 it is possible to find the optimum set of parameters achieved after the fitting procedure. Observing the progress of the mass within the ten size classes along the milling time (reported in Figure 5.7), one can appreciate the quality of the fitting, perfectly capable to capture both the peaks in the mass–based granules size distribution. Moreover, from the simulation it looks that almost the total mass re–distribution occurs within the initial 60 seconds of process, whereas in the following minute of simulation, the last small fraction of mass still included in the top size class moves to the smallest ones.

Tab. 5.4. Set of parameters $\underline{\theta}$ obtained

$\mathbf{m}_1$	$\mathbf{m}_2$	$\mathbf{p}_1$	$\mathbf{p}_2$	$\mathbf{a}$	$\mathbf{k}_1$	$\mathbf{k}_2$	σ
2.67	2.18	110	902	0.389	0.0584	3.52	0.244

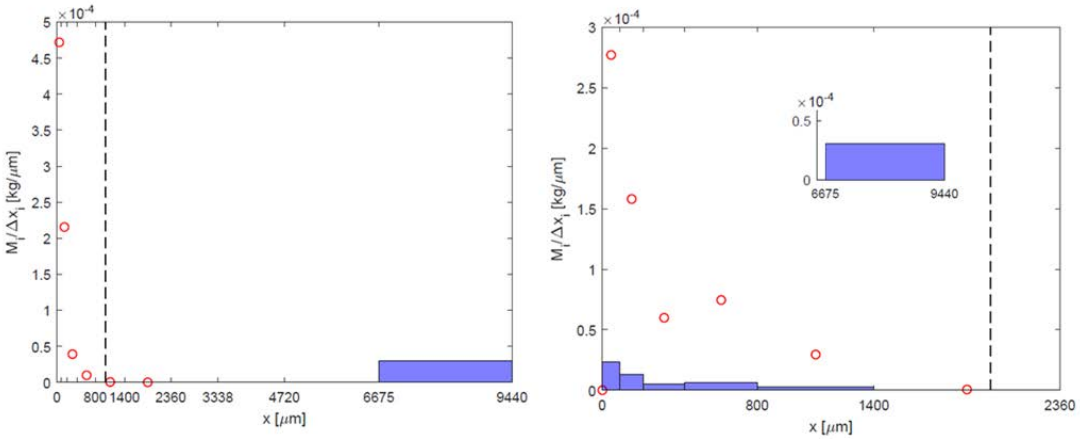

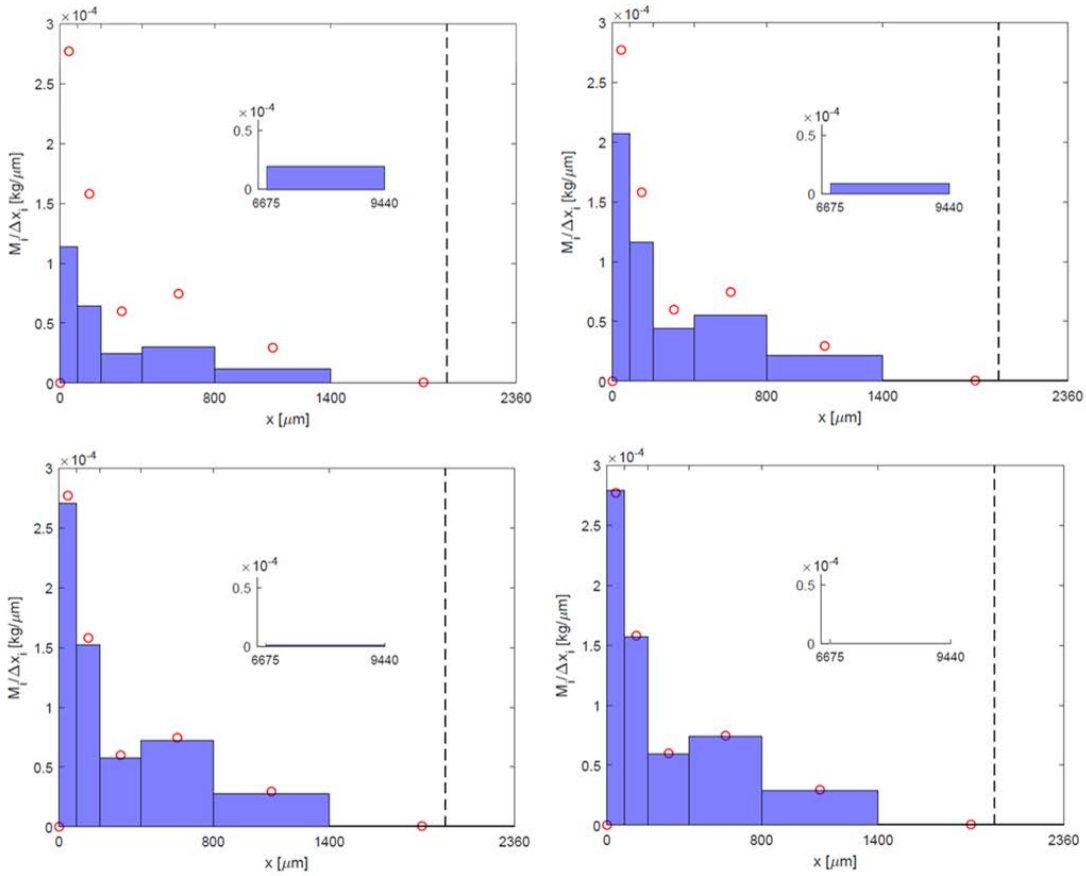

Fig. 5.7. Progress of the mass during the time t = *0-1.5-9-23-59-120 s*

5.6.1 Sensitivity analysis, 2 mm screen

Finally, in order to assess the parameters identificability, once again a sensitivity analysis has been carried out. The results have been plotted in the following Figure 5.8.

As expected, the presence of a second peak in the distribution has increased the complexity in terms of fitting and the first consequence is a more difficult parameter identification through the experimental data, as shown by the model responses. Also in this case the identification of the parameters p_1 and p_2 is very challenging, even if their parameter estimation from fitting makes sense since it is pretty close to the particle size values where the peaks are established. Unfortunately, the analysis shows also that the parameter σ is un–identificable because its $\mathbf{Q}_S$ trend within the ten size classes along the time is flat (y-axis value is in the order of 10^{-16}). One possible conclusion is that this kind of model applied to a bimodal distribution case must be re–parametrized, since in this actual mathematical form the parameter σ cannot be identified from the experiments.

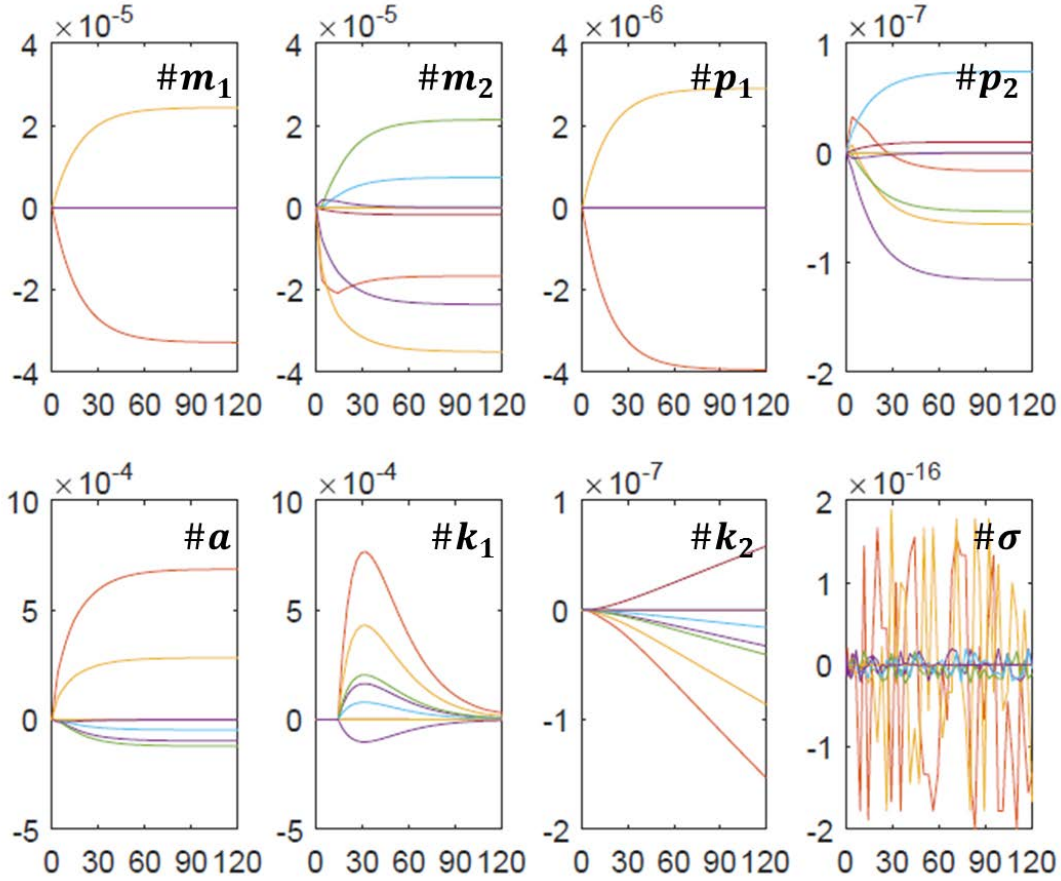

Fig. 5.8. Model response with respect to 1% parameters change one by one

On the other hand, the un–identificability of σ for the case involving the larger screen (2 mm) theoretically makes sense, since eventually the corrective factor is effectively important just for smaller screen (like the 1 mm).
To conclude this first analysis, two x–log scale plots are now reported, where it is possible to better appreciate the particle size distributions for both the screen sizes analyzed. As before, the red dots represent the experimental points, whereas the black curve embeds the model result. The mill equipped with 1 mm screen size will lead to a monomodal distribution, whereas the case with 2 mm screen ends up with a bimodal distribution.

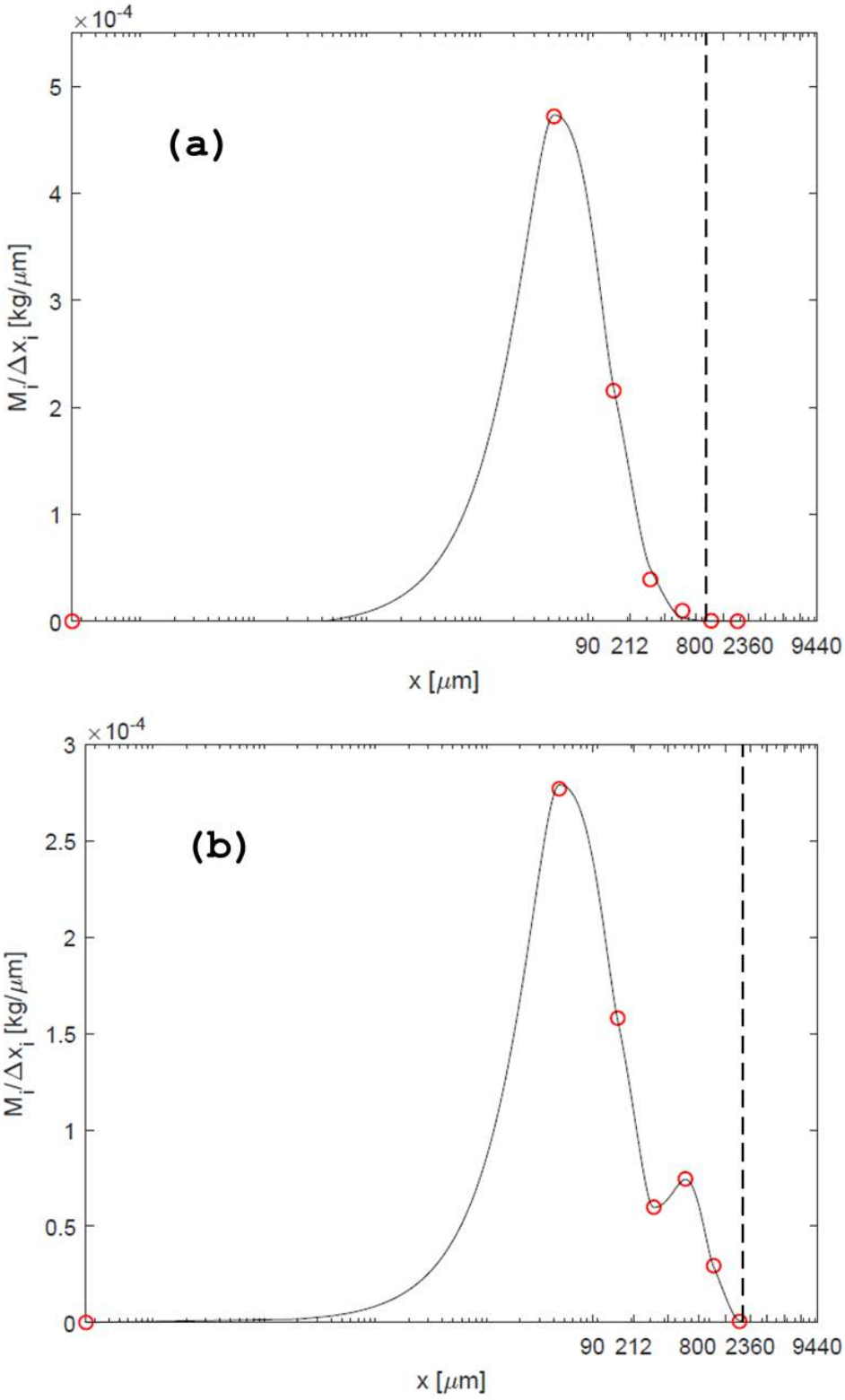

Fig. 5.9. (a) shows the 1 mm screen distribution, while (b) the 2 mm screen one

5.7 Consistency evaluation of the model

Up to this point, the goodness of fitting and the identificability of parameters have been proved. Now there is the need to evaluate also the consistency of the parameter estimation. In order to do this, different set of experimental data were used. Indeed, the previous modelling was developed for granules obtained by the milling of ribbons with a controlled porosity of 30 %. In this part of the study, experimental data referred to the milling of tougher ribbons, with a porosity of 24 %, will be exploited. The hardness of the ribbons will be higher and therefore it is expected an increase of the second mode of the distribution, meaning that more granules will be produced. The main aim is to assess whether the optimum set of parameters obtained from the fitting change compared to the previous results.
Even in this case, both the 1 mm and the 2 mm screen cases have been analyzed.

5.7.1 Monomodal Granule Size Distribution – 1 mm screen size

In Table 5.5, the result of the fitting in terms of parameter array is reported:

Tab. 5.5. Set of parameters $\underline{\theta}$ obtained

$\mathbf{m}_1$	$\mathbf{m}_2$	$\mathbf{p}_1$	$\mathbf{p}_2$	$\mathbf{a}$	$\mathbf{k}_1$	$\mathbf{k}_2$	σ
1.007	0.225	325.737	0.000	1.000	0.034	0.836	0.114

In agreement with the results reported in Table 5.3, also in this case, since it is a monomodal distribution, the value of p_2 is almost zero, whereas a is around 1. Figure 5.10 shows the simulation results and one can notice the progress of the mass into the several size classes along the milling time:

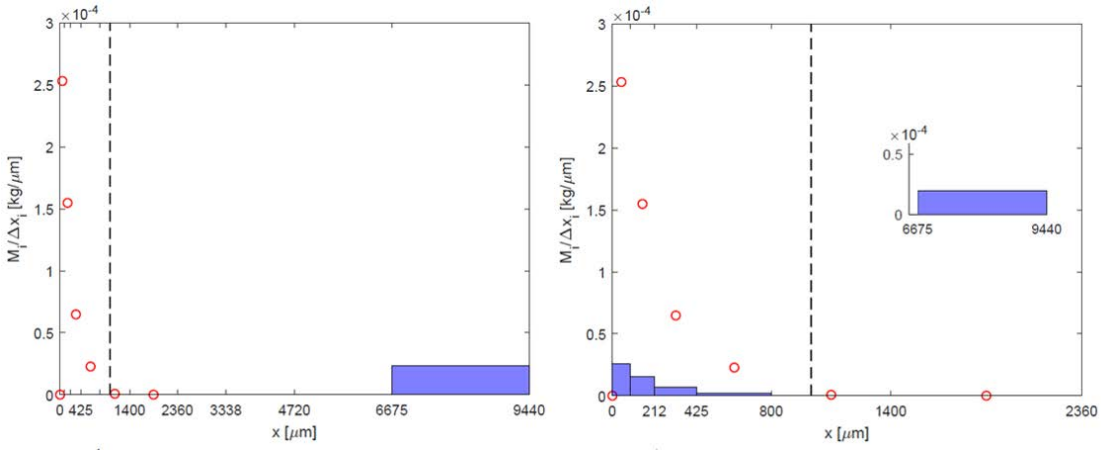

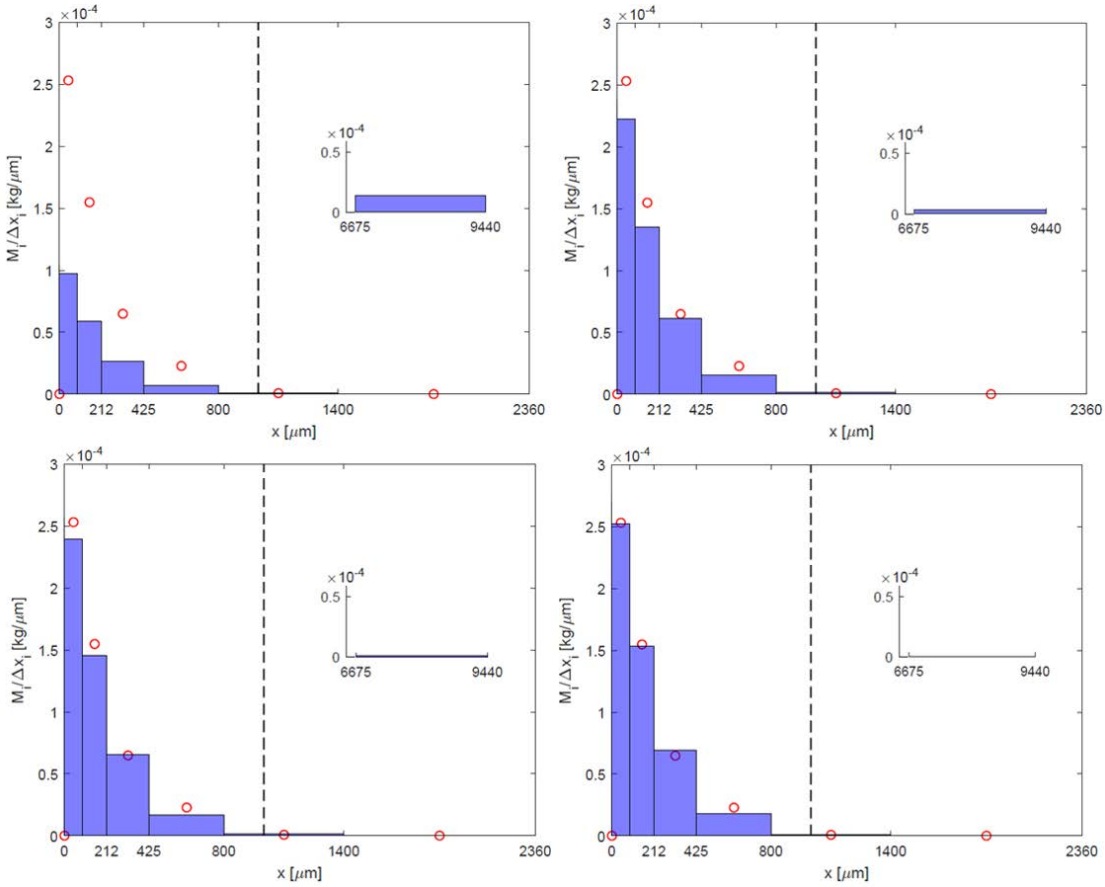

Fig. 5.10. Progress of the mass during the time t = *0-3-14-59-80-120 s*

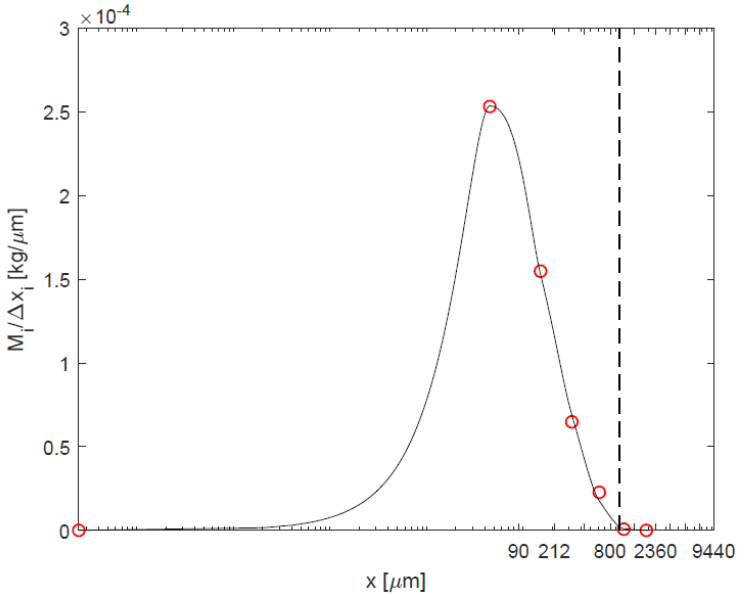

Fig. 5.11. Granule size distribution in log scale for 1 mm screen size

In order to provide a general validity to the model, it is still suggested to adopt all the eight parameters involved in the original model because of numerical stability. In view of the above, concerning the monomodal distributions it is possible to conclude that assigning $p_2 = 0$ and $a = 1$ are reasonable guesses, since their final values from the fitting reflect the theoretical speculation. Concerning the goodness of the fitting, both Figure 5.10 and Figure 5.11 show that there is a pretty small mismatch in the tail of the distribution (third and fourth size class). Anyway, despite this tiny error, the quality of the fitting is still good.

5.7.2 Bimodal Granule Size Distribution – 2 mm screen size

Milling ribbons with lower porosity (24 %), one can foresee that the percentage of granules produced will be higher compared to the initial case for which the porosity was 30 %. Figure 5.12 points out the re–distribution of the mass into the several size classes along the milling time, highlighting just the initial six ones:

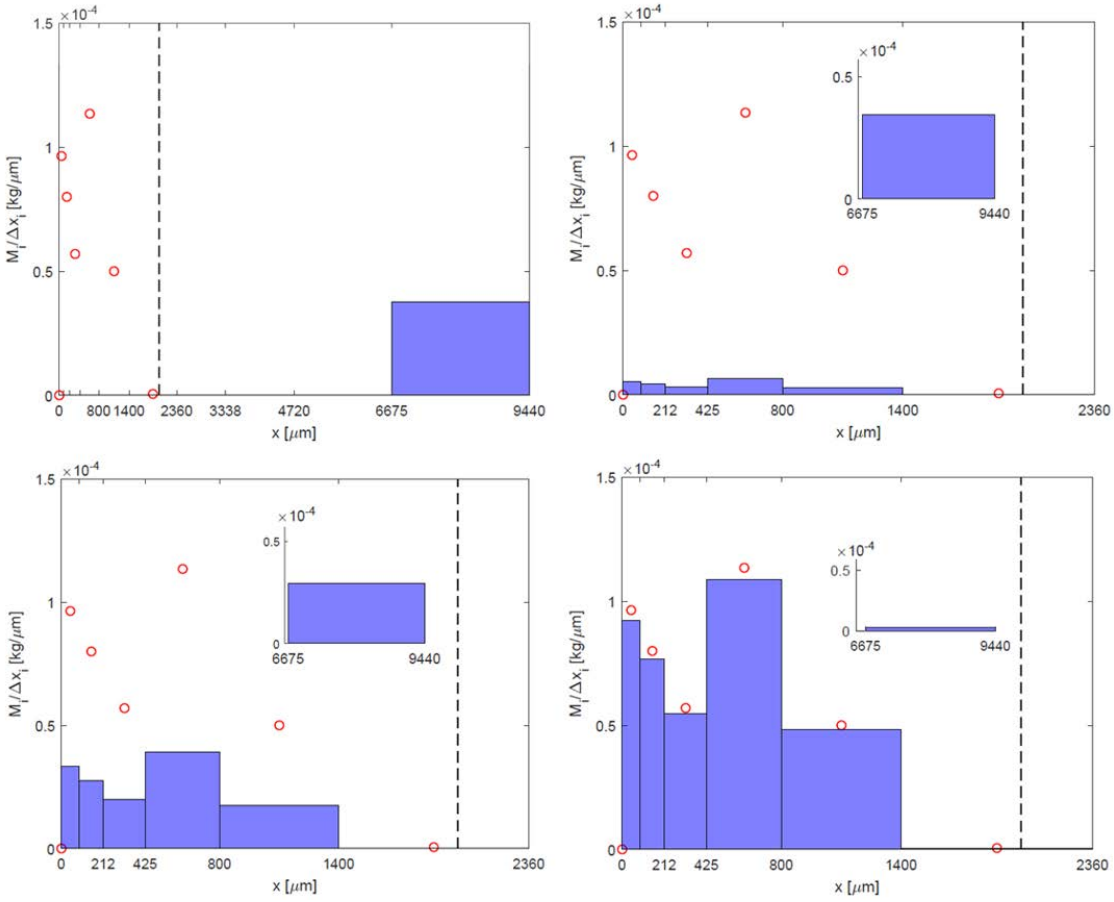

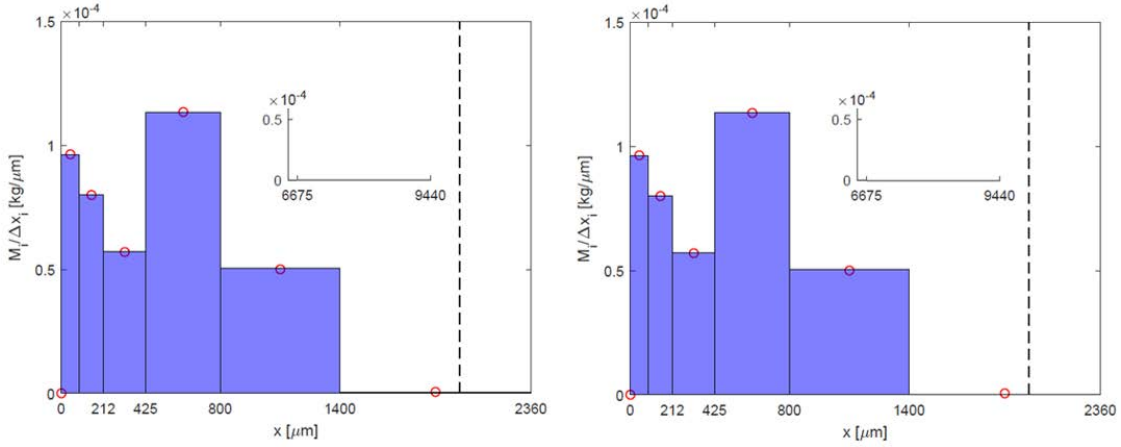

Fig. 5.12. Progress of the mass during the time t = *0-0.03-0.2-1.6-5.2-120 s*

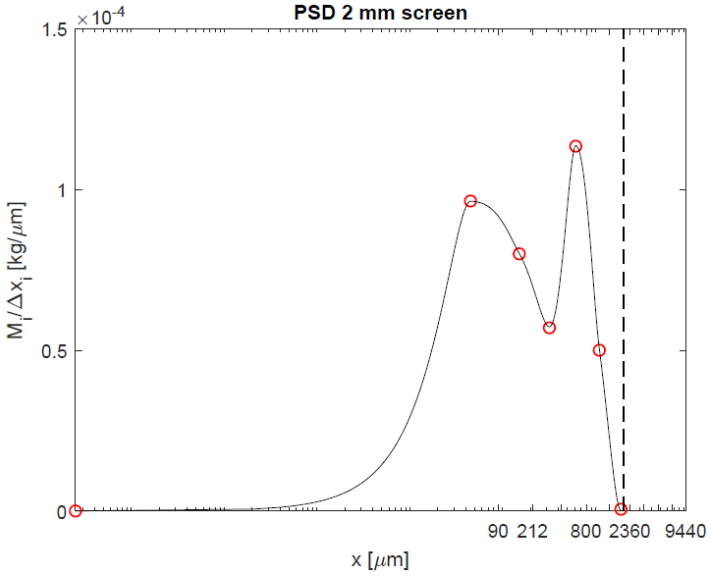

Fig. 5.13. Granule size distribution in log scale for 2 mm screen size

Looking at Figure 5.12, it is pretty evident how the second mode overcomes the first one. In Table 5.6, the optimum set of parameters is reported:

Tab. 5.6. Set of parameters $\underline{\theta}$ obtained

$\mathbf{m}_1$	$\mathbf{m}_2$	$\mathbf{p}_1$	$\mathbf{p}_2$	$\mathbf{a}$	$\mathbf{k}_1$	$\mathbf{k}_2$	σ
1.680	2.930	154	931	0.171	2.01	2.54	0.161

Once againg from Figure 5.12 and Figure 5.13, it is possible to appreciate the goodness of the fitting. The values of p_1 and p_2 do not change significantly from the previous set of parameters achieved for the different porosity. That is reasonable, since the peak locations are almost the same, despite the different porosities. To

better highligth the comparison in terms of parameter estimation, in the following section there will be Table 5.11 and Table 5.8 which summarize the key results obtained in this study, for both the porosities investigated and for each screen size. In conclusion of the first part, a summary of the main findings is now reported:

Tab. 5.7. Final set of parameters $\underline{\theta}$ for the two porosities, 1 mm screen

	$\mathbf{m}_1$	$\mathbf{m}_2$	$\mathbf{p}_1$	$\mathbf{p}_2$	$\mathbf{a}$	$\mathbf{k}_1$	$\mathbf{k}_2$	σ
ε=30%	1.110	0.199	180	0.005	1.000	0.950	0.995	0.133
ε=24%	1.007	0.225	325.737	0.000	1.000	0.034	0.836	0.114

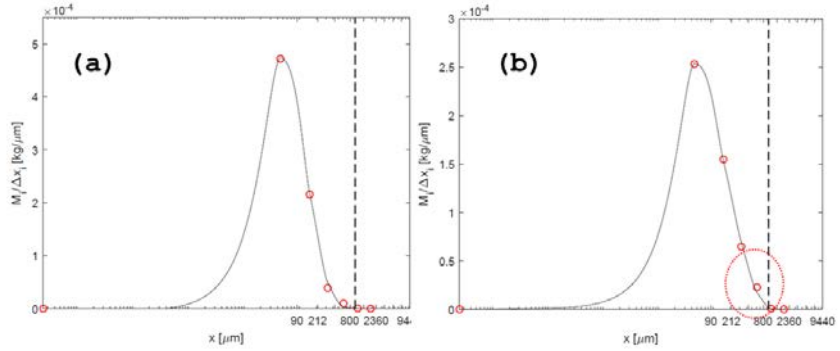

Fig. 5.14. (a) $\Rightarrow$ (1 $mm, \varepsilon = 30\%$), while (b) $\Rightarrow$ (1 $mm, \varepsilon = 24\%$)

Tab. 5.8. Final set of parameters $\underline{\theta}$ for the two porosities, 2 mm screen

	$\mathbf{m}_1$	$\mathbf{m}_2$	$\mathbf{p}_1$	$\mathbf{p}_2$	$\mathbf{a}$	$\mathbf{k}_1$	$\mathbf{k}_2$	σ
ε =30 %	2.67	2.18	110	902	0.389	0.0584	3.52	0.244
ε =24 %	1.680	2.930	154	931	0.171	2.01	2.54	0.161

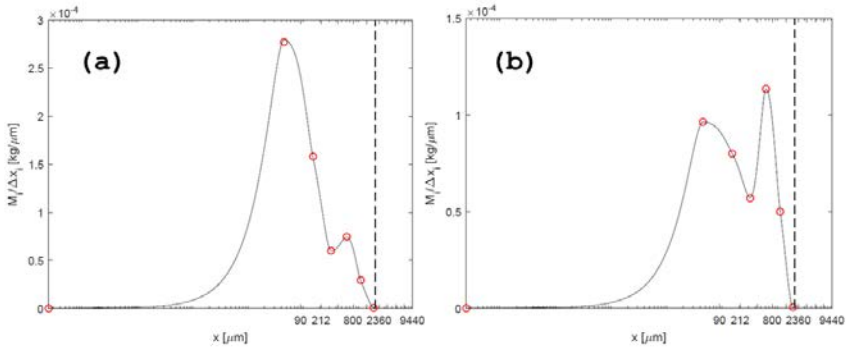

Fig. 5.15. (a) $\Rightarrow$ (2 $mm, \varepsilon = 30\%$), while (b) $\Rightarrow$ (2 $mm, \varepsilon = 24\%$)

Concerning the 1 mm screen size, even if the ribbon porosity changed, in the end the final granules size distribution still remains monomodal. And indeed the value of p_2 and a are consistent with this fact. There's just one mode, implying that a is equal to 1, while p_2 stays roughly equal to zero. Unfortunately, the value of p_1 changes between the two cases. This is unexpected, since the peak location remains the same. Probably the larger amount of granules produced starting with ribbon at lower porosity (see detail in Figure 5.14,**(b)**) leads the optimization to increase the value of p_1. The other parameters involved in the breakage function are pretty comparable, as well as the corrective parameter within the classification function. Concerning the selection function, k_2 remains roughly constant, but k_1 is nearly one order of magnitude lower for the second porosity. With regard to the 2 mm screen size, the situation looks to be much more interesting. First of all, also in this case the peak locations remain constant between the two porosities and indeed the model parameters p_1 and p_2 don't change. That's totally coherent with the theory. Moreover, looking at Figure 5.15, it is evident how the proportionality between the two modes of the distribution changes moving from the initial situation at higher porosity to the second one. In view of the above, one would expect that the proportional parameter a changed, and indeed that's what happened. Also in this case the parameter k_1 changes with the porosity, while σ is still included within a reasonable range. Finally, concerning the parameters m_1 and m_2, there is a sort of effect compensation, meaning that m_1 decreases from the initial condition to the second one, whereas m_2 increases.

5.8 Validation of the model

As final analysis concerning the traditional ribbons, the model validation was carried out. Therefore, using the parameters in Table 5.11 and Table 5.8, first we have decided to simulate a milling process of 50 seconds, feeding the mill with the ribbons at lower porosity (ε=24%) and adopting the 1 mm screen size. The model results were then compared with the new experimental data produced just to assess the quality of the predictions. Figure 5.16 shows the predicted granules size distribution, directly compared with the experiments. The model slightly overestimates the distribution peak, but the quality of the prediction is still good. One might also notice that 50 seconds of milling operation is not enough to break down completely the feed ribbons, since there is still some material located in the upper size class.

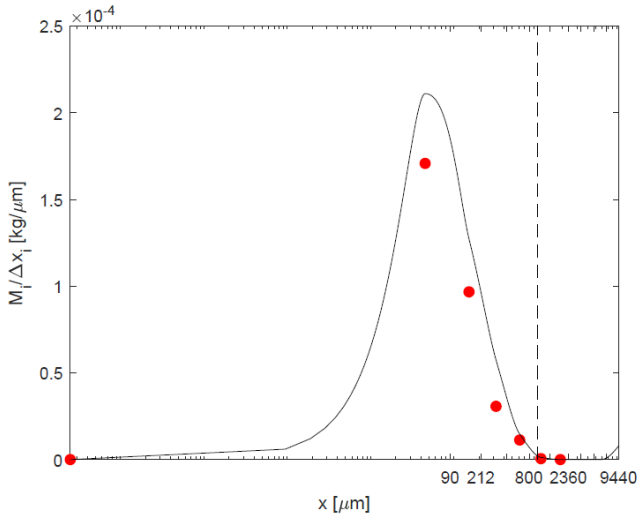

Fig. 5.16. Measured (red points) and predicted (solid line) milled granule size distribution equipping the mill with the 1 mm screen size (ε=24%)

As further validation, the Retsch® mill has been equipped with the 2 mm screen size and we simulated the process feeding the mill with the ribbons at higher porosity (ε=30%).

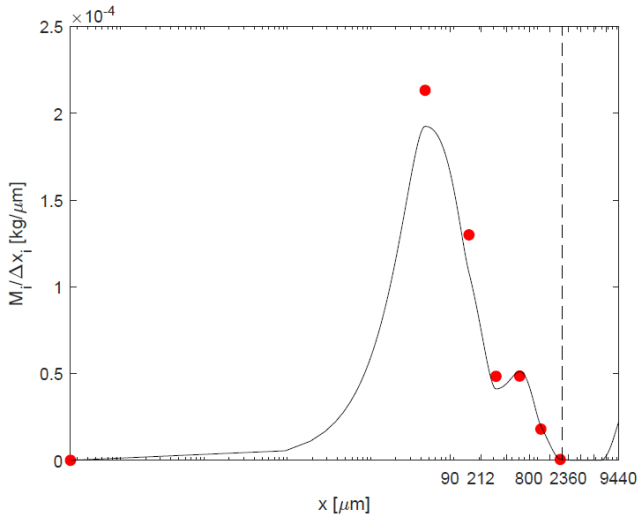

Fig. 5.17. Measured (red points) and predicted (solid line) milled granule size distribution equipping the mill with the 2 mm screen size (ε=30%)

In this case, a milling time of 20 seconds has been chosen. One might expect that the process is not fulfilled, and indeed this speculation is confirmed by the model result. Once again, a new set of experimental data has been performed and Figure 5.17 shows both the measured granule size distribution and the model result. The prediction looks quite good, the first peak is slightly underestimated but the

error is quite low and the final shape of the distribution is close to the measured points. Both these simulations proved the goodness of the previous parameter estimation, but unfortunately there is still not a way to correlate the parameter values to the input milling conditions, such as the screen size choice or the feed ribbon porosity. For this reason, further analysis are required in order to make the model more predictive.

5.9 Milling of circular ribbons

In the second part of the Chapter, the application of the population balance model to the circular ribbons is discussed. Granules were purely made of one excipient, the MCC PH–102 Avicel®. In order to enlarge the experimental field, five batches of ribbons with different porosities were performed using the Instron® mechanical press under controlled process conditions. These batches were produced charging the die with a constant amount of material equal to 1000 ± 4 mg but changing the maximum compression load. The ribbons porosity ε ranges between 47 % (a) and 23 % (e). Then, the ribbons were size reduced in a cutting mill (Retsh® batch mill) with a fixed impeller speed of 1500 rpm. The screen used in the experiments had squared apertures of 2 mm. The milled granules were then sampled for characterisation. In particular the granule size distribution was computed using a QicPic (Sympatec®) with a Gradis/L gravity disperser and a Vibri/L dosing unit. This instrument performs a dynamic image analysis for free-flowing powders and granules from 5 μm to 10,000 μm with dispersion in free fall. In order to assess the upper size class within which the mass of the feeding ribbon has to be classified, the following procedure was adopted.

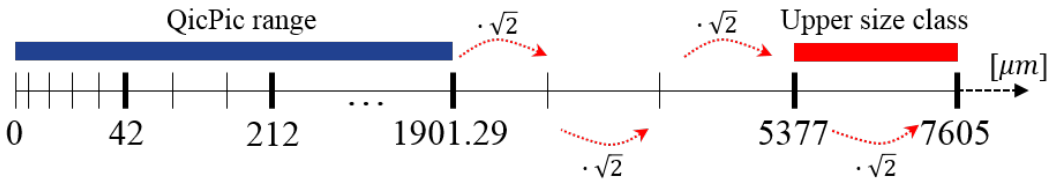

Fig. 5.18. Upper size class determination procedure

The upper size class was estimated based on geometrical hypothesis. The volume of the single ribbon has been assessed, assuming an average thickness among all the batches. Thereafter, the radius of the sphere having the same volume of the cylindrical ribbon was assessed and it has been assumed to be a reference value of the maximum size class. Therefore, starting from the maximum particle size

produced as experimental output by the QicPic, the $\sqrt{2}$ rule was adopted. Other size classes were added, until the reference value previously assessed was reached (Figure 5.18). Recalling Tab. §3.1, Table 5.9 summarises the batches porosities:

Tab. 5.9. Porosity variability within each ribbon batch

	(a)	(b)	(c)	(d)	(e)
$\varepsilon = [\%]$	46.7±2.3	39.4±2.3	34.3±3.2	27.3±3.3	23.8±4.5

Figure 5.19 shows the whole experimental set up followed along the work, starting from the ribbon production through die compaction and ending up with the QicPic measurement of the granule size distribution.

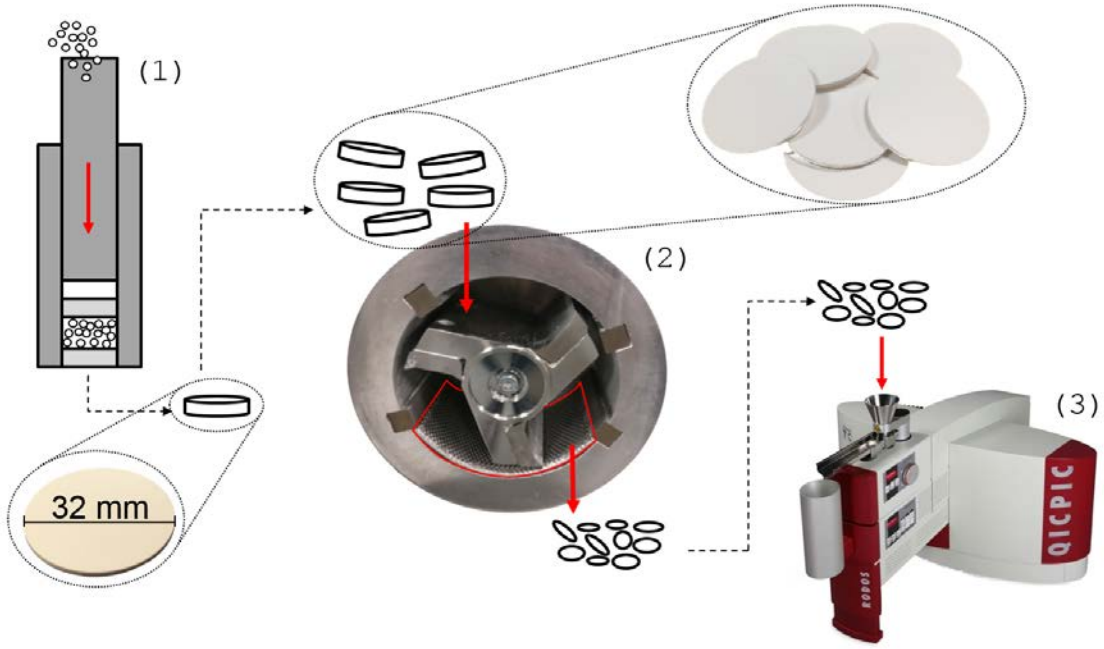

Fig. 5.19. (1) Instron press for die compaction, (2) Retsch mill for milling, (3) QicPic for granule size distribution

5.9.1 Model refinement

Minimising the objective function **S** presented in Eq. 5.7, the parameter identification was performed. Afterthat, the first purpose of the study is to quantify the effect of the ribbon porosity on the final parameter estimation. Indeed Figure 5.20 illustrates the progress of the parameters along the five ribbon batches at different porosities.

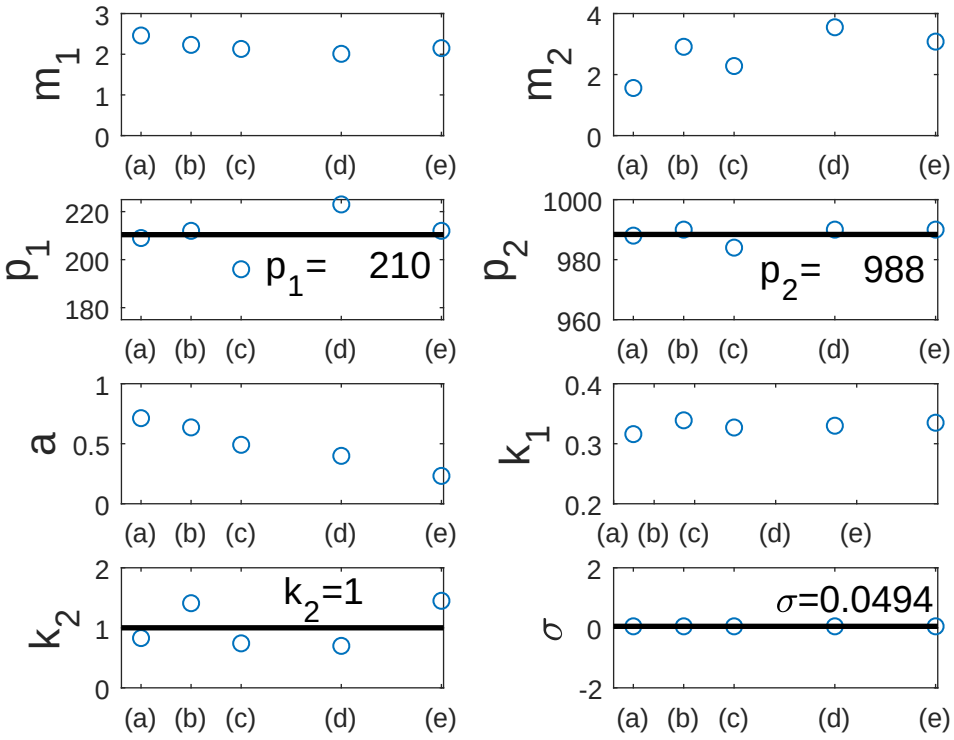

Fig. 5.20. Parameter estimation as a function of different circular ribbon porosities

From Figure 5.20 one can observe that σ is totally independent of the porosity. This result makes sense since we are dealing with an highly intensive mill (1500 rpm). Indeed, despite of the porosity value, the mill blades break the tablets so fast that it is not necessary to account for any critical size difference in the classification function since everything is just dragged down when the particle size is lower than the screen size diameter. Furthermore, coherently with the theory, p_1 and p_2 look to be quite constant because the peak positions do not change with the porosity. This lead us to conclude that p_1 and p_2 can be assigned as material constants and they are just screen size–dependent since the granule size distribution would turn to be monomodal if the mill was equipped with the 1 mm screen.
Figure 5.21 is a surface plot where the progress of the granule size distribution as a function of the porosity can be appreciated; the two planes have been located corresponding to the particle sizes equal to p_1 and p_2 respectively.

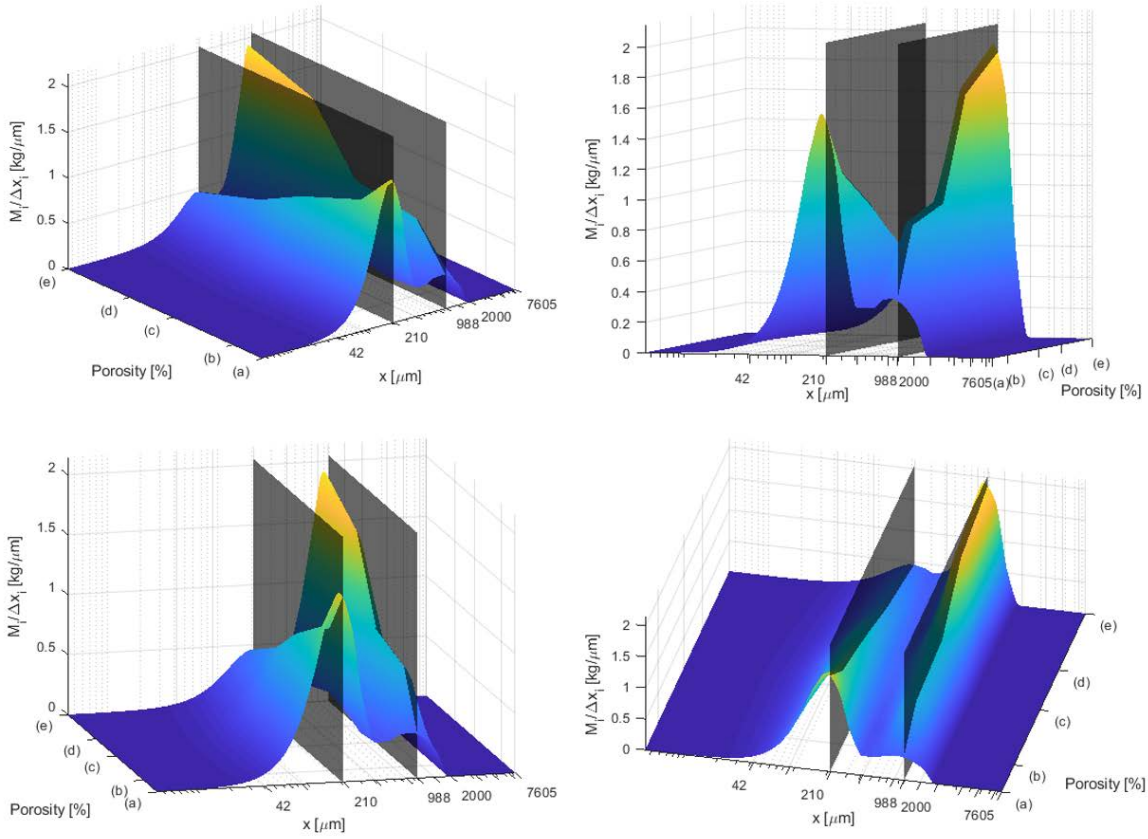

Fig. 5.21. 3D surface plot of the granule size distributions as a function of porosity

From Figure 5.21 one can easily observe how the proportion between the two modes changes depending on the porosity value. Hence for the higher porosity case (a), most of the mass is located within the first peak, meaning that the largest amount of material has turned back to the previous powder condition (low amount of granules). The situation is totally the opposite looking at the lower porosity value (e), where just the second peak exists. In terms of modelling, the constancy of p_1 and p_2 which have been found to be just material–dependent simplifies the model, since we are moving from an initial system with eight parameters to a new one where reasonably the number of parameters has been reduced up to five (σ will be assumed constant). As further step, another model semplification was adopted. Looking at Figure 5.20 the parameter k_2 is sustained roughly around 1 for the five tablet batches. From the theory, k_2 is that parameter related to the granule shape. Therefore it was decided to re–arrange the model, setting k_2=1 as material constant. In this way, the selection function $\underline{S}$ turns to be linear and involves just the parameter k_1 (Eq. 5.3). Furthermore, the geometrical exponents m_1 and m_2 involved in Eq. 5.4 can reasonably be simplified into integer values. Figure 5.20 highlights that m_2

should be slightly higher than m_1, even if its variability is larger. Therefore, a combinatorial analysis has been performed, aiming to explore multiple combinations for m_1 and m_2 integer values. In particular, the ranges investigated were bounded between 2 and 3. Up to this point, the model was re–formulated into the following parameter's structure:

Tab. 5.10. Model formulation before combinatorial analysis

$\mathbf{m}_1$	$\mathbf{m}_2$	$\mathbf{p}_1$	$\mathbf{p}_2$	$\mathbf{a}$	$\mathbf{k}_1$	$\mathbf{k}_2$	σ
`[for 2:0.5:3]`	`[for 2:0.5:3]`	210	988	$\mathbf{Par}_1$	$\mathbf{Par}_2$	1	0.0494

In this way, the parameters left in the model available for fitting are a and k_1:

$$\underline{\theta} = \begin{bmatrix} a & k_1 \end{bmatrix}$$

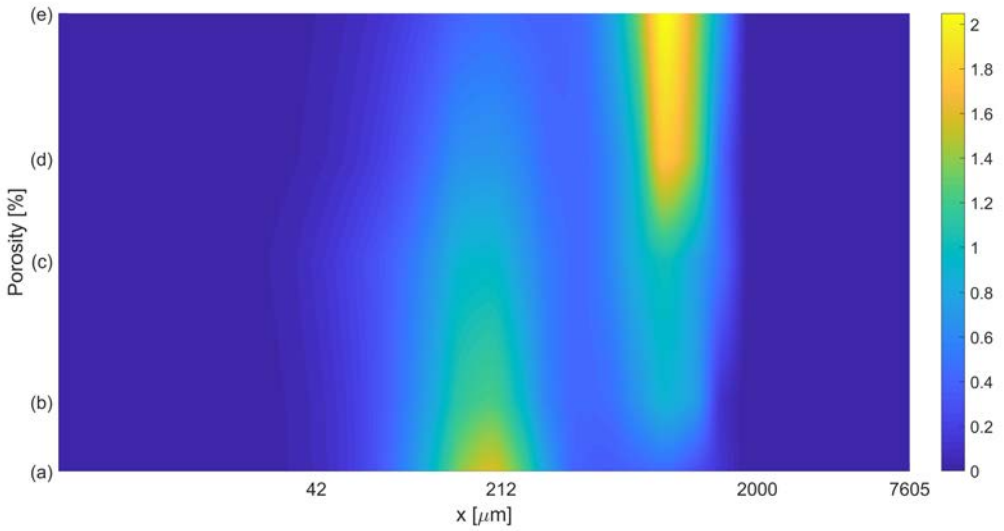

Fig. 5.22. XY view of 3D surface plot of the granules size distributions as a function of porosity according to the experimental data

Figure 5.22 reports the XY view of the milled granule size distributions according to the QicPic results. Coherently, the first mode dominates when the porosity is high, whereas the second one increases step by step decreasing the porosity. This figure is then compared with the model results (illustrated in Figure 5.23), trying to identify the most suitable combination of m_1 and m_2 capable to properly match these experimental data. From the combinatorial analysis, the best parameter pairing that allows to approach the experimental data is m_1=2 and m_2=2.5.

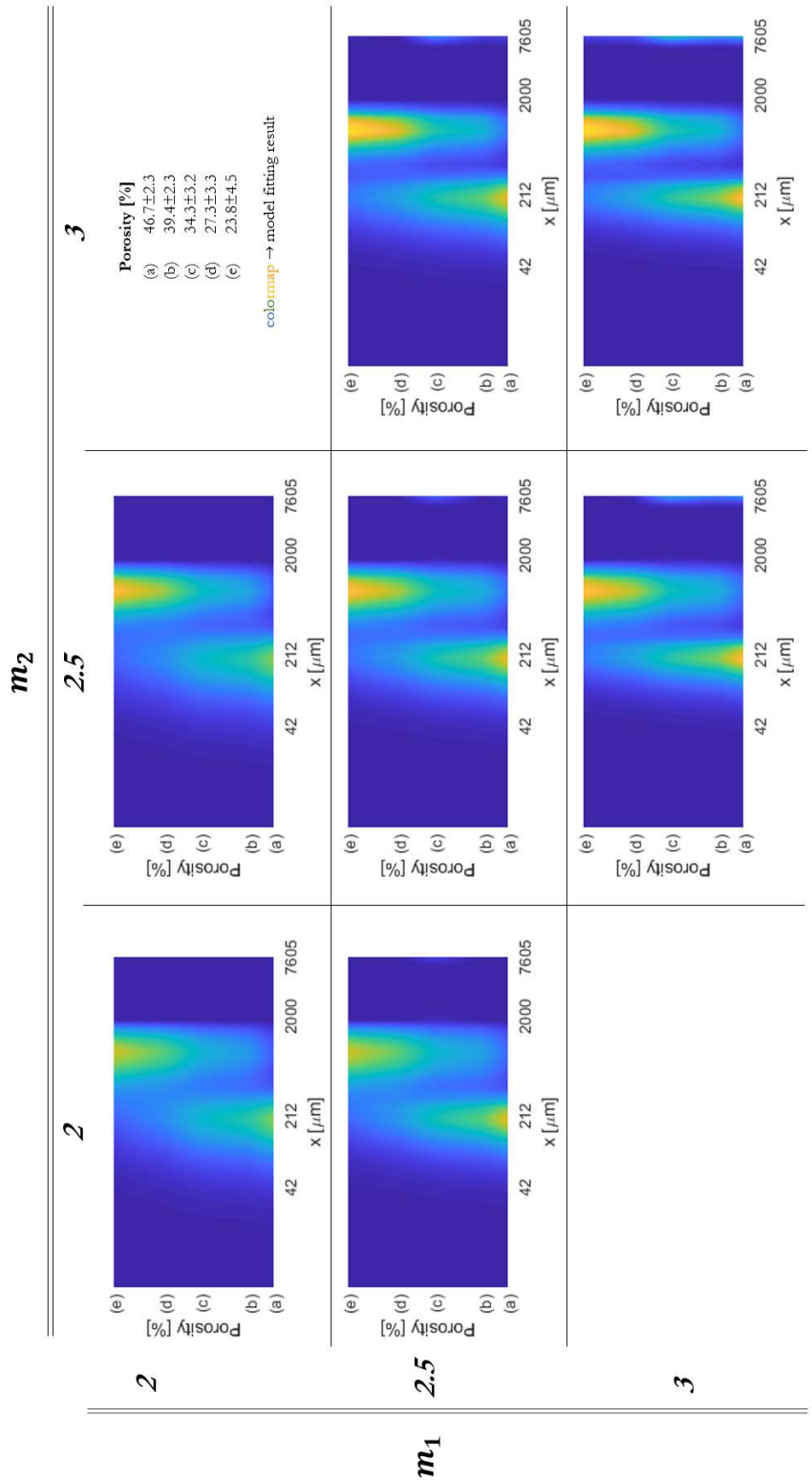

Fig. 5.23. XY view of 3D surface plots of the granule size distributions as a function of porosity for seven meaningful combinations of m_1 and m_2

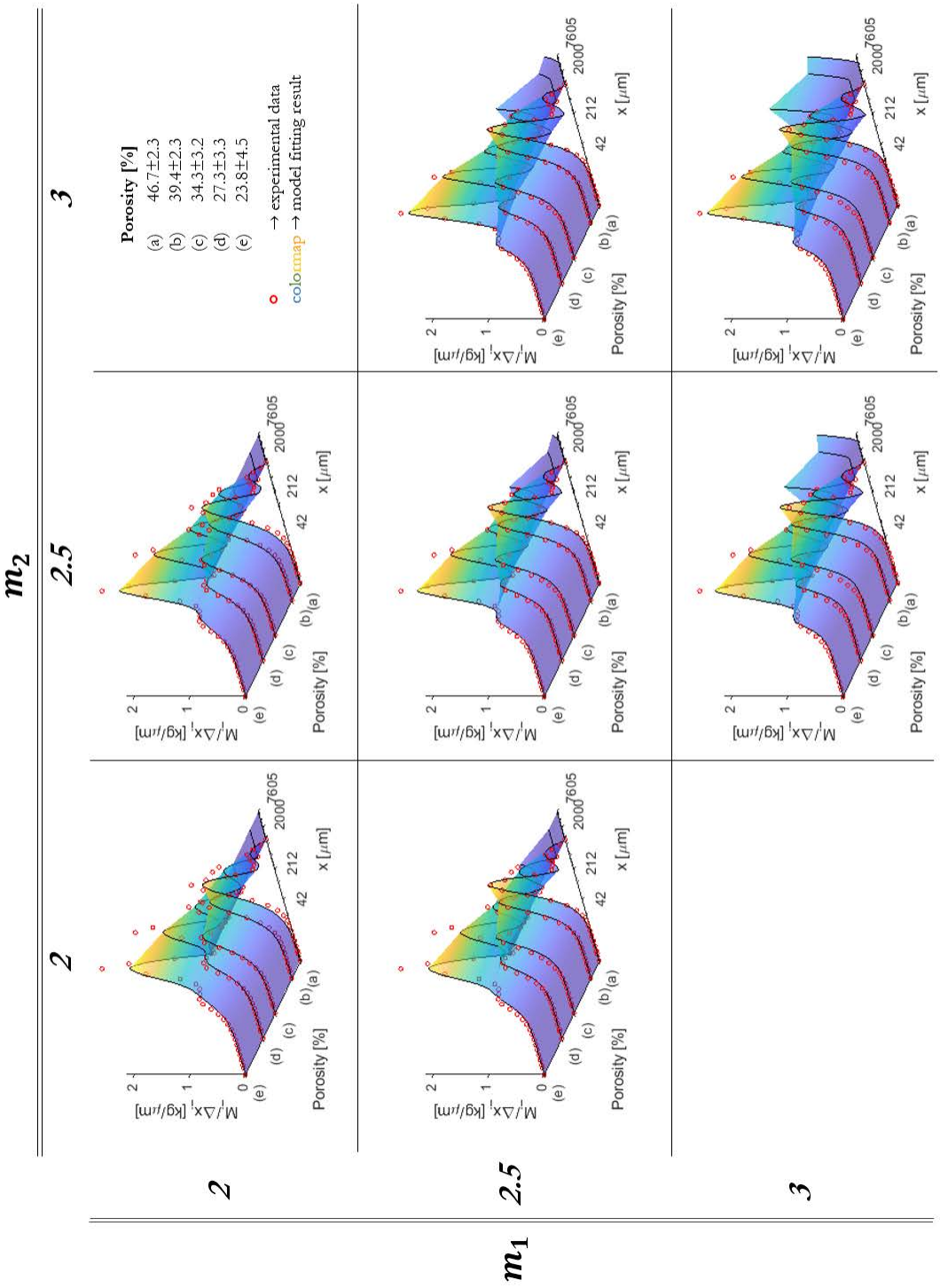

Fig. 5.24. 3D surface plots of the granules size distributions as a function of porosity for seven meaningful combinations of m_1 and m_2

Indeed, most of the other pairings would lead to an overestimation of the upper size class. The previous optimum pair ensures a good trade–off capable to properly fit the experimental data despite a slight underestimation of the two peaks.
Up to this point, the model has been refined into just two parameters, whose trends as a function of the porosity will be reported in Figure 5.25.

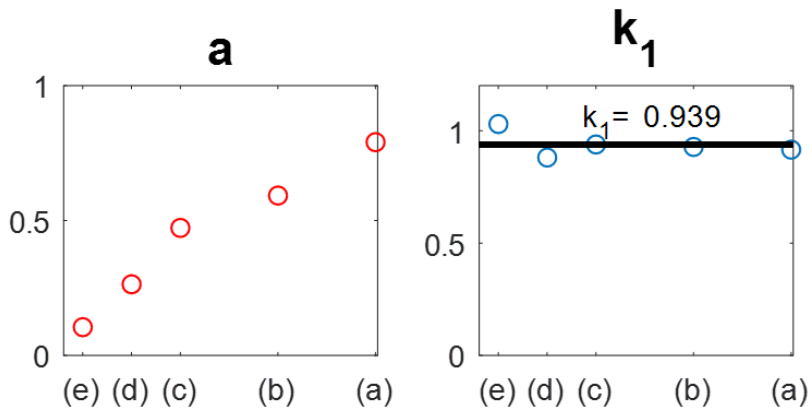

Fig. 5.25. Parameter estimation as a function of different tablet porosity after model refinement

Figure 5.25 shows that also the parameter k_1 is constant along the five tablet batches despite the different porosities. The only model parameter which is really capable to account for different feed ribbon porosity is *a*.

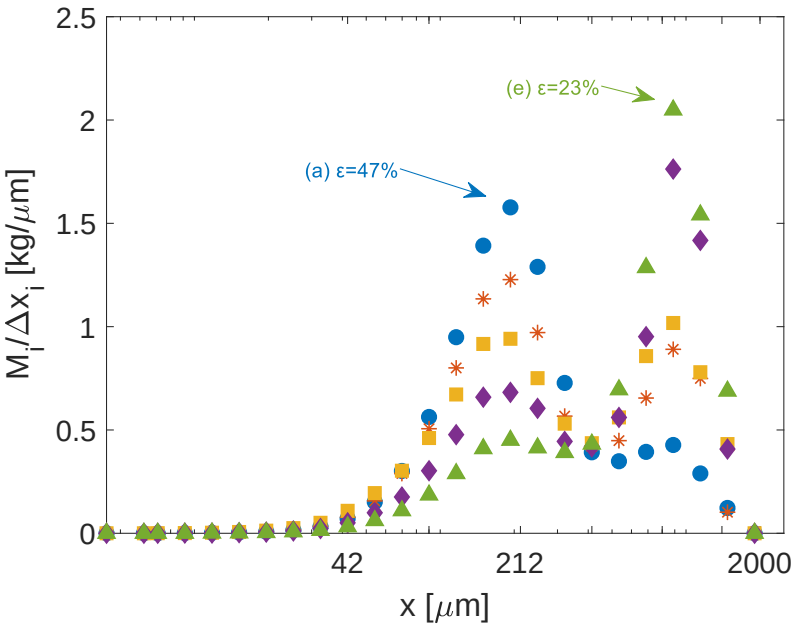

Fig. 5.26. Experimental milled granule size distributions as a function of tablet porosity

From the experiments one can observe that what is actually changing in the milled granule size distribution moving along the porosity domain is the proportion between the two modes. Figure 5.26 illustrates the experimental results, in particular one can notice that the lower the porosity, the lower the first peak whereas the second one will increase. The model parameter a is responsible for predicting how the proportion between the two modes will change depending on the feed tablet porosity. To get reasonable results, it is necessary to bind the a values within the range [0,1]. Theoretically, it is possible to achieve a tablet porosity of 0% applying an infinite compression pressure; in that extreme case, the value of a would be 0, since there were not any fines produced from the milling operation. The other outer case occurs when the tablet porosity is maximum, that is when no pressure is applied and the material is still maintained into the powder state. The *natural* porosity of MCC PH-102 was assessed as:

$$\varepsilon_{MAX} = 1 - \frac{\rho_{bulk}}{\rho_{true}} = 78.66\% \tag{5.10}$$

where both ρ_{bulk} and ρ_{true} values were taken from Schiano et al. [31].
Consequently, after having added these theoretical limits, the progress of a against the porosity is:

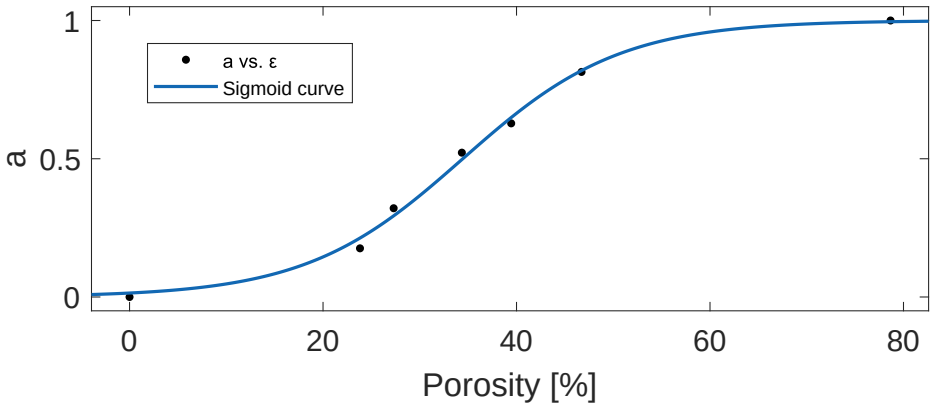

Fig. 5.27. Sigmoid function describing the relationship between a and the porosity

The progress of a along the ribbon porosity is mathematically quantified by the *logistic function*, also called Sigmoid curve function which involves two parameters:

$$a = \frac{1}{1 + e^{-k(\varepsilon - \varepsilon_0)}} \tag{5.11}$$

Fitting the experimental data (reported in Figure 5.27), the parameter values are:

Tab. 5.11. k and ε_0 values involved into the logistic function

k [-]	ε_0 [%]
0.1229	34.45

The S–shaped function perfectly traces the progress of the parameter a along the porosity domain. At the beginning, increasing the ribbon porosity, a will just slightly raise, whereas in the middle of the porosity domain there is a sudden increase of a. In particular, the abrupt transition occurs once the ε_0 is overcome; for this reason, that function parameter can be seen as a *critical porosity*. If the porosity value is below ε_0, a will be lower than 0.5, meaning that the second mode will prevail. On the other hand, if the porosity value overcomes ε_0, then the first mode will dominate.
Finally, the model parameters achieved after the refinement are reported in Table 5.12:

Tab. 5.12. Model parameters after refinement

Parameter	**Value**	**Units**
m_1	2	-
m_2	2.5	-
p_1	210	μm
p_2	988	μm
a	$a = \frac{1}{1+e^{-0.1229(\varepsilon-34.45)}}$	-
k_1	0.939	$1/s$
k_2	1	-
σ	0.0494	-

Through a quantitative analysis was possible to prove that all the parameters involved in the breakage and selection functions, except a, are independent of the ribbon porosity. This set of parameters will be validated in the following section, whereas in the end the model predictions will be presented.

5.9.2 Model validation

To prove the goodness of the model parameter identification, the model validation was performed, checking the predictions both within and outside the experimental domain (Figure 5.28).

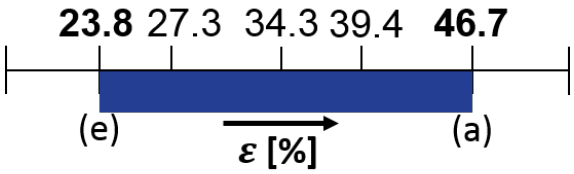

Fig. 5.28. Experimental porosity domain, going from **(e)** to **(a)**

A target porosity of 30 % belonging within the experimental domain was chosen to perform the first model validation. In order to check the model result, the experimental procedure reported in Figure 5.19 was repeated once again to come up with a 6^{th} ribbon batch. Therefore, a new set of 20 tablets was produced through die compaction and then milled adopting the usual 2 mm screen size. The predicted granule size distribution has been experimentally validated:

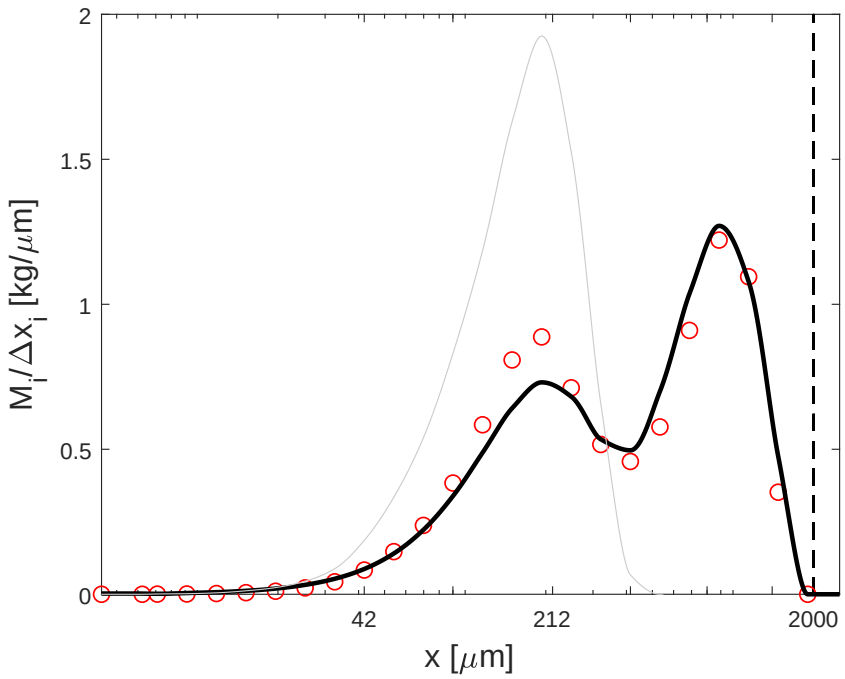

Fig. 5.29. Measured (symbols) and modelled (solid line) milled granule size distribution within the experimental domain. The dashed line stands for the screen size used, while the grey curve represents the fines size distribution

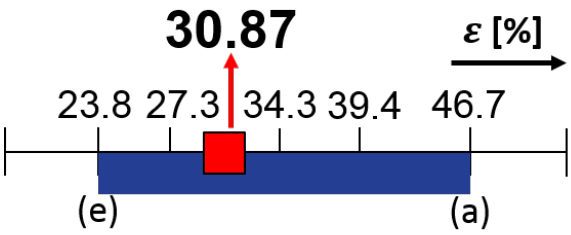

Fig. 5.30. Experimental porosity domain, with detail on the 6^{th} ribbon batch porosity

Figure 5.29 shows that the model can very–well predict the granule size distribution within the experimental field. Despite of the measured points, the model tends to slightly underestimate the first peak corresponding to the fines condition. Moreover, no particles above the screen size are detected by the model, meaning that the classification function was correctly implemented.
Since the objective of dry granulation is the enlargement of the particle size minimising the fines, the further model validation that was performed investigates a porosity value smaller than the lower experimental domain limit. For this reason a 7^{th} ribbon batch was produced, whose average porosity was 21.83 %. Even in this case, the experimental data were obtained in order to compare them with the modelled granule size distribution, assessing in this way the quality of the prediction.

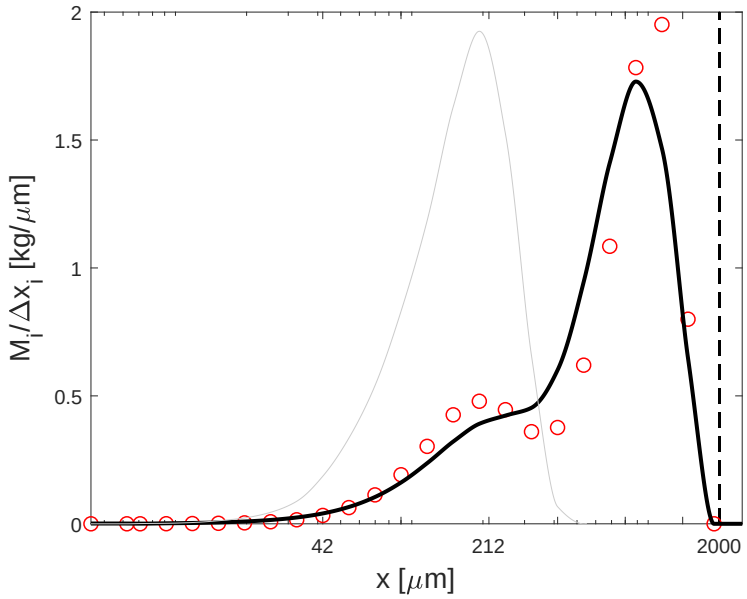

Fig. 5.31. Measured (symbols) and modelled (solid line) milled granule size distribution outside the experimental domain. The dashed line stands for the screen size used, while the grey curve represents the fines size distribution

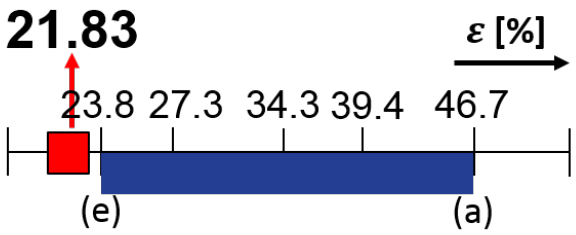

Fig. 5.32. Experimental porosity domain, with detail on the 7^{th} ribbon batch porosity

Decreasing the ribbon porosity has lead to a decrease of the fines after the milling operation which is confirmed both by the experiments and the model result. Definitely the first peak can't be totally deflected since fines will be anyway present, but their proportion in the final distribution was dramatically reduced simply decreasing the feeding ribbon porosity. In terms of model prediction, the quality is still pretty high also outside the experimental field. The model is able to capture the presence of the initial reduced first peak, whereas slightly underestimates the second mode. Also in this case the grey curve corresponding to the powder size distribution was included in the plot in order to prove that the first peak of the milled granule size distribution stands exactly for the fines.

5.9.3 Model prediction

One of the objective of the study was to undestand whether it is possible to achieve a process condition through which the minimisation of the fines is satisfied. Up to this point, the only parameter that can be adjusted to accomplish the project objective is the ribbon porosity. For this reason, a `for` cycle changing the porosity from the powder condition to the hardest ribbons was implemented. The model predictions are reported in Figure 5.33 and Figure 5.34, respectively as probability and cumulative distribution functions. Producing ribbons with high porosity will turn to be useless from the dry granulation point of view since all the materials coming out from the mill is going to come back to the previous powder condition. Viceversa, decreasing the porosity it is evident how the second mode starts to increase. Furthermore, once the critical porosity value ε_0 is overcome, there a switch between the dominant regimes, since the second mode will prevail. According to the model projection it would be possible to achieve a total inversion between the two distribution modes feeding the mill with ribbons at 15 % of porosity. That will result in the fines minimisation condition.

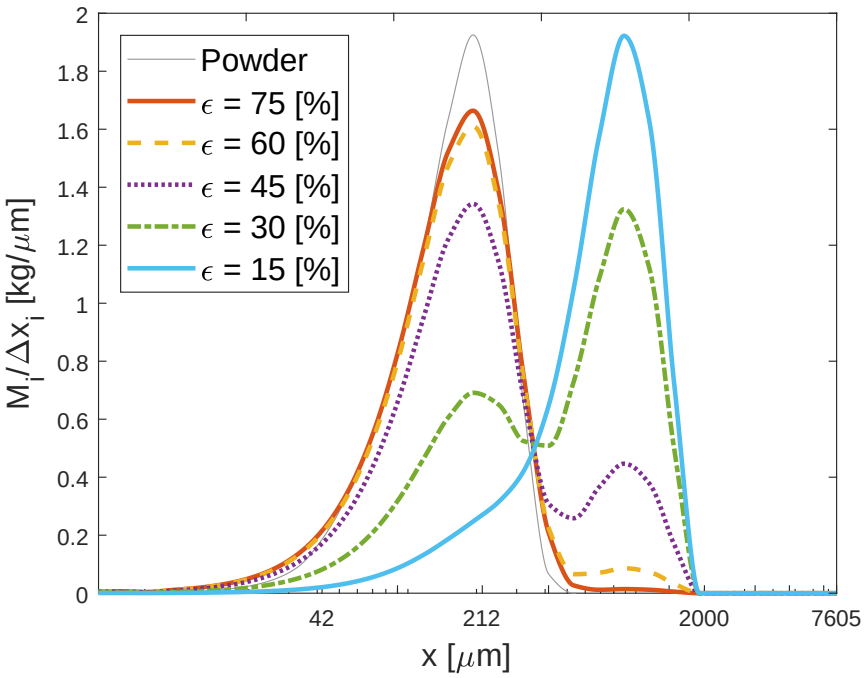

Fig. 5.33. Predicted milled granule size distribution as a function of the ribbon porosity, in PDF form

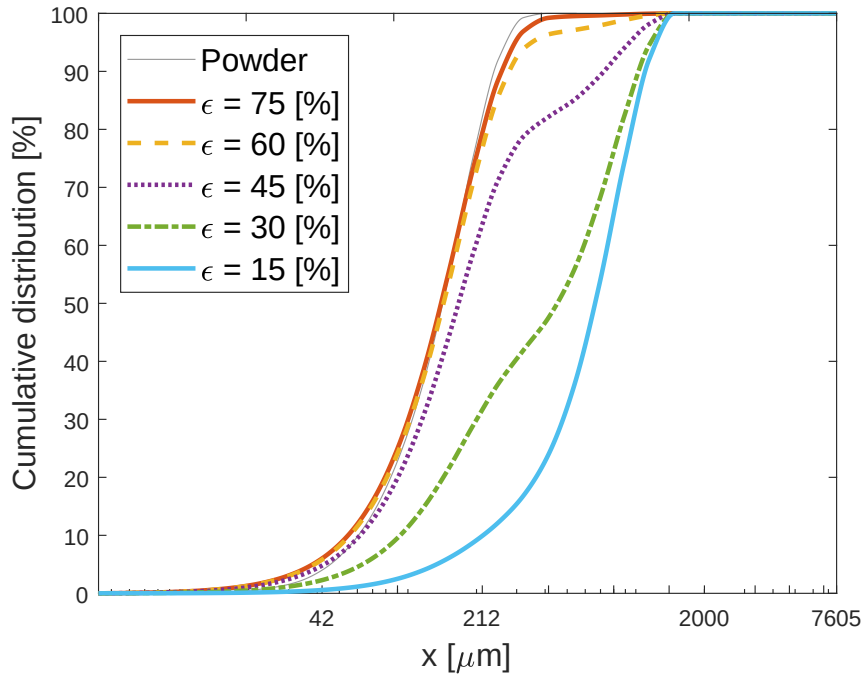

Fig. 5.34. Predicted milled granule size distribution as a function of the ribbon porosity, in CDF form

Once the powerful capability of model has turned out, further analysis can be drawn. To verify the enlargement process in granulation, one important statistical parameter of the distribution is the d_{50}. That parameter corresponds to the particle diameter at which the 50 % of a sample's mass is smaller than and 50 % of a sample's mass is larger than. Statistically, the d_{50} is exactly the median of the distribution. Certainly from a granulation process, people expect that the higher the process performance, the higher the d_{50} value. Figure 5.35 shows exactly this trend, meaning that d_{50} increases the lower the feeding ribbon porosity.

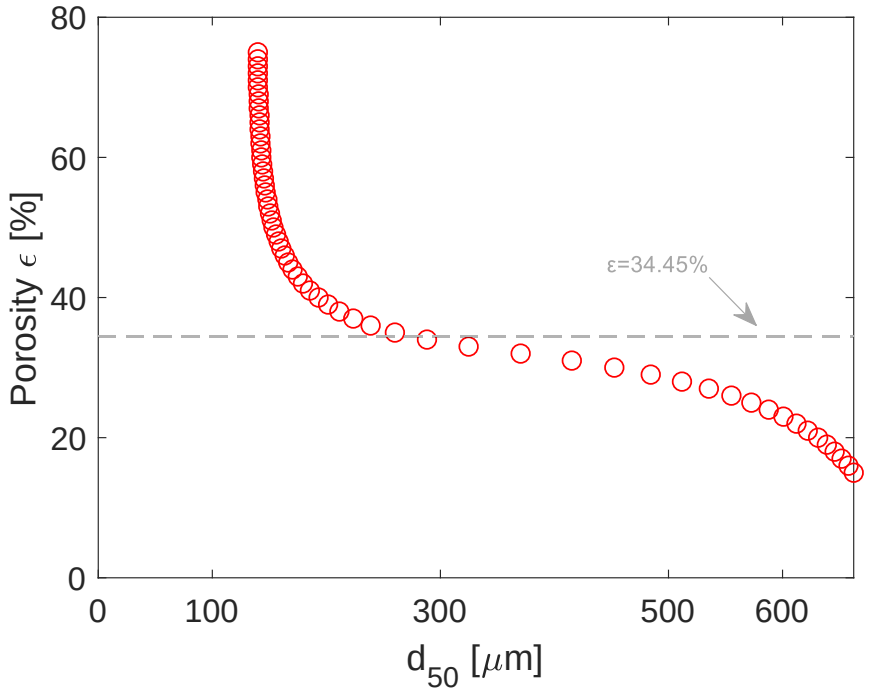

Fig. 5.35. Ribbon porosity plotted against the statistical parameter d_{50}

From the previous figure, it is extremely evident how the d_{50} suddenly increases once that the critical porosity is overtaken. In particular, through dry granulation and starting from ribbons at 20 % porosity, it is possible to triple the d_{50} with respect to the initial value at power state. An another important parameter that describes the distribution is the span, which is formally defined as:

$$span\ \psi = \frac{d_{90} - d_{10}}{d_{50}} \tag{5.12}$$

The span of a mass–based size distribution, named as ψ, gives an indication of how far the 10 % and 90 % points are apart, normalized with the midpoint. In practice,

the span is a statistical descriptor of the width of the distribution. The smaller the value, the narrower the distribution. Dealing with a bi–modal distribution, this statistical parameter can be used to control the granulation process. Ideally people would like to have a distribution which is as steep as possible and located at higher particle size compared to the fines condition. Figure 5.36 illustrates what is the relationship of the ribbon porosity with respect to the distribution span:

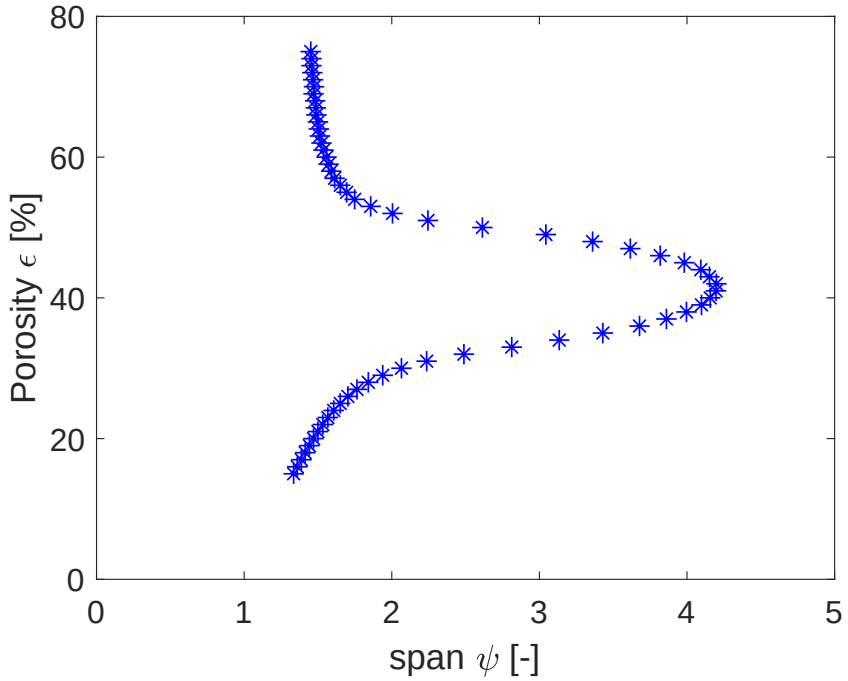

Fig. 5.36. Ribbon porosity plotted against the distribution span

Figure 5.36 highlights that the span distribution dramatically increases for the ribbon porosity range for which the milled granule size distribution is bi–modal because of course that condition corresponds to the largest distance between the 10 % and 90 % points. Moreover, one can notice that the width of the distribution of the powder state is quite similar to the lowest ribbon porosity case. This is again a confirmation of the optimum process condition encountered when the process handles ribbons with as low as possible porosity.

Chapter 6

Mechanistic analysis

In Chapter 3, a brief introduction of the compressibility analysis has been shown. In particular, the Heckel and the Kawakita models mathematically quantify the pattern of the compression force along the deformation. Two parameters per each model have been presented and they have a precise physical meaning. The objective of this Chapter is to develop a mechanistic analysis of the compression process, aiming to point out any possible dependence between the model parameters and the ribbon porosity. The research question turns out as:

Can we improve the understanding of compression processes correlating the ribbon porosity with the parameters of well–established models?

6.1 Compressibility analysis

Owing to the great relevance of compressibility in pharmaceutical industries, compressibility behaviour of several materials have been already characterized in the literature. For example, Zhang et al. [42] studied the compressibility of different grades of pharmaceutical excipients, such as MCC and lactose. Furthermore Sun and Grant [34] investigated the size effect on compressibiltiy behaviour of powders; the compression analysis of powder was studied using the Heckel equation to calculate yield stress and the results showed that the yield stress increases with increasing particle size. This was consistent with the results obtained by York [39] and more recently by Khomane and Bansal [18]. However, the Heckel plot has limitations, which were observed by Patel et al. [24]. At higher compression forces,

no particular trend was observed which was attributed to the nullification of the effect of the particle size due to the extensive fragmentations at higher compaction pressure.

First of all, it is important to describe the several mechanisms taking place during the compression. In the Figure 6.1 it is possible to synthetize the major steps involved in powder compression, as described by Salbu [29]. Each stage represents a certain part of the pressure range used, starting from the initial particle rearrangement, the particle fragmentation, the particle plastic deformation and finally the elastic deformation of the compact. Initially, at low compression pressures, the particles are brought closer together. At a certain applied pressure, the particles reach a maximum attainable packing structure and any further particle movement becomes impossible. Therefore, the following volume reduction is associated with changes in the dimensions of particles. These ones might occur both temporarily by elastic deformation and permanently by plastic deformation. Finally, in the decompression phase, *i.e.* when the applied pressure is removed, the particles may expand due to elastic recovery.

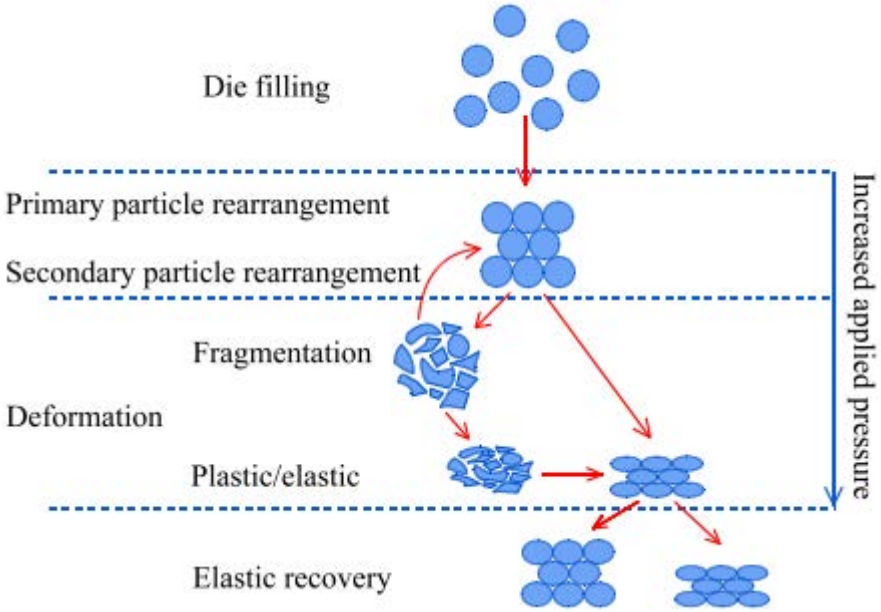

Fig. 6.1. Schematic illustration of the powder compression cycle

6.1.1 Force vs displacement

The output of the Instron® press depicts the progress of the compression force against the deformation. It is extremely important to measure the initial height

of the powder bed. Calling h_0 the initial condition, it is possible to monitor the progress of the powder bed height into the die subtracting the initial value for the current deformation. The trend of the ribbon thickness along the process is directly linked to the change in the bulk density, hence in the ribbon porosity.

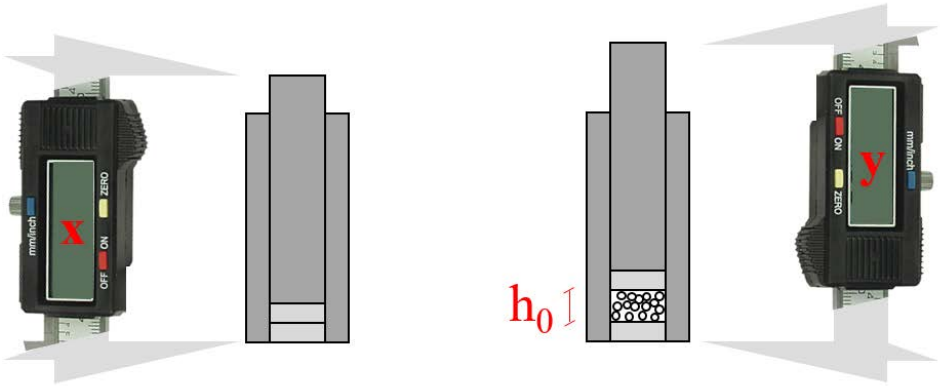

Fig. 6.2. How to measure the initial height of powder into the die

Therefore, looking at Figure 6.2, h_0 is calculated as:

$$h_0 = y - x \tag{6.1}$$

The Heckel equation provides a method for transforming a parametric view of the force and displacement data to a linear relationship for the materials undergoing compaction. In order to apply this model, it is necessary to know the profile of the bulk density along the compression. Firstly, calling γ the displacement, the progress of the powder height into the die along the process time is computed as:

$$h(t) = h_0 - \gamma \tag{6.2}$$

Secondly, the change in the powder height leads to a change in the bulk density (ρ_B) during the compression:

$$\rho_B(t) = \frac{M}{V} = \frac{M}{\pi/4 D^2 h(t)} \tag{6.3}$$

Finally, the relative density plotted in the Heckel plot (Eq. 3.5) is defined as the ratio between the bulk and the true density:

$$\rho_R(t) = \frac{\rho_B(t)}{\rho_{true}} \tag{6.4}$$

After the mathematical premise, the Heckel plots are now illustrated:

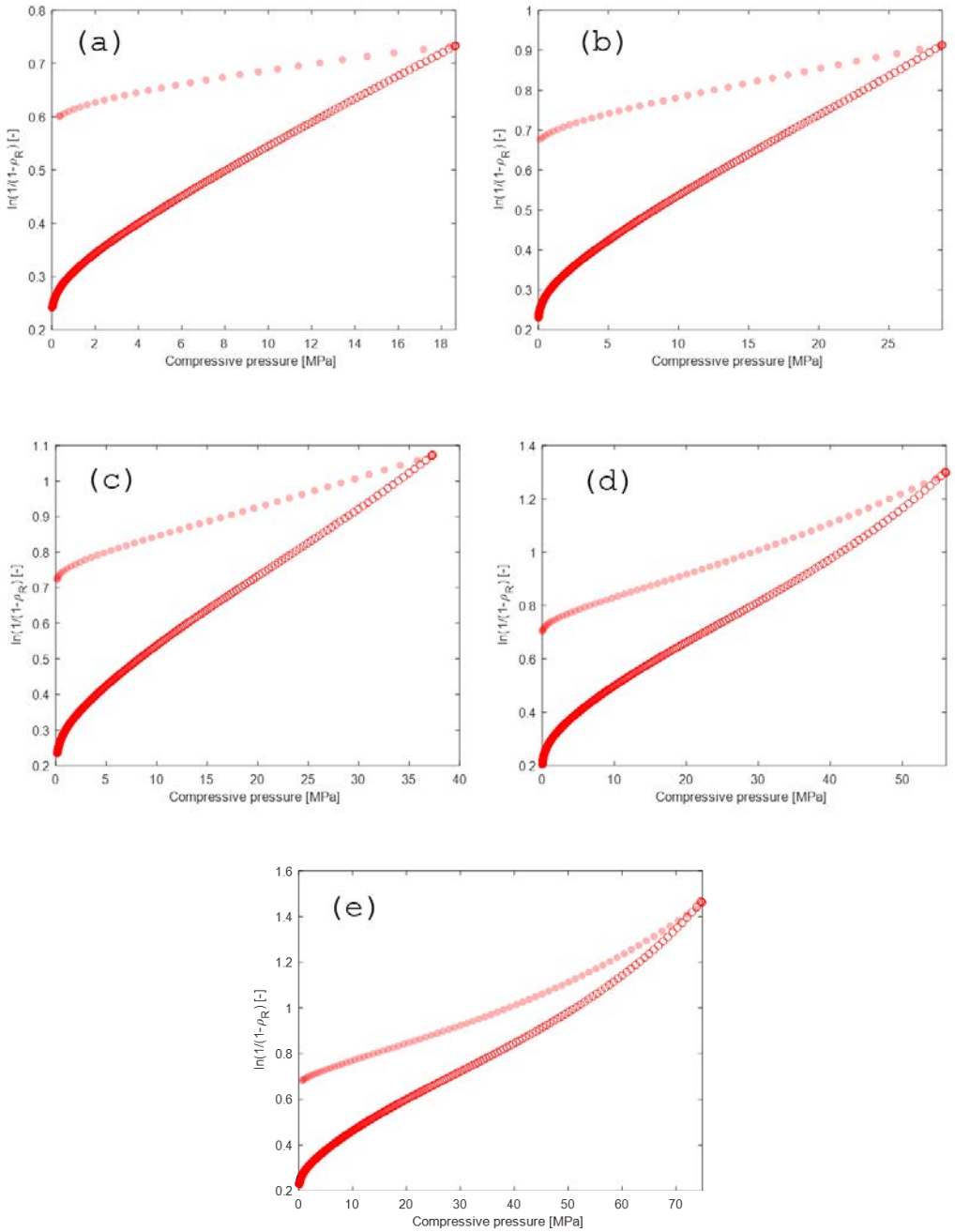

Fig. 6.3. Heckel plots for the five ribbon batches, from (a) to (e)

The mechanistic analysis involves just the loading contribution of the compression process. For this reason the unloading part has been plotted in transparency. Analyzing the previous plots, it is clear that the linear behaviour predicted by Heckel holds true mostly for low compression pressures. In particular, for batches (d) and (e), the plots bend after a certain pressure.

The relationship between the force and the displacement can be also examined applying the Kawakita model. In this case, it is required to know the pattern of the

degree of volume reduction C along the compression. Through the measurement of the initial powder bed, its trend is calculated as:

$$C(t) = \frac{V_0 - V}{V_0} = \frac{\pi/4D^2h_0 - \pi/4D^2h(t)}{\pi/4D^2h_0} \tag{6.5}$$

Referencing to Eq. 3.8, the Kawakita plots for each ribbon batch will be presented:

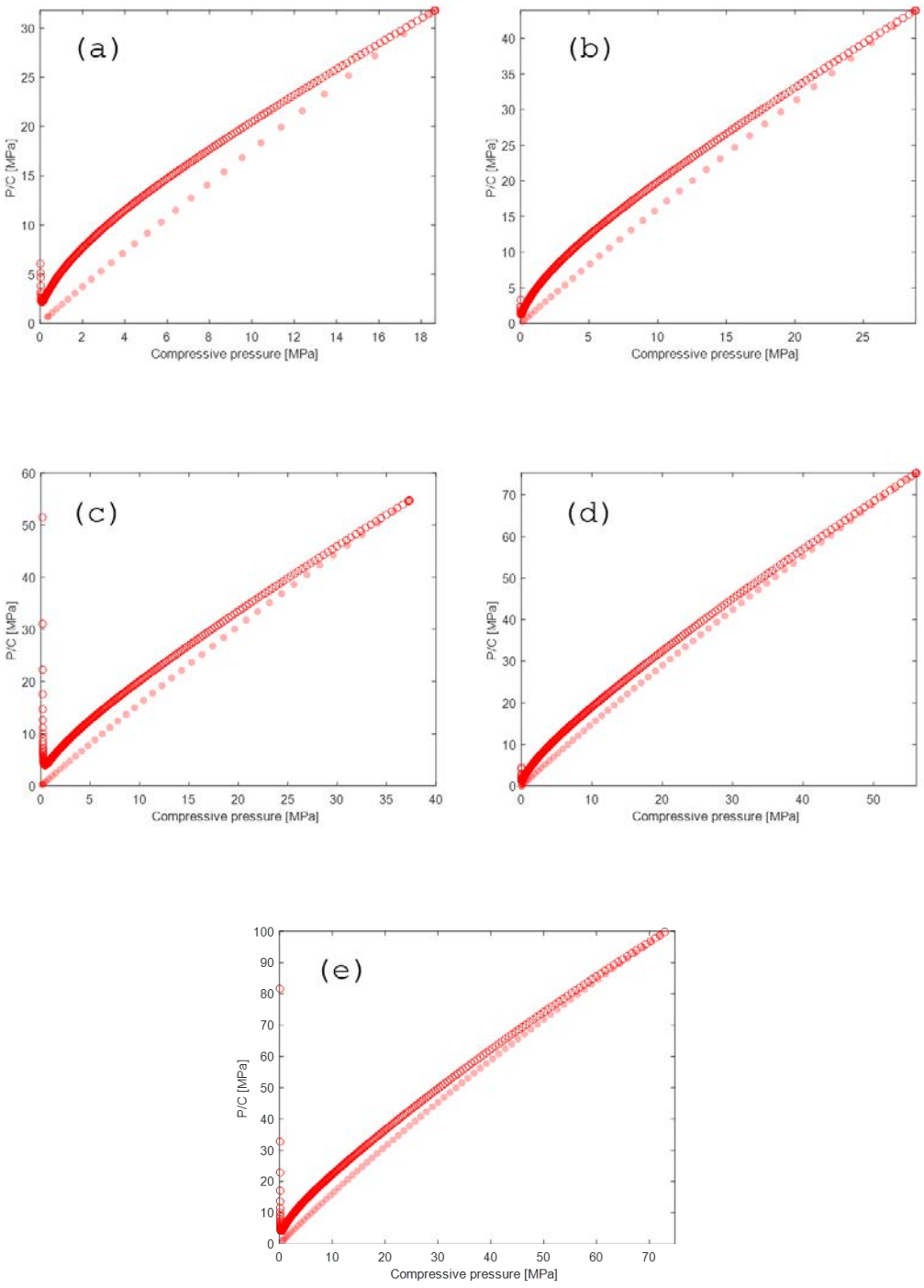

Fig. 6.4. Kawakita plots for the five ribbon batches, from (a) to (e)

Once that the experimental data have been plotted, the parameter identification was performed. For both the model, the estimation was carried out just within the pressure range that highlights a linear behaviour. In the following analysis, all the experimental runs were used in order to appreciate the variability between the ribbon porosities, but also within the same batch. The result of the analysis has been depicted as follows; for each ribbon batch, a scatter plot of the experimental runs was included, whereas along–side there is a histogram distribution of the paramater distribution. The first row of each `subplot` refers to the Kawakita parameters (a and b), while the second one stands for the Heckel parameters (A and k). Among all the batches, the largest variabilities can be observed in the `(b)` and `(d)` ones.

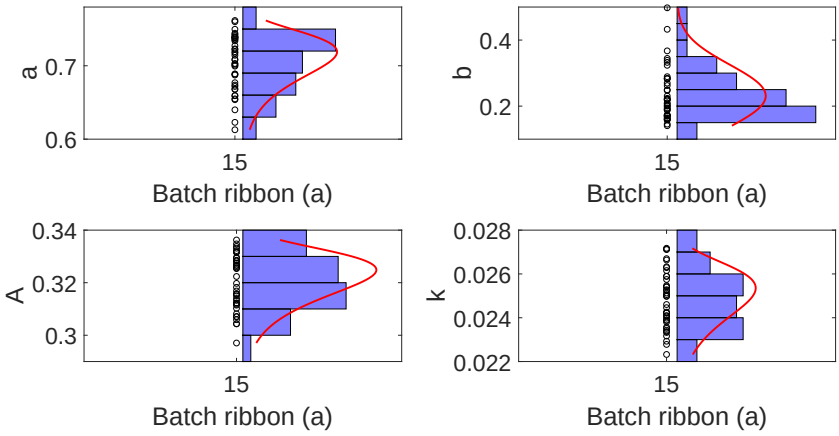

Fig. 6.5. Parameter estimation for ribbon batch `(a)`

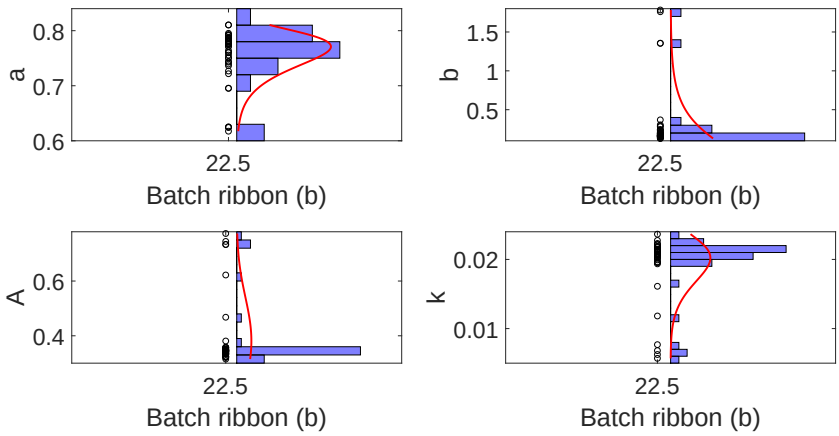

Fig. 6.6. Parameter estimation for ribbon batch `(b)`

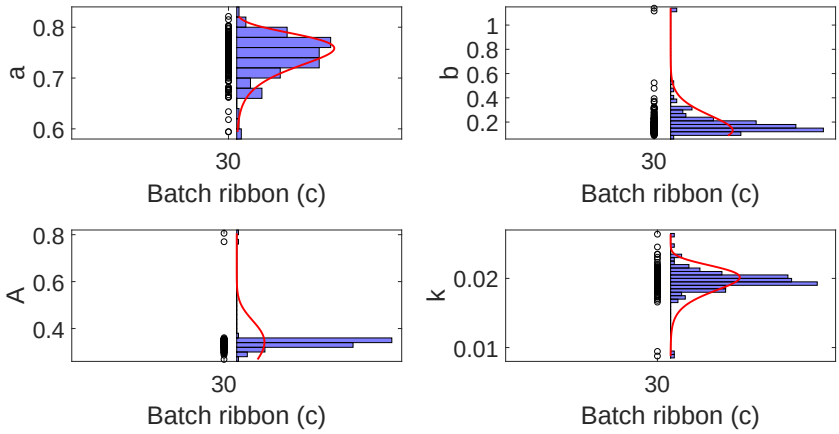

Fig. 6.7. Parameter estimation for ribbon batch (c)

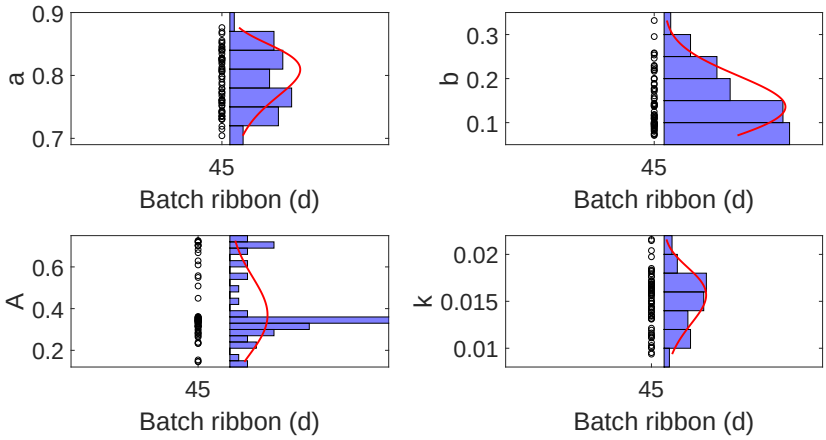

Fig. 6.8. Parameter estimation for ribbon batch (d)

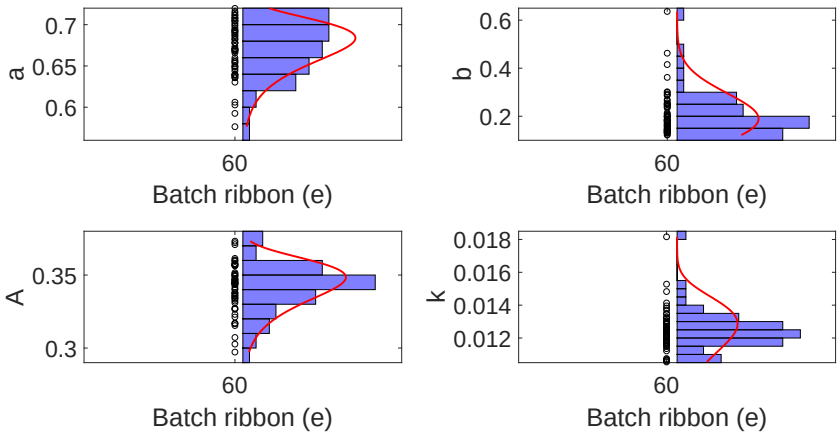

Fig. 6.9. Parameter estimation for ribbon batch (e)

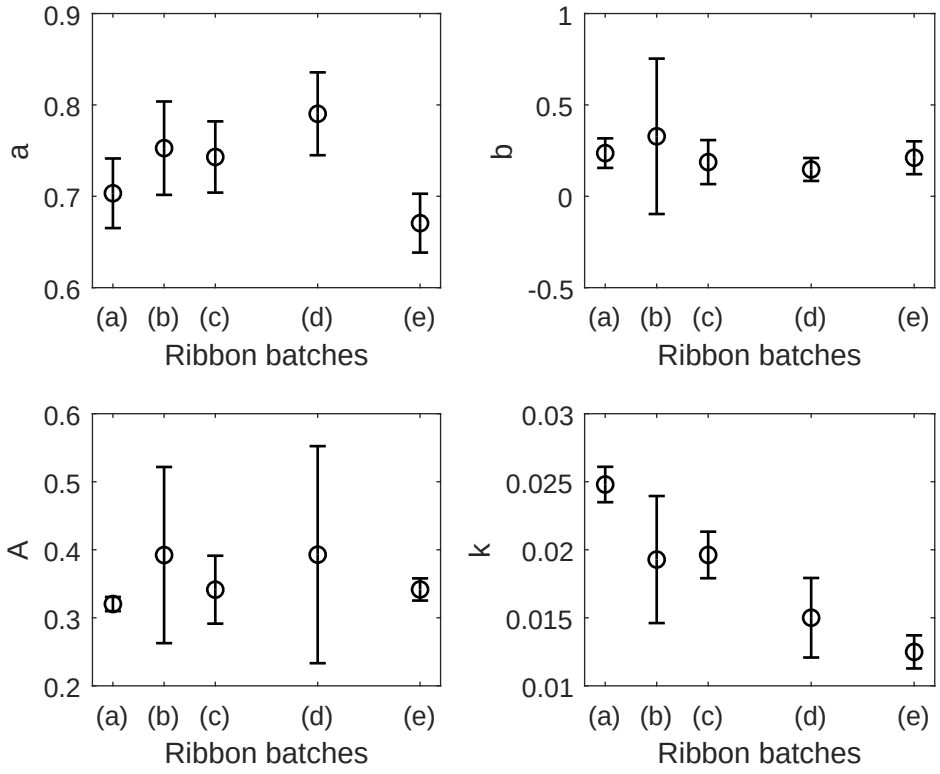

Fig. 6.10. Parameters pattern for the five ribbon batches

The Heckel parameters were estimated applying the "zero pressure" or "out–of–die" method of data collection. In this way, the relative density is measured on the compacts after relaxation following ejection from the die. The results regarding the slope of the Heckel plot reported in Figure 6.10 are consistent with [18]. Furthermore, the estimated values of a and b involved in the Kawakita model are comparable with Zhang et al. [42]. Interestingly, even if theoretically the parameters involved in the Heckel and Kawakita should be material constants, it is clear that the slope of the Heckel plot depends on how dense the powder is compressed. This result was for the first proved by Patel et al. [24] in 2007. Thereafter in 2010 Patel et al. [25] published a second article, enlarging the number of materials analysed. They found that the apparent mean yield pressure from Heckel analysis was significantly affected by the applied pressure.

6.1.2 Energy analysis

As discussed in Chapter 3, the mechanistic analysis of the compressibility must take in account also the energy point of view. In particular it is expected that the higher the compression pressure, the higher the energy required. The energy required for the compression is exactly equal to the area below the curve referring to force against displacement, whose raw data are available directly from the press.

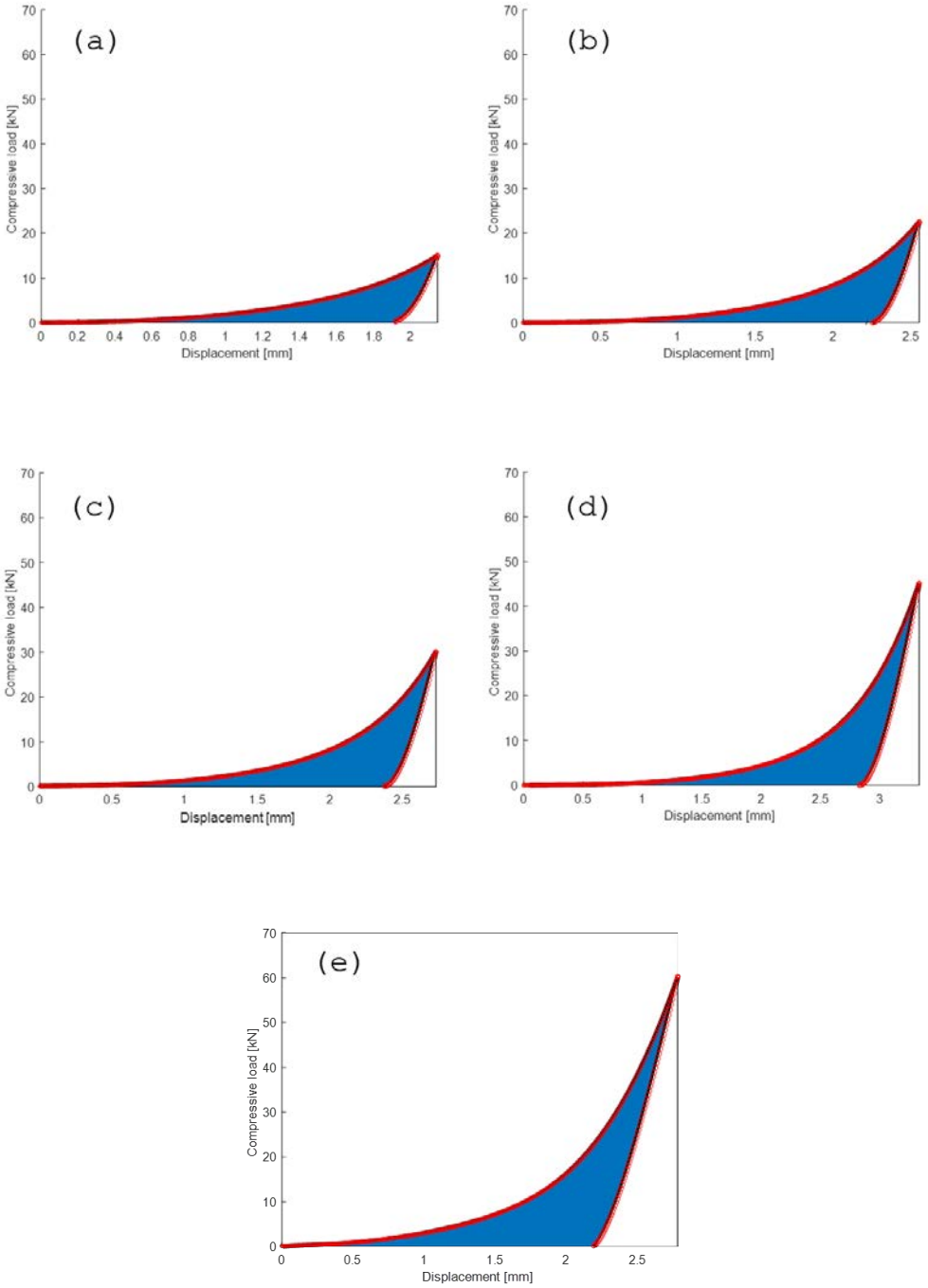

Fig. 6.11. Compressibility energy depending on the ribbon batch

Assignin a constant y–axis limit ensures a better understanding on the increase of the compressibility energy for the five different ribbon batches. Furthermore, it is awaited a higher elastic recovery increasing the applied pressure, hence decreasing the porosity. This speculation is confirmed looking at Figure 6.11, where it is clear that the proportion between the two areas is steadily changing (§3.2.3). Also in this Section, the results are now reported in order to highlight both the variability within the single ribbon batch, and the changes among the five batches.
Figure 6.12 to Figure 6.16 illustrate the low variability of both compressibility energy and elastic recovery within each single ribbon batch. This result can be drawn also looking at the `errorbar` in Figure 6.17. The variability seems to go up increasing the compression force, since for the highest porosity batch the calculations of both energy and elastic recovery are included into a narrow range.

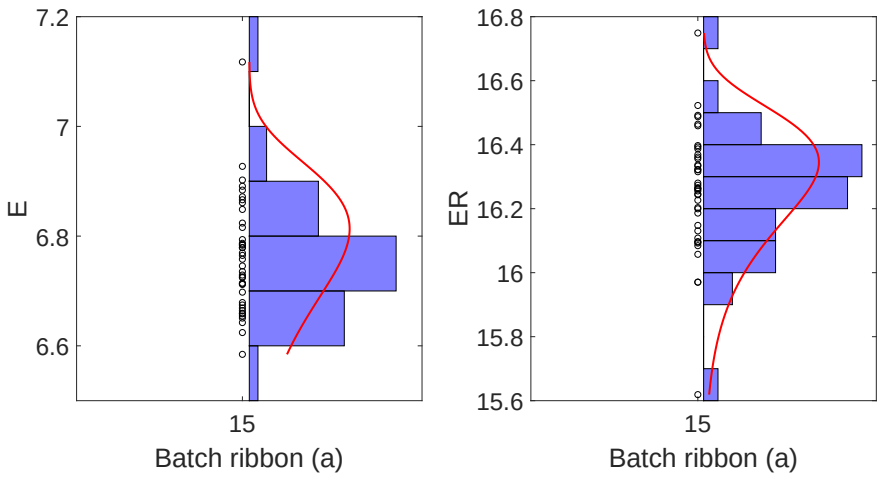

Fig. 6.12. Compressibility energy and elastic recovery for ribbon batch (a)

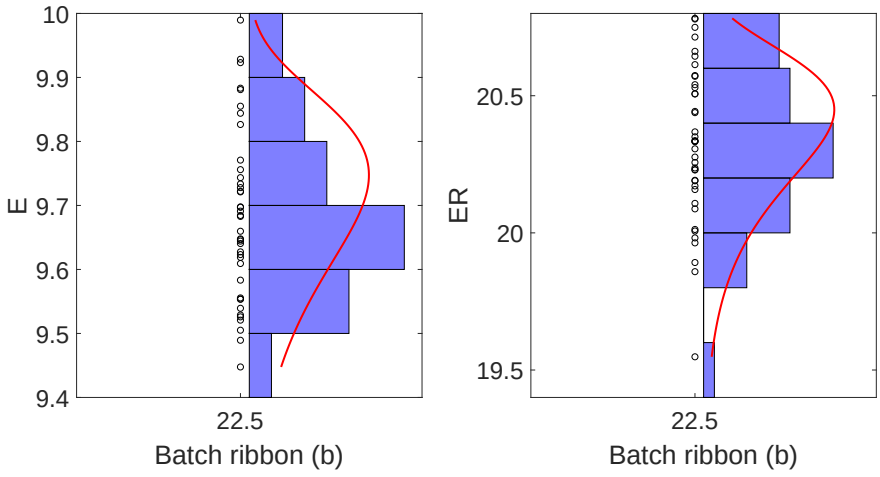

Fig. 6.13. Compressibility energy and elastic recovery for ribbon batch (b)

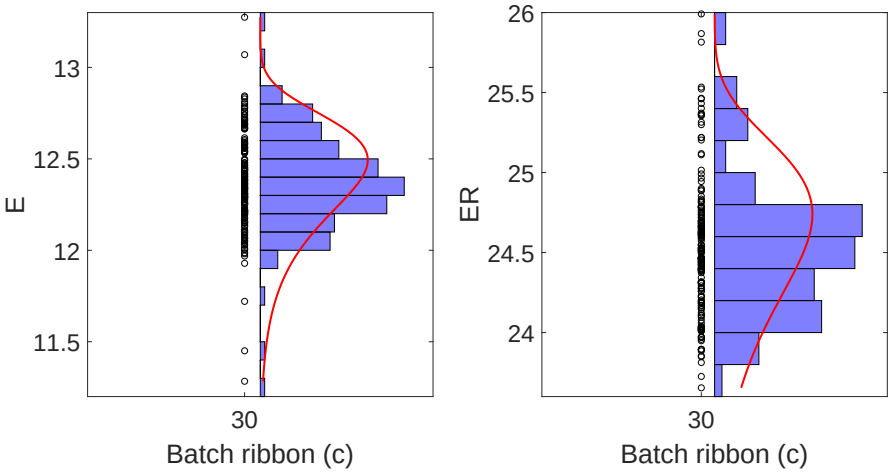

Fig. 6.14. Compressibility energy and elastic recovery for ribbon batch (c)

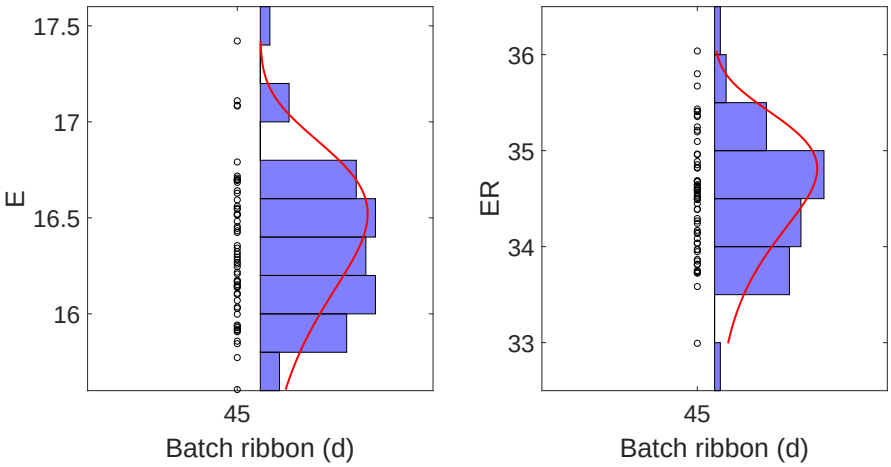

Fig. 6.15. Compressibility energy and elastic recovery for ribbon batch (d)

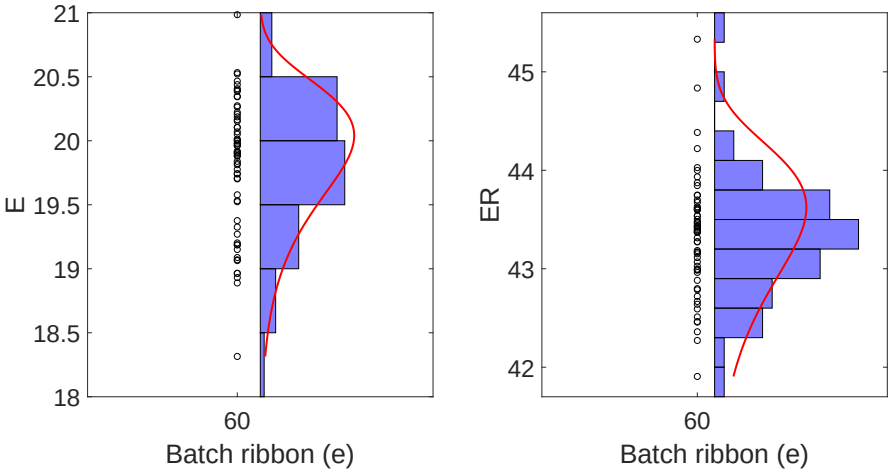

Fig. 6.16. Compressibility energy and elastic recovery for ribbon batch (e)

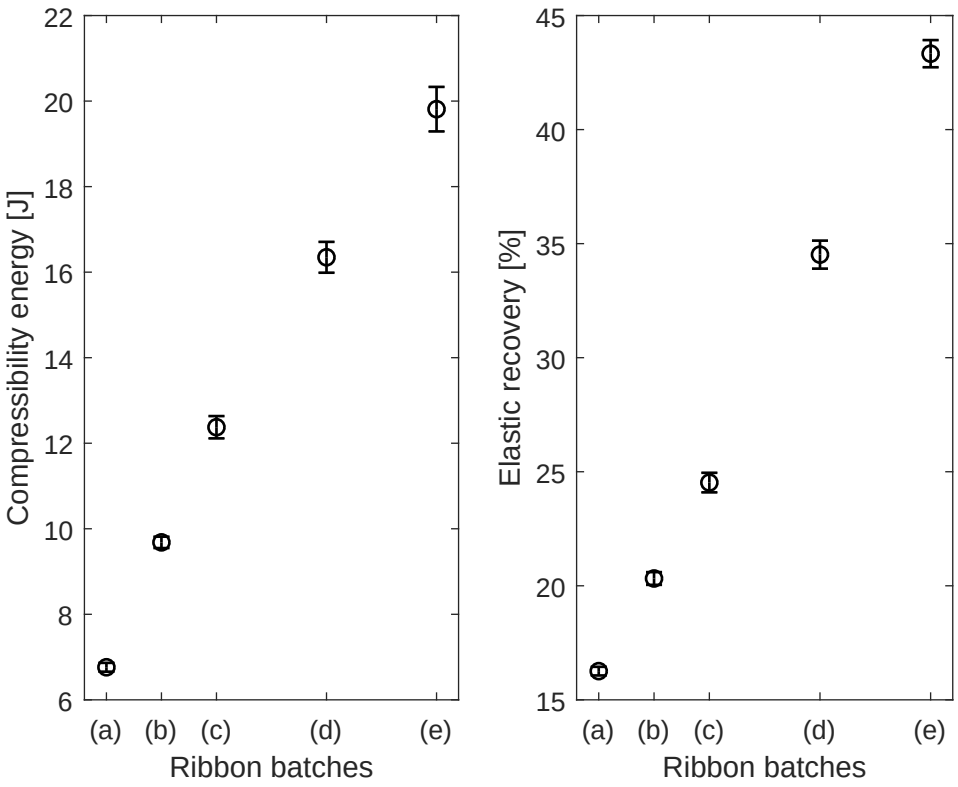

Fig. 6.17. Compressibility energy and elastic recovery pattern for the five ribbon batches

The results reflect the initial expectations. The compressibility energy roughly triples, from the 7 of batch (a) to 20 J of (e). A similar upward trend is shown by the elastic recovery, that almost hits 45 % for the lowest ribbon porosity.

As further analysis, the compressibility analysis according to the energy point of view has been repeated. In this latter case, the die compaction experiments were carried out starting with the granules produced after the ribbon milling. The objective was to prove that the size enlargement leads to a lower compression energy, but also to a higher elastic recovery. Indeed there are evidence in the literature (York [39]) for which large particles produce tablets with larger pores than fine particle. In other words, the reduction of pores size due to plastic deformation is less efficient for larger particles. Therefore, the volume reduction for coarse particles is slower than fine particles at a given compaction pressure. This will lead to a higher elastic recovery.

Comparing Figure 6.18 to Figure 6.17, it is clear that the compressibility energy decreases when the compacts are produced with granules. On the other hand, producing tablets feeding the die with granules will also cause an increase in the elastic recovery.

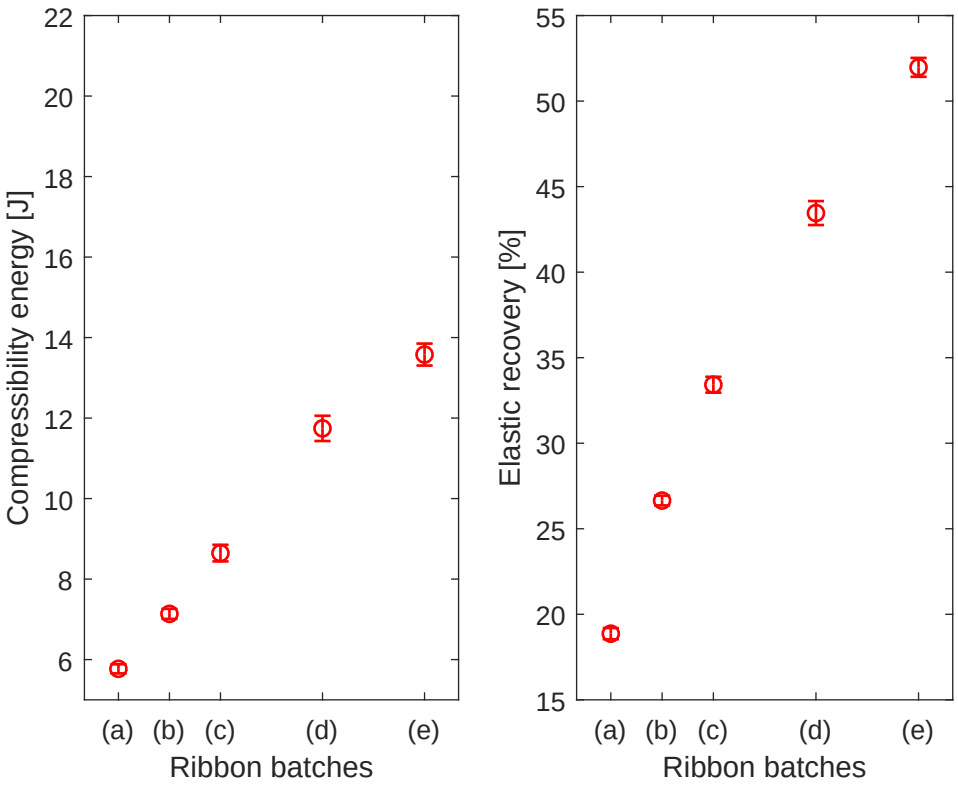

Fig. 6.18. Compressibility energy and elastic recovery pattern for the five granules batches

6.2 Die filling experiments

The major purpose of dry granulation is to enhance the capability of the solids to flow. Flowability is a key property of solid materials and its improvement can lead to several advantages in the downstream operations of a pharmaceutical industries. The objective of this last Section of the thesis is to prove the effective increase in the material flowability, using the rotary die filling device described in Chapter 2 (§2.5).

6.2.1 Powder

The powder flowability was assessed indirectly through die filling experiments. They were performed on pure powders using the methodology reported in Chapter 2. Applying the model proposed by Wu et al. [38] and fitting the experimental data, it is possible to calculate both the critical velocity and the exponent n. In particular, the lower the critical velocity, the highest the powder flowability. As previously mentioned, this type of experiment was carried out just on the ribbon batch (c), since a huge amount of materials was necessary to fill up the shoe.

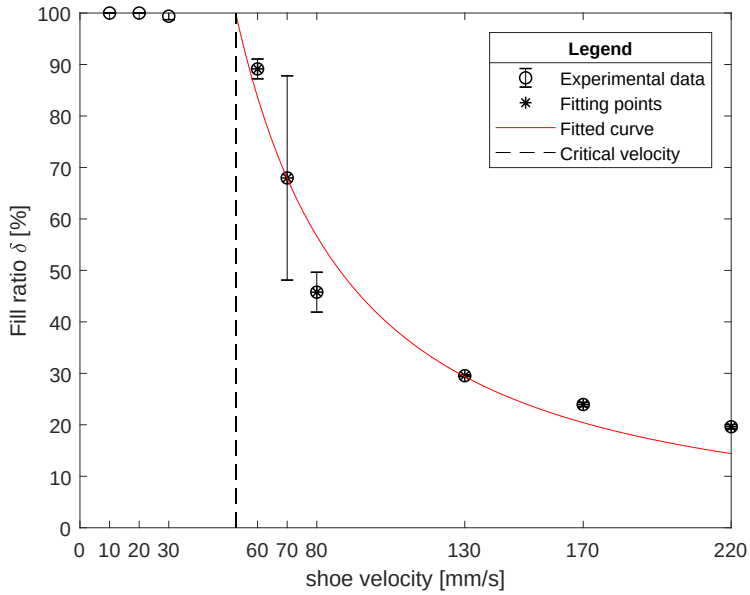

Fig. 6.19. Die filling experiments for MCC PH–102 powder

Tab. 6.1. Parameter estimation of die filling

$\mathbf{V}_c$ [mm/s]	**n** [-]
52.58	1.35

Figure 6.20 illustrates the progress of the fill ratio δ against the shoe velocity. Naturally it is expected a decrease of the fill ratio increasing the shoe velocity, since the residence time of the die below the shoe will be lower. Nine different velocities covering a range from 10 to 220 mm/s were chosen to enlarge the experimental domain as much as possible. For each shoe velocity, three different measurements were taken. In the region within which it is experienced a sudden decrease of the fill ratio, it is also observed the highest variability. The fitting results are reported in Table 6.1.

6.2.2 Granules

Filling ratio is not a material property, however it is an experimental output which helps in the understanding of the influence of process parameters (*i.e.* shoe speed) or materials properties (*i.e.* size) on flowability behaviour of powders. In order to fill up completely the shoe producing valid results, 100 g of materials were necessary. This material availability was satisfied just for the batch (c), for which a lot of tablets were produced. The methodology followed during the experiments

is exactly the same reported in Chapter 2. To prove the amelioration of flowability coming out from dry granulation process, a comparison between the parameters model of powder and granules is presented.

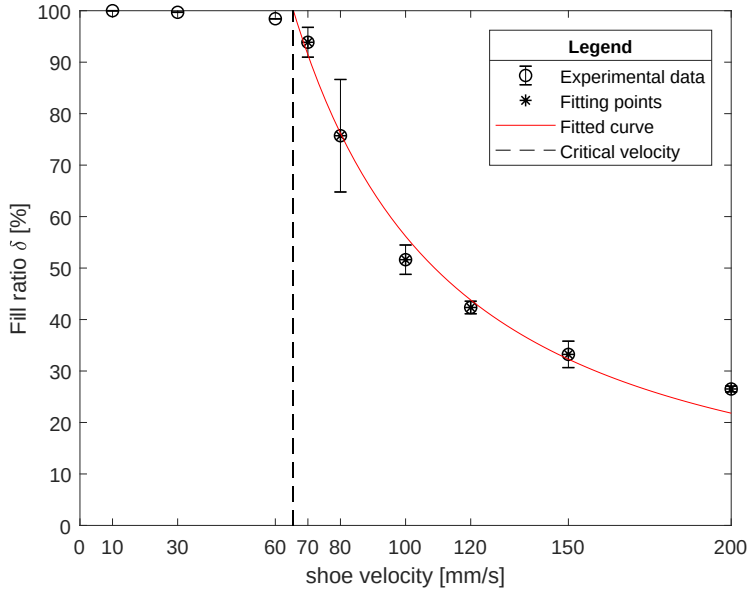

Fig. 6.20. Die filling experiments for MCC PH–102 granules from (c)

Tab. 6.2. Parameter estimation of die filling

$\mathbf{V}_c$ [mm/s]	**n** [-]
65.55	1.36

Comparing the parameters in Table 6.2 with the ones referred to the powder, it is clear that the exponent n is constant, whereas the critical velocity V_c changes. In particular, the granules V_c is roughly 20 % more than the powder one. This results showed that for a higher fill ratio were obtained for granules at a given shoe speed. This led to the conclusion that granules have an higher flowability with respect to the powder because more mass was deposited into the die. In other words, to achieve a given filling ratio value, lower shoe speeds are required for finer particles. Therefore, it can be concluded that granules have higher flowability than fines.

Chapter 7

Conclusions

7.1 Summary

The initial main objectives of this study were:

- ✓ To enhance a better control of the ribbon porosity;
- ✓ To improve the performance of dry granulation process during milling;
- ✓ To develop a mechanistic analysis of the compression process.

7.2 Conclusions

Through die compaction it was possible to produce circular ribbons with a better control in the final porosity. Indeed it was proved that the variability of the porosity within each single batch is quite narrow. Moreover the manufacture of five ribbon batches with different porosities allowed to study the effect of ε in the dry granulation process. In particular, one of the major issues affecting the dry granulation is the production of fines during the milling operation. In order to improve the understanding of this process, tackling the problem of fines generation, a numerical approach has been adopted. Therefore a new mass–based breakage function coupled with mass-based population balance model for ribbon milling has been developed. The model showed good agreement with the experimental data ensuring a proper parameter estimation. Furthermore it was possible to refine the model, through a detailed study on the effect of the porosity on the final

granule size distribution. After the model refinement, just one parameter has been proved to be porosity–dependent. The model can predict the granules size distributions quite well. Indeed, both the predictions within and outside the experimental domain have been positively checked. Finally the application of the population balance model allowed to identify the optimum operating condition to minimize the fines.
Moreover in the final part of the work, a complete study of the compressibility has been carried out. The raw data per each compression run were saved and elaborated into a MATLAB® code to develop a mechanistic analysis. Specifically this analysis has been addressed exploiting two well–established mathematical models. It was found that the slope of the Heckel plot depends on the applied pressure (hence on the ribbon porosity). This funding has been already positively proved by previous studies. The compressibility analysis was developed also from the energy point of view, quantitatively proving that the higher the compression pressure, the higher the compressibility energy but also the elastic recovery. The advantages of the dry granulation in terms of flowability enhancement have been briefly discussed in Section §6.2, in which the results of die filling experiments have been reported.

7.3 Future work

Recommendations for future research in the PBM are as follows:

- To explore different materials, looking for other material constants and compare the parameters.
- To investigate different screens size, enlarging the validity of the model towards multiple operating conditions.

List of figures

List of tables

Symbols

V_c	critical velocity	[mm/s]
V_s	shoe velocity	[mm/s]
n	exponent	[-]
d_{10}	10^{th} percentile	[μm]
d_{50}	50^{th} percentile	[μm]
d_{90}	90^{th} percentile	[μm]
V_p	particle volume	[m^3]
A_p	particle area	[m^3]
k	Heckel parameter	[MPa^{-1}]
A	Heckel parameter	[-]
P_y	Heckel yield stress	[MPa]
C	degree of volume reduction	[-]
a	Kawakita parameter	[-]
b	Kawakita parameter	[-]
V_0	initial volume of bulk solid	[m^3]
V	volume of bulk solid	[m^3]
$\mathbb{E}$	compressibility energy	[J]
$\mathcal{F}(\gamma)$	loading contribution	[kN]
$\mathfrak{F}(\gamma)$	unloading contribution	[kN]
S_i	selection function component	[s^{-1}]
M_i	mass in size class i	[kg]
$b_i j$	breakage function component	[-]
c_i	classification function component	[-]
x_i	particle size component	[μm]
d_s	screen diameter	[μm]
$\mathbf{S}$	objective function	[$kg^2/\mu m^2$]
m_1	breakage function parameter	[-]
m_2	breakage function parameter	[-]
a	breakage function parameter	[-]
p_1	breakage function parameter	[μm]
p_2	breakage function parameter	[μm]
h_0	initial height of powder bed	[mm]
$h(t)$	current height of powder bed	[mm]

Greek letters

δ	fill ratio	[-]
ψ	distribution span	[-]
Ψ	material sphericity	[-]
ρ_B	bulk density	$\left[kg/m^3\right]$
ρ_{true}	true density	$\left[kg/m^3\right]$
ε	porosity	[-]
ρ_R	relative density	[-]
γ	displacement	[mm]
η	milling efficiency	[-]
σ	classification function parameter	[-]

Vectors and matrices

$\underline{S}$	selection function array
$\underline{\underline{b}}$	breakage function matrix
$\underline{c}$	classification function array
$\underline{x}$	particle size array
$\underline{\theta}$	set of parameters
$\underline{\theta}_0$	set of parameters base case
$\underline{\underline{\theta}}_0$	matrix of base case parameters
$\underline{\underline{P}}$	perturbation matrix
$\underline{\underline{\theta}}_\varepsilon$	matrix of perturbated parameters
$\underline{\underline{\mathbf{X}}}$	3D storage matrix
$\underline{\underline{\mathbf{Q}}}_S$	3D sensitivity matrix
$\underline{\theta}_{new}$	set of parameters new

Acronyms

PBM	population balance model
DG	dry granulation
RCDG	roll compaction dry granulation
API	active pharmaceutical ingredient
SEM	scanning electron microscope
ER	elastic recovery

Acknowledgments

Prof. Chuan–Yu Wu
per il supporto e i preziosi consigli trasmessi nell'arco dei sei mesi.

Prof. Andrea Claudio Santomaso
per il sostegno e l'aiuto offerto in fase di revisione del lavoro di tesi.

Prof. Lian Liu
per avermi fornito il background teorico sulla modellazione implementando i bilanci di popolazione.

MSc Anthonia Omeiza
per avermi fornito una prima parte di dati sperimentali utilizzati durante la modellazione

Ufficio 17BC02
ai compagni d'ufficio, per l'aiuto reciproco e i pranzi trascorsi assieme.

Famiglia
per il supporto e i sacrifici che mai sono mancati durante questi anni di formazione.

Amici
per tollerare i momenti di assenza, sapendo apprezzare maggiormente il tempo trascorso assieme.

References

[1] H. Adi, I. Larson, and P. Stewart. Use of milling and wet sieving to produce narrow particle size distributions of lactose monohydrate in the sub-sieve range. *Powder Technology*, 179(1-2):95–99, 2007.

[2] I. Akseli, S. Iyer, H. P. Lee, and A. M. Cuitiño. A quantitative correlation of the effect of density distributions in roller-compacted ribbons on the mechanical properties of tablets using ultrasonics and x-ray tomography. *AAPS PharmSciTech*, 12(3):834–853, 2011.

[3] M. T. am Ende, S. K. Moses, A. J. Carella, R. A. Gadkari, T. W. Graul, A. L. Otano, and R. J. Timpano. Improving the content uniformity of a low-dose tablet formulation through roller compaction optimization. *Pharmaceutical development and technology*, 12(4):391–404, 2007.

[4] L. G. Austin and P. T. Luckie. Methods for determination of breakage distribution parameters. *Powder Technology*, 5(4):215–222, 1972.

[5] C. Bacher, P. Olsen, P. Bertelsen, J. Kristensen, and J. Sonnergaard. Improving the compaction properties of roller compacted calcium carbonate. *International journal of pharmaceutics*, 342(1-2):115–123, 2007.

[6] D. Barrasso, S. Oka, A. Muliadi, J. D. Litster, C. Wassgren, and R. Ramachandran. Population balance model validation and predictionof cqas for continuous milling processes: Toward qbdin pharmaceutical drug product manufacturing. *Journal of Pharmaceutical Innovation*, 8(3):147–162, 2013.

[7] E. Bilgili and B. Scarlett. Population balance modeling of non-linear effects in milling processes. *Powder Technology*, 153(1):59–71, 2005.

[8] J. M. Bultmann. Multiple compaction of microcrystalline cellulose in a roller compactor. *European journal of pharmaceutics and biopharmaceutics*, 54(1):59–64, 2002.

[9] R. Charls. Energy-size reduction relationships in comminution. *Trans. AIME*, 9:80–88, 1957.

[10] T. Feng, F. Wang, R. Pinal, C. Wassgren, and M. T. Carvajal. Investigation of the variability of nir in-line monitoring of roller compaction process by using fast fourier transform (fft) analysis. *Aaps Pharmscitech*, 9(2):419–424, 2008.

[11] J. F. Gamble, M. Tobyn, A. B. Dennis, and T. Shah. Roller compaction: application of an in-gap ribbon porosity calculation for the optimization of downstream granule flow and compactability characteristics. *Pharmaceutical development and technology*, 15(3):223–229, 2010.

[12] M. K. Ghorab, R. Chatlapalli, S. Hasan, and A. Nagi. Application of thermal effusivity as a process analytical technology tool for monitoring and control of the roller compaction process. *AAPS PharmSciTech*, 8(1):E155–E161, 2007.

[13] C. Gotsis, L. Austin, P. Luckie, and K. Shoji. Modeling of a grinding circuit with a swing-hammer mill and a twin-cone classifier. *Powder technology*, 42(2):209–216, 1985.

[14] P. Guigon and O. Simon. Roll press design—influence of force feed systems on compaction. *Powder Technology*, 130(1-3):41–48, 2003.

[15] M. G. Herting and P. Kleinebudde. Roll compaction/dry granulation: Effect of raw material particle size on granule and tablet properties. *International journal of pharmaceutics*, 338(1-2):110–118, 2007.

[16] H. Hughes, M. M. Leane, M. Tobyn, J. F. Gamble, S. Munoz, and P. Musembi. Development of a material sparing bulk density test comparable to a standard usp method for use in early development of api's. *AAPS PharmSciTech*, 16(1):165–170, 2015.

[17] S. Inghelbrecht and J. P. Remon. Roller compaction and tableting of microcrystalline cellulose/drug mixtures. *International Journal of Pharmaceutics*, 161(2):215–224, 1998.

[18] K. S. Khomane and A. K. Bansal. Yield strength of microcrystalline cellulose: Experimental evidence by dielectric spectroscopy. *International journal of pharmaceutics*, 455(1-2):1–4, 2013.

[19] H. Lim, V. S. Dave, L. Kidder, E. N. Lewis, R. Fahmy, and S. W. Hoag. Assessment of the critical factors affecting the porosity of roller compacted ribbons and the feasibility of using nir chemical imaging to evaluate the porosity distribution. *International journal of pharmaceutics*, 410(1-2):1–8, 2011.

[20] A. Miguelez-Moran, C.-Y. Wu, and J. Seville. The effect of lubrication on density distributions of roller compacted ribbons. *International journal of pharmaceutics*, 362(1-2):52–59, 2008.

[21] A. M. Miguélez-Morán, C.-Y. Wu, H. Dong, and J. P. Seville. Characterisation of density distributions in roller-compacted ribbons using micro-indentation and x-ray micro-computed tomography. *European Journal of Pharmaceutics and Biopharmaceutics*, 72(1):173–182, 2009.

[22] R. W. Miller. Roller compaction technology. *Drugs and the pharmaceutical sciences*, 81:99–150, 1997.

[23] J. J. Motzi and N. R. Anderson. The quantitative evaluation of a granulation milling process i. algebraic method for particle size analysis. *Drug Development and Industrial Pharmacy*, 10(2):225–239, 1984.

[24] S. Patel, A. M. Kaushal, and A. K. Bansal. Effect of particle size and compression force on compaction behavior and derived mathematical parameters of compressibility. *Pharmaceutical research*, 24(1):111–124, 2007.

[25] S. Patel, A. M. Kaushal, and A. K. Bansal. Mechanistic investigation on pressure dependency of heckel parameter. *International journal of pharmaceutics*, 389(1-2):66–73, 2010.

[26] S. Peter, R. F. Lammens, and K.-J. Steffens. Roller compaction/dry granulation: Use of the thin layer model for predicting densities and forces during roller compaction. *Powder technology*, 199(2):165–175, 2010.

[27] G. Reynolds, J. Fu, Y. Cheong, M. Hounslow, and A. Salman. Breakage in granulation: a review. *Chemical Engineering Science*, 60(14):3969–3992, 2005.

[28] G. K. Reynolds. Modelling of pharmaceutical granule size reduction in a conical screen mill. *Chemical Engineering Journal*, 164(2-3):383–392, 2010.

[29] L. Salbu. Compressibiliy and compactibility of pectin powders-a study of their potential as direct compression excipients in tablets. 2011.

[30] L. R. Schenck and R. V. Plank. Impact milling of pharmaceutical agglomerates in the wet and dry states. *International journal of pharmaceutics*, 348(1-2):18–26, 2008.

[31] S. Schiano, C.-Y. Wu, A. Mirtic, and G. Reynolds. A novel use of friability testing for characterising ribbon milling behaviour. *European Journal of Pharmaceutics and Biopharmaceutics*, 104:82–88, 2016.

[32] J. P. Seville and C.-Y. Wu. *Particle Technology and Engineering: An Engineer's Guide to Particles and Powders: Fundamentals and Computational Approaches*. Butterworth-Heinemann, 2016.

[33] P. J. Sheskey, T. D. Cabelka, R. T. Robb, and B. M. Boyce. Use of roller compaction in the preparation of controlled-release hydrophilic matrix tablets containing methylcellulose and hydroxypropyl methycellul ose polymers. *Pharmaceutical technology*, 18(9):132–132, 1994.

[34] C. Sun and D. J. Grant. Influence of crystal structure on the tableting properties of sulfamerazine polymorphs. *Pharmaceutical research*, 18(3):274–280, 2001.

[35] W.-J. Sun and C. C. Sun. Ribbon thickness influences fine generation during dry granulation. *International journal of pharmaceutics*, 529(1-2):87–88, 2017.

[36] S. G. von Eggelkraut-Gottanka, S. A. Abed, W. Müller, and P. C. Schmidt. Roller compaction and tabletting of st. john's wort plant dry extract using a gap width and force controlled roller compactor. i. granulation and tabletting of eight different extract batches. *Pharmaceutical development and technology*, 7(4):433–445, 2002.

[37] R. Wiedey and P. Kleinebudde. The density distribution in ribbons from roll compaction. *Chemie Ingenieur Technik*, 89(8):1017–1024, 2017.

[38] C.-Y. Wu and A. Cocks. Flow behaviour of powders during die filling. *Powder Metallurgy*, 47(2):127–136, 2004.

[39] P. York. Particle slippage and rearrangement during compression of pharmaceutical powders. *Journal of Pharmacy and Pharmacology*, 30(1):6–10, 1978.

[40] P. Yu, W. Xie, L. Liu, and M. Powell. The development of the wide-range 4d appearance function for breakage characterisation in grinding mills. *Minerals Engineering*, 110:1–11, 2017.

[41] W. Yu and B. C. Hancock. Evaluation of dynamic image analysis for characterizing pharmaceutical excipient particles. *International journal of pharmaceutics*, 361(1-2):150–157, 2008.

[42] Y. Zhang, Y. Law, and S. Chakrabarti. Physical properties and compact analysis of commonly used direct compression binders. *aaps Pharmscitech*, 4(4):489–499, 2003.

Appendix A

In this first Appendix, the MATLAB® code used to perform the optimization is reported. In this way it was possible to identify the sets of parameters for the five different ribbon batches. In particular this code referrs to batch (c).

```
%=========================================================================
%                          PBM screen size 2 [mm]
%                             Porosity 35.5 %
%=========================================================================

function PBM_fitting

clc
close all
clear all
format long

%% Parameter guess

m1 = 2.2;
m2 = 2.5;
p1 = 180;
p2 = 952;
a1 = 0.523;
k1 = 0.154;
k2 = 1.13;
sigma = 0.1;

M = 180; %[g] INLET mass

%% UN-constrained OPTIMIZATION
% par0 = [m1 m2 p1 p2 a1 k1 k2 sigma];
%
% options = optimset('MaxFunEvals',15000);
% % options = optimset('TolFun',1e-12);
% obj = fminsearch(@S,par0,options);
%
% function S = S(par0)

%% Constrained OPTIMIZATION

par0 = [m1;m2;p1;p2;a1;k1;k2;sigma];
```

```
A = [];
b = [];
Aeq = [];
beq = [];

lb = [0;0;0;0;0;0;0;0];
ub = [10;10;1000;3000;1;0.5;5;0.3];

options = optimset('TolCon', 1e-100, 'TolX', 1e-100);

obj = fmincon(@S,par0,A,b,Aeq,beq,lb,ub,[],options);

function S = S(par0,A,b,Aeq,beq,lb,ub)

Xi= [7605;5377;3802;2688;1901.29;1474.59;1143.65;886.98;687.92;...
     533.53;413.79;320.93;248.9;193.04;149.72;116.12;90.06;69.85;...
     54.17;42.01;32.58;25.27;19.6;15.2;11.79;9.14;7.09;6.23;4.39];

y0 = [9.0598,0,0,0,0,0,0,0,0,0,0,0,0,0,0,0,0,0,0,0,0,0,0,0,0,0,0,0];

% Experimental results
yexp = [0;0;0.0005;0.001;0.00275;0.00625;0.01275;0.0250;0.05075;...
        0.10875;0.1945;0.30275;0.4610;0.67175;0.9163;0.94125;...
        0.75075;0.5305;0.436;0.56075;0.8575;1.01775;0.7795;...
        0.431750;0]';

% Bij calculation

Yi= par0(5)*((1-exp((log(0.2))*(Xi/par0(3)).^par0(1))))+...
    (1-par0(5))*((1-exp((log(0.2))*(Xi/par0(4)).^par0(2))));
Yi2=[Yi(2:29);0];
Zi=Yi-Yi2;

for ii=2:28
    Zi(:,ii)= Zi(:,ii-1);
end
Bob = tril((Zi));

for r=1:28
    Bob(r,r)=0;
end

YiJim = Yi(2:29);
YiT = YiJim.';
for iii = 2:29
```

```
    YiT(iii,:) = YiT(iii-1,:);
end

Bij=Bob./YiT;

%S calculation

Xtop = max(Xi);
S=par0(6)*((Xi./Xtop).^par0(7));

c = zeros(29,1);
dscreen = 2000; %[\mum]
limit = (1-par0(8))*dscreen;

for h = 1:29
    if Xi(h) <= limit
        c(h,1)=0;
    elseif Xi(h) > dscreen
        c(h,1)=1;
    else
        c(h,1)=(dscreen-Xi(h))/(par0(8)*dscreen);
    end
end

tspan = [0,60]; %[s]
[t,y] = ode45(@PBM,tspan,y0,[],S,Bij,c); %SOLVER

Y = fliplr(y);

Dy = Y(end,1:25);

S = norm(yexp-Dy); %LS method

%% Plot section

% Visualization (LINE PLOT)

XP = flipud(Xi); % MAX class size
semilogx(XP(1:25),yexp,'or')
hold on
semilogx(XP(1:25),Y(end,1:25))
xlabel('x [\mum]');
ylabel('M_i/\Deltax_i [kg/\mum]');
xticks([0 42 90 212 414 800 1400 2000 3338 4720 6675 7605])
xticklabels({'0','42',' ','212',' ',' ',' ','2000',' ',' ',' ','7605'})
```

```
title(sprintf('m_1=%7.3g   m_2=%7.3g   p_1=%7.3g   p_2=%7.3g',par0))
title(sprintf('a=%7.3g   k_1=%7.3g   k_2=%7.3g   sigma=%7.3g',par0))
ylim([0 1.2])
xlim([0 max(Xi)])
grid on
hold off
drawnow

function dM = PBM(t,y,S,Bij,c)

dM(1) = -S(1)*y(1)*c(1);

for i = 2:29
    Sum = 0;
    for j = 1:i-1
        Sum = Sum + Bij(i,j)*S(j)*y(j)*c(j);
    end
    dM(i) = Sum - (S(i)*y(i)*c(i));
end
dM = dM';
```

Appendix B

The parameter identification has been performed for all the ribbon batches. This MATLAB® code was implemented to identify the most suitable combination of the parameters m_1 and m_2 capable to match the experimental results. Please notice that the 2D matrix `yexp` and the 3D matrix `Y` are incompleted due to lack of space. The outputs of the script are two 3D plots oriented in the XY plane view. In the first `subplot` the matrix combinations are illustrated, whereas in the `Figure(2)` the experimental data are depicted.

```
%=========================================================================
%                          Combinatorial analysis
%=========================================================================

%% Experimental data

Xi= [7605;5377;3802;2688;1901.29;1474.59;1143.65;886.98;687.92;...
     533.53;413.79;320.93;248.9;193.04;149.72;116.12;90.06;69.85;...
     54.17;42.01;32.58;25.27;19.6;15.2;11.79;9.14;7.09;6.23;4.39];

% 5x29 Matrix (first row --> 15 kN, second row --> 22.5 kN,...)

y0 = zeros(5,29);
y0(:,1)=[9.0590;9.0607;9.0598;9.0590;9.0600];

% 5x25 Matrix (first row --> 15 kN, second row --> 22.5 kN,...)

yexp = zeros(5,29);
yexp(:,1:25) = [0 0 0 0.0010000000000 0.002000000000 0.0040000...
                0 0 0 0.0010000000000 0.002000000000 0.0040000...
                0 0 0.000500000000000 0.001000000000 0.0027500...
                0 0 0 0.0010000000000 0.001000000000 0.0030000...
                0 0 0 0 0.00100000000 0.002000000000 0.0036666..];

XP = flipud(Xi);

% 5x29x7 Matrix (first row --> 15 kN, second row --> 22.5 kN,...)
Y = zeros(5,29,7);

% 1 --> m1 = 2 m2 = 2
% 2 --> m1 = 2 m2 = 2.5
% 3 --> m1 = 2 m2 = 3
% 4 --> m1 = 2.5 m2 = 2
```

```
% 5 --> m1 = 2.5 m2 = 2.5
% 6 --> m1 = 2.5 m2 =3
% 7 --> m1 = 3 m2 = 2
% 8 --> m1 = 3 m2 = 2.5
% 9 --> m1 = 3 m2 = 3

Y(:,:,2) = [0.00519933955697375 0.00526948030557629 0.0030876691...
            0.00402960445037246 0.00408565879103802 0.0023944256...
            0.00335609783980195 0.00340403999031504 0.0019952707...
            0.00207400429448475 0.00210650476138620 0.0012354361...
            0.00114566124110004 0.00116698194775742 0.0006852534..];
Y(:,:,1) = [0.00512592407425138 0.00519375377643777 0.0030429780...
            0.00393699604278397 0.00398914244473467 0.0023372292...
            0.00321076561812290 0.00325333217702872 0.0019061380...
            0.00193104501520826 0.00195673055578811 0.0011464946...
            0.00094718943319667 0.00096144648677165 3 0.00056338..];
Y(:,:,4) = [0.00076553789303866 4 0.00104259246260934 0.000677108...
            0.00064899229128594 4 0.00085826042972449 6 0.00055267...
            0.00055794579017666 6 0.00071954113488554 1 0.00045987...
            0.00045550854197849 1 0.00055232457364440 1 0.00034616...
            0.00036117034094457 9 0.00040312340477562 8 0.00024545..];
Y(:,:,5) = [0.00071314520402797 7 0.00099768168514876 5 0.00065281...
            0.00055693190393526 9 0.00077914187125828 3 0.00050981...
            0.00044100839276894 4 0.00061696663727996 2 0.00040370...
            0.00029647069477000 1 0.00041476093995325 6 0.00027139...
            0.00017208423378977 5 0.00024074632851909 2 0.00015752..];
Y(:,:,6) = [0.00071746636261370 8 0.00100384139244770 0.000656878...
            0.00056362444713725 2 0.00078872002437333 6 0.00051614...
            0.00045012090428240 3 0.00062997233223295 6 0.00041228...
            0.00031829097326251 1 0.00044567150703005 4 0.00029173...
            0.00019602616388935 7 0.00027469751035857 5 0.00017988..];
Y(:,:,8) = [9.70585508960337e-05 0.00017833704479830 3 0.00012954...
            7.91833293564197e-05 0.00014353359591622 9 0.00010381...
            6.50096471094124e-05 0.00011646189736067 1 8.39132824...
            5.16582853064968e-05 8.96967626456582e-05 6.39571545...
            3.76322062896741e-05 6.24303975836086e-05 4.38067095..];
Y(:,:,9) = [9.40565798399514e-05 0.00017475863465173 0 0.00012739...
            7.37205332690810e-05 0.00013697394444754 3 9.98497217...
            5.84658924923480e-05 0.00010863058223713 9 7.91883031...
            4.18664295777849e-05 7.77885261811797e-05 5.67054209...
            2.62832387569109e-05 4.88347153500503e-05 3.55990065..];

eps = [46.72 39.45 34.35 27.30 23.82];
eps = fliplr(eps);
```

```
%% First plot (lines+map 3D)

xx = linspace(0.0025,max(Xi),10001);
EPS = repmat(eps',1,10001);

for W = 1:9
    if W == 3 || W == 7
        W = W+1;
    end
    subplot(3,3,W)

        for w = 1:5

            plot3(XP(1:25),eps(w)*ones(25),yexp(w,1:25),'or',...
                 'Markersize',3)
            hold on
            set(gca,'xscale','log')
            xlim([min(Xi) max(Xi)])
            zlim([0 max(max(yexp))+0.1])
            ylim([min(eps) max(eps)])
            cs = pchip(XP,Y(w,:,W));
            plot3(xx,EPS(w,:),ppval(cs,xx),'-k','Linewidth',1);
            hold on
            xticks([0 42 90 212 414 800 1400 2000 3338 4720 6675 7605])
            xticklabels({'0','42',' ','212',' ',' ',' ','2000',' ',...
                         ' ',' ','7605'})
            yticks(eps)
            yticklabels({'(a)','(b)','(c)','(d)','(e)'})
            ylabel('Porosity [%]','Fontsize',14)
            xlabel('x [\mum]','Fontsize',14);
            zlabel('M_i/\Deltax_i [kg/\mum]','Fontsize',14);
            hold on
        end
        for O = 1:5
            Dy = Y(:,:,W);
            D(:,O,:) = Dy;
            cs = pchip(XP,[Dy(O,:)]);
            A(O,:) = ppval(cs,xx);
            if O == 5
            H = linspace(0,max(max(yexp)),10001);
            HH = repmat(H,5,1);
            s = surf(xx,eps,A,'Facecolor','interp');
            s.EdgeColor = 'none';
            caxis([0 2.05])
            end
```

```
        end
        set(gca,'Fontsize',14)
end

hlink = linkprop([subplot(3,3,1),subplot(3,3,2),subplot(3,3,3),...
                  subplot(3,3,4),subplot(3,3,5),subplot(3,3,6),...
                  subplot(3,3,7),subplot(3,3,8),subplot(3,3,9)],...
                  {'CameraPosition','CameraUpVector'});
rotate3d on

view(0,90) %view on XY plane

%% Second plot (experimental data)

figure(2)

xx1 = linspace(0.0025,max(XP),10001);
for L = 1:5
    DY = yexp;
    DD(:,L,:) = DY;
    Cs = pchip(XP,[DY(L,:)]);
    V(L,:) = ppval(Cs,xx1);
end
r = surf(xx1,eps,V,'Facecolor','interp');
r.EdgeColor = 'none';
view(0,90) %view on XY plane
xticks([0 42 90 212 414 800 1400 2000 7605])
xticklabels({'0','42',' ','212',' ',' ',' ','2000','7605'})
yticks(eps)
set(gca,'xscale','log')
yticklabels({'(a)','(b)','(c)','(d)','(e)'})
ylabel('Porosity [%]')
xlabel('x [\mum]');
zlabel('M_i/\Deltax_i [kg/\mum]');
xlim([min(Xi) max(Xi)])
zlim([0 max(max(yexp))+0.1])
ylim([min(eps) max(eps)])
set(gca,'Fontsize',16)
% colorbar('southoutside')
```

Appendix C

After the parameters identification, this final script allows to calculate the granule size distribution inserting as inputs the mass of material entering the mill and the average porosity of the feeding ribbon batch. An additional input is the array of GSD experimental data that can be entered in order to have a direct comparison between experimental and modelled results in the final graphical output.

```
%=========================================================================
%                              PBM Final script
%=========================================================================

clc
clear all
close all

%% Variables definition

M = input('Insert initial mass'); %[g] INLET mass

% Model parameters

m1 = 2;
m2 = 2.5;
p1 = 212;
p2 = 988;
k1 = 0.939;
k2 = 1;
sigma = 0.0494;

eps = input('Insert ribbon porosity'); %[%]
a = 1/(1+exp(-0.1228*(eps-34.45)));

qP = [0.001;0;0.005;0.012;0.024;0.054;0.108;0.232;0.452;0.811;...
      1.235;1.533;1.497;1.246;1.012;0.586;0.2;0.037;0.012;0];
y0 = [9.0590,0,0,0,0,0,0,0,0,0,0,0,0,0,0,0,0,0,0,0,0,0,0,0,0,0,0,0,0,0,0];
y0exp = input('Insert array experimental data for validation');

F = [15 22.5 30 45 60 68.36]; %[kN]
Pr = F./(pi/4*32^2)*1000; %[MPa]

% Particle size array
```

```
Xi= [7605;5377;3802;2688;1901.29;1474.59;1143.65;886.98;687.92;...
     533.53;413.79;320.93;248.9;193.04;149.72;116.12;90.06;69.85;...
     54.17;42.01;32.58;25.27;19.6;15.2;11.79;9.14;7.09;6.23;4.39];

% Bij calculation

Yi= a*((1-exp((log(0.2))*(Xi/p1).^m1)))+...
    (1-a)*((1-exp((log(0.2))*(Xi/p2).^m2)));
Yi2=[Yi(2:29);0];
Zi=Yi-Yi2;

for ii=2:28
    Zi(:,ii)= Zi(:,ii-1);
end
Bob = tril((Zi));

for r=1:28
    Bob(r,r)=0;
end

YiJim = Yi(2:29);
YiT = YiJim.';
for iii = 2:29
    YiT(iii,:) = YiT(iii-1,:);
end

Bij=Bob./YiT;

%S calculation

Xtop=max(Xi);
S=k1*((Xi./Xtop).^k2);

%c calculation (classification function)

c = zeros(29,1);
dscreen = 2000; %[\mum]
limit = (1-sigma)*dscreen;

for h = 1:29
    if Xi(h) <= limit
        c(h,1)=0;
    elseif Xi(h) > dscreen
        c(h,1)=1;
    else
```

```
        c(h,1)=(dscreen-Xi(h))/(sigma*dscreen);
    end
end

tspan = [0,60];

[t,y] = ode45(@PBM,tspan,y0,[],S,Bij,c);

Y = fliplr(y);

%% Simulation

figure(1)

XP = flipud(Xi); % MAX class size
hold on
for w = 1:length(t)
    Dy = Y(w,:);
    semilogx(2000*ones(100),linspace(0,2.5,100),'--k','Linewidth',1);
    hold on
    plot(XP(1:25),y0exp,'or','Markersize',7)
    hold on
    xticks([0 42 90 212 414 800 1400 2000 3338 4720 6675 7605])
    xticklabels({'0','42',' ','212',' ',' ',' ','2000',' ',' ',...
                 ' ','7605'})
    title('PSD 2 mm screen');
    ylabel('M_i/\Deltax_i [kg/\mum]');
    cs = pchip(XP,[Dy]);
    xx = linspace(0.0025,7605,10001);
    plot(xx,ppval(cs,xx),'-k','Linewidth',2)
    xlim([min(Xi) 2500])
    set(gca,'Xscale','log')
    xlabel('x [\mum]','Fontsize',14);
    ylabel('M_i/\Deltax_i [kg/\mum]','Fontsize',14);
    yticks([0 .5 1 1.5 2])
    yticklabels({'0','0.5','1','1.5','2'})
    ylim([0 2])
    hold off
    drawnow
end

hold on
CS = pchip(XP(1:20),[qP]);
XX = linspace(0.0025,550,10001);
plot(XX,ppval(CS,XX),'-','Color',[0 0 0]+0.8)
```

```
function dM = PBM(t,y,S,Bij,c)

dM(1) = -S(1)*c(1)*y(1);

for i = 2:29
    Sum = 0;
    for j = 1:i-1
        Sum = Sum + Bij(i,j)*S(j)*y(j)*c(j);
    end
    dM(i) = Sum -S(i)*c(i)*y(i);
end
dM = dM';
end
```